BERLINER
GEOWISSENSCHAFTLICHE
ABHANDLUNGEN

Reihe D Band 14

Nasir Hasen Kenea

Digital Enhancement of Landsat Data, Spectral Analysis and GIS Data Integration for Geological Studies of the Derudeb Area, Southern Red Sea Hills, NE Sudan

FU • TU • TFH

Berlin

1997

BERLINER GEOWISSENSCHAFTLICHE ABHANDLUNGEN

Reihe A: Geologie und Paläontologie Reihe B: Geophysik • Reihe C: Kartographie
Reihe D: Geoinformatik • Reihe E: Paläobiologie

Reihe D: Geoinformatik

D188

Herausgegeben von geowissenschaftlichen Instituten
der Freien und der Technischen Universität Berlin
sowie von der Technischen Fachhochschule Berlin

Selbstverlag Fachbereich Geowissenschaften
Freie Universität Berlin
1997

Berliner geowiss. Abh., D, 14, 116 pp., Berlin 1997

NASIR HASEN KENEA

Digital Enhancement of Landsat Data, Spectral Analysis and GIS Data Integration for Geological Studies of the Derudeb Area, Southern Red Sea Hills, NE Sudan

Selbstverlag Fachbereich Geowissenschaften, FU Berlin

Der Druck dieser Arbeit wurde finanziert aus Mitteln des Deutschen Akademischen Austauschdienstes (DAAD).

Druck: Offsetdruckerei G. Weinert, Saalburstraße 3, 12099 Berlin
Verlag: Selbstverlag Fachbereich Geowissenschaften, Freie Universität Berlin. 1997.

ISBN 3-89582-039-3
ISSN 0941-23 IX

CONTENTS

Zusammenfassung

Die Geologie des Arbeitsgebietes Derudeb ist mit Methoden der Fernerkundung und Ge-Informationssystemen auf der Grundlage einer begrenzten Datenbasis untersucht worden. Als Ergebnis wurde ein geologisches Kartenblatt im Maßstab 1 : 250 000 erstellt. Das Gebiet der südlichen Red Sea Hills, im NE des Sudan gelegen, bildet den nubischen Teil des Arabisch-Nubischen Schildes. Verschiedene Gneise, metavulkano-sedimentäre Serien und intrudierte syn- und postorogene Plutonite saurer bis basischer Zusammensetzung bilden das Grundgebirge proterozoischen Alters. Die phanerozoischen Gesteine des Untersuchungsgebietes bestehen überwiegend aus Sandsteinen sowie aus basaltischen und rhyolitischen Extrusiva, die wiederum von Gangschwärmen durchschnitten sind.

Die duktilen Hauptdeformationsereignisse, wie Sie in den Gesteinen des Grundgebirges erkannt wurden, sind Ergebnisse der Akkretionstektonik des Nubischen Schieides, die eine wiederholte Faltung und Krustenverkürzung während der Pan-Afrikanischen Phase bewirkten. Die Adadi-Überschiebungs- und Transpressions-Scherzone ist eines der Haupt-strukturelemente, die der Akkretionstektonik zugeordnet werden können. Sie ist typisiert durch intensiv zerscherte und zerlegte Meta-Ultramafite und ausgedehnte Scherbänder. Diese Zone ist sinistral versetzt, ebenso wie die neoproterozoische Nakasib Suture im N und wird als mögliche Krustengrenze angesehen, die in künftigen Akkretionsmodellen dieses Gebietes berücksichtigt werden sollte. Das in der Arbeit neudefinierte "Baraka Terrane" stellt wahrscheinlich eines der ältesten Krustensegmente der Region dar.

Dehnungstektonik wahrscheinlich mesozoischen Alters ließ das Odi-Riftbecken entstehen. Spätoligozäner bis frühmiozäner Vulkanismus entlang von Dehnungsbrüchen entwickelte sich im Odi-Becken und Adar-Ribad-Gebiet, wobei im Odi-Becken der Vulkanismus teilweise unter Wasserbedeckung stattgefunden hat. Die begrenzenden Störungen sind häufig reaktivierte Lineamente des Pan-Afrikan mit submeridionaler Orientierung. NE-SW streichende Transform-störungen mit linkslateralen Bewegungen sind älter als die N-S verlaufenden. Die Dehnung, in deren Anschluß Magmatismus und Hebung folgten, ist in Richtung des Roten Meers deutlich stärker.

Für visuelle Verbesserungen der Landsat-Daten wurden IHS Transformationen der drei am wenigsten korrelierten Kanäle verwandt, um eine gute lithologische Unterscheidbarkeit zu gewährleisten. Eine Hauptkomponentenanalyse erbrachte bessere Resultate für das S/N-Verhältnis, wenn standardisierte Koeffizienten anstelle der Kovarianzmatix eingesetzt wurden. Weiterhin hat sich die Auswahl von vier Spektralkanälen, anstelle aller sechs Kanäle, für die Hauptkomponentanalyse als ausreichend erwiesen, um eine gute lithologische Trennung im Bild zu erreichen. Weitere Verbesserungen der Ergebnisse ergaben sich durch die Verrechnung der ersten mit den weiteren Hauptkomponenten. Die Histogramm-Streckung durch Dekorrelation stellt ebenfalls ein wertvolles Hilfsmittel für die Bereitstellung von Band-kombinationen dar, das durch die Vernachlässigung der verrauschten Haupt-komponenten ebenfalls eine Qualitätssteigerung der rücktransformierten Daten bewirkt. Ratiobildungen verschiedener Band-kombinationen lieferten brauchbare Bilder unter Anwendung der "directed-band-ratio"-Technik, die sowohl spektrale als auch morphologische Informationen enthalten. Allgemein gesprochen, ermöglicht die Kombination verschiedener Bildverbesserungsmethoden die Erstellung einer optimierten Bildinterpretation. Die digitale Klassifizierung von spektralen und Textur-elementen erwies sich in diesem Zusammenhang als nicht sehr hilfreich.

Gossans als Indikator für Gold-Sulphid-Vorkommen wurden erfolgreich sowohl mit der "feature-oriented-PCA" (Hauptkomponenten-analyse) als auch mit Ratiobildern kartiert. Diese Ergebnisse konnten durch den Einsatz von GIS-Techniken weiter verbessert werden. Die Methode der IHS-Transformation hat zur Identifikation eines bisher unbekanten Gossans bei Derudeb geführt. Die Analyse von im Labor durchgeführte

Spektralmessungen an ausgewählten Proben ergab eine durch Wüstenlack hervorgerufene Reduzierung der Reflektanz um bis zu 70% im VIS und um 20% im SWIR des elektromagnetischen Spektrums. Im sichtbaren Bereich des Spektrums werden durch den Einfluß des Wüstenlacks die Absorptionsbanden von Gesteinen überdeckt, so daß ein "flaches" Signal resultiert. Im SWIR kommt es nur zu einer Abschwächung, wobei die generelle Form erhalten bleibt. Diese Effekte haben anscheinend nur geringen Einfluß auf die Unterscheidbarkeit der Gossans von anderen Gesteinen.

Bouguer und residuale Schweredaten, Aeromagnetik, geologische und topographische Daten wurden mittels GIS aufbereitet. In den meisten Fällen erbrachte eine Oberflächenmodellierung besser interpretierbare Ergebnisse. Im allgemeinen zeigen die Schweredaten eine gute Übereinstimmung mit der Verteilung der Plutone, wohingegen die aeromagnetischen Daten besser für die Lokalisierung von regional bedeutsamen Lineamenten geeignet sind. Beide Datentypen unterstützen die Trennbarkeit der in dieser Arbeit vorgeschlagenen Krustenblöcke (Terranes) im Arbeitsgebiet.

Vom Fachbereich Geowissenschaften der Freien Universität Berlin zur Erlangung des akademischen Grades Dr. rer. nat. genehmigte Dissertation.
Tag der Disputation: 03.02.1997; Gutachter: Prof. Dr. F. K. List, Prof. Dr. E. Klitzsch.

This work has been accepted as doctoral thesis at the Free University of Berlin, Department of Geosciences.

Anschrift der Verfassers: Freie Universität Berlin, Institut für Geologie, Geophysik und Geoinformatik, Fachrichtung Geoinformatik, Malteser-Str. 74-100, 12249 Berlin.

Abstract

The geology of the Derudeb area has been studied by means of remote sensing and Geo-Information System (GIS) techniques, and limited field data, with the production of a geological map at a scale of 1 : 250 000. The area of the southern Red Sea Hills, NE Sudan, forms part of the Nubian sector of the Arabian-Nubian Shield. Various gneisses and metavolcano-sedimentary schists intruded by syn- and post-orogenic plutons of basic to acidic composition constitute the basement lithology of generally Neoproterozoic age. Sedimentary rocks dominated by sandstone, and basaltic as well as rhyolitic flows dissected by dike swarms comprise the Phanerozoic sequence in the area.

The major ductile deformation events recognised in the basement rocks correspond to the accretion tectonics of the Nubian Shield that gave rise to repeated foldings and crustal shortenings during the Pan-African. The high-strain Adadi Thrust and Transpressional Shear Zone is one of the principal structures ascribed to these events. It is typified by strongly sheared and dismembered meta-ultramafics and extensive shear bands. This zone is sinistrally displaced like the Neoproterozoic Nakasib Suture to the N, and is thought to denote a possible crustal boundary to be considered in future accretion models for this area. The redefined Baraka Terrane probably represents one of the oldest crustal segments in the region.

Extensional tectonics of presumably Mesozoic time produced the Odi rift basin. Late Oligocene-Early Miocene volcanism along extensional fractures occurred in the Odi basin and Adar Ribad areas, in the former case partly in a subaqueous environment. The bounding normal faults are often reactivated major Pan-African lineaments with a submeridional trend. Younger NE-SW striking transcurrent faults with left-lateral movements apparently represent the latest extensional episode in the area. Extension, that was subsequently followed by magmatism and uplifting, was seemingly greater towards the Red Sea.

For visual enhancement of Landsat data IHS transformation of the three least correlated bands yielded an overall good lithologic enhancement. PC (Principal Component) analysis resulted in a higher signal-to-noise ratio when standardized coefficients were used instead of the covariance matrices. Four bands, instead of six, proved sufficient to produce substantial spectral contrast; modifications by convolving the first PC with the other components yielded improved results. Decorrelation stretching is also a valuable tool in providing a higher number of band triplets, and omission of noise-dominated PCs during retransformation generally gave substantial enhancements. Band ratioing yielded geologically useful images by adopting the "directed band ratio" technique, whereby both spectral and morphological information are preserved. Generally, combinations of results from different enhancement methods are suitable for comprehensive results during image interpretation. Digital classification of spectral and textural parameters proved less useful in the present context.

Gossans as markers of gold-sulphide deposits have been successfully mapped by using "feature oriented PCA" and band ratioing, with improved results obtained by a GIS-overlay technique. IHS decorrelation stretching has led to the discovery of a gossan body in the Derudeb area. Spectral analysis of selected rock samples has shown that overall reflectance is reduced by up to 70% in the VIS parts and 20% in the SWIR parts of the electromagnetic spectrum due to desert varnish. In the VIS region absorption bands turn to featureless spectra due to this effect, whereas in the SWIR spectra are generally subdued but preserved. This has apparently little consequence on the discrimination of gossans from other rock types.

Bouguer gravity, residual gravity, aeromagnetic, geologic and topographic data were processed using GIS techniques. In most cases surface modelling yielded more interpretable results. Generally, the gravity data show good conformity with plutonic distribution whereas aeromagnetic data are more helpful for detection of lineaments of regional significance. Both the gravity and aeromagnetic data apparently corroborate the geologic interpretation in depicting the suggested different crustal blocks.

Acknowledgements

This work has been conducted within the framework of the Special Research Project-69 "Geological Problems in Arid and Semi-arid Areas", funded by the German Research Foundation (Deutsche Forschungsgemeinschaft). The study has been carried out under a scholarship financed by the German Academic Exchange Services (Deutscher Akademischer Austausch-dienst). Both are gratefully acknowledged.

I would like to express my sincere thanks and gratitude to Prof. Dr. F. K. List for his initiation, guidance and invaluable discussions at all stages of the work. His unreserved help in making my study a success is greatly appreciated. Advices provided by Prof. Dr. E. Klitzsch are also sincerely acknowledged.

Special thanks are due to Dr. C. J. Ebinger (University of Leeds, UK) for her unreserved help in reviewing part of the thesis and suggesting valuable ideas. Absolute age determination of selected rock sample were also made possible through her assistance, and the cooperation of Dr. D. C. Rex.

Dr. G. Matheis and Mrs. A. Brown (Technical University of Berlin) conducted the chemical analysis of some rock samples. Dr. E. M. Abdel Rahman (Geological Research Authority of the Sudan), and Prof. R. J. Vail (Portsmouth Polytechnic, UK) cooperated in getting some materials pertaining to the study area. I am grateful to all.

I am thankful to Dr. H. Kaufmann and G. Krüger (Geoforschungszentrum, Potsdam) who have been helpful in using the Lambda 19 spectrometer. Dr. H. Burger shared discussions on some statistical aspects of the work.

Several colleagues have been helpful at different stages of the work. H. Haenisch, N. Ott, I. A. I. Shaddad and Dr. H. Worku shared discussions pertaining to the geology of the area. R. Schoele has been cooperative to solve problems with the computers. Dr. K. Hofmann and Dr. W. Koch were helpful at various stages of the work. Dr. H. Kußerow, Dr. C. Bauer, I. Bido, I. Gräbe and C. Gummersbach have been cooperative in different aspects during my study. A. Schwenger drew some of the diagrams and P. Böttcher scanned samples on the electron microscope. I am very grateful to all.

I am indebted to Prof. R. P. Gupta and Mr. Amenti Abraham for their support to my application for the DAAD scholarship.

Special regard is due to my wife Fatuma for her unreserved inspiration, sacrifice and understanding. Her endurance with Hawie, in my absence, is greatly appreciated. My mother Merema and my sisters deserve sincere acknowledgements for their consistent encouragement and concerns. Finally, a long list of close friends and relatives who contributed to this achievement in one way or another are deep-hearted ly thanked.

1 Introduction

1.1 The Study Area

The area covered by Sheet Derudeb 1 : 250 000 (NE 37-1) is situated in the Red Sea Province of northeastern Sudan, bounded by longitudes 36°00' and 37°30' E, and parallels 17°00' and 18°00' N (Figure 1.1) out of which an area of about 16,800 km^2 has been investigated by this work. The main asphalted Khartoum-Port Sudan road *(ca.* 1170 km) traverses N-S through the western part of the map sheet crossing the Derudeb township. Port Sudan, to the NE, can also be reached from Khartoum by air on daily schedule. Other seasonal tracks motorable with 4-WD vehicles connecting the settlement of Hamashkoreb to Derudeb (in the W) and Tokar (E of the area) serve as the best access to the south-southwestern and eastern parts of the area, respectively. The valleys and sandy plains in the region are by and large motorable during the dry season. Figure 1 shows the location and accessibility map of the Derudeb area.

No perennial river is known to exist, but several seasonal streams apparently dissect most parts of the study area. Among these, Khor Langeb is the most prominent one which drains through a rather rugged terrain in the central part of the area, southwards and then NE to the Baraka valley (Figure 4.1). With the exception to limited ones in the W, all the rivers in the area drain into the Langeb valley. In the western and southwestern parts the river systems show a southwesterly drainage to the River Nile through a rather moderate topography covered by sand. Both parallel and rectangular drainage patterns are widely distributed in the area, being significantly controlled by Pan-African and Cenozoic structures (Section 2.2.4).

Topographically the Derudeb area makes part of the generally rugged and hilly terrain of the Red Sea Hills (RSH) of NE Sudan, that has been tectonically active since the Neoproterozoic. The elevation is higher in the central N and NW, and it gradually decreases towards S and SE. In the NE the highest peak of 1326 m above m. s. 1. occurs S of Jibal Arqawi, and an elevation of over 1200 m is reached on the uplifted block of Jibal Adar Ribad. Towards the eastern part of the same ridge the topography abruptly falls, reaching the lowest elevation of about 90 m in the Baraka valley. With the possible exception to isolated ridges, the morphology appears generally matured and less uneven in the SE, whereas to the N it is rather rugged. Figure 6.3 shows the elevation distribution of the Derudeb area.

The RSH is characterised by an arid to semi-arid climatic conditions. The summer is dry and hot, with temperatures reaching well over 45°C in the months March to October. In winter the temperature ranges between 25°C and 10°C during the day and night times, respectively. The rainy season falls between the months of July and September, with possibly a little precipitation also in the winter.

The RSH in general, and the study area in particular, is dominantly populated by the Beja ethnic group. The Hadandawa and Beniamir tribes of this group, who also speak their respective tribal languages, dominate the western two-third and the eastern one-third of the map area, respectively. Both tribes lead an exclusively nomadic life, mainly breeding camels, goats and sheep. In a few instances they practice seasonal farming of usually sorghum. The Derudeb township, after which the map sheet has been named, is the largest settlement in the area followed by Hamashkoreb in the central S. Scarce hand dug wells in valleys and areas covered by Quaternary sediments remain the principal source of water in the Derudeb region.

Vegetation is generally scarce in the Derudeb area, and rock exposure is very good, making remote sensing applications for geological studies highly feasible. Acacia trees and sparse bushy plants occur along relatively plain areas whereas ridge slopes are practically devoid of vegetation. Along major drainage channels fairly abundant dome trees are not uncommon. The Odi plain in the central S (Figure 4.1) is the only area where pronounced vegetation occurs throughout the year

and where farming is often practiced.

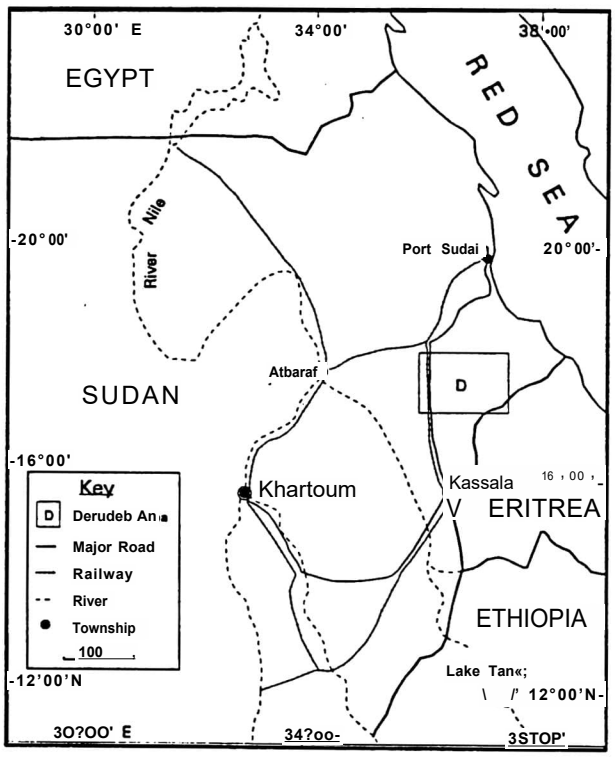

Figure 1.1. Location and accessibility map of the study area (Derudeb map-sheet, NE 37-1).

1.2 Previous Works

The Derudeb area is among the least studied regions in the RSH of Sudan. Delany (1956) produced the first geological map of the map sheet (previously 46-1, now NE 37-1) at the scale of 1 : 250 000. According to her the area broadly consists of undifferentiated gneisses and volcano-sedimentary schists for which she introduced the term Odi Schist, foliated granites, Tertiary volcanics and Mesozoic sedimentary rocks. She also described the Tihilla ring complex in the NW and the various volcanic and sedimentary cover rocks of the Odi area in fair detail. She identified intraformational sediments within the younger volcanic sequence. The basement rocks were obviously less studied and structural data were poorly documented. The geology of the area has also been less contained in the context of the regional setup.

Ahmed (1977) carried out a detailed study on the petrology and evolution of the Tihilla igneous complex in the northwestern part of the area. He described the complex as a shallow-level post-orogenic ring structure with generally alkaline character that possibly evolved through magmatic differentiation.

Between the late 1970's and early 1980's a number of more systematic works over the geology of the RSH at large were conducted. In a technical cooperation programme between the Soviet Union and the Sudan Geological and Mineral Resources Department, the "Technoexport Project" was engaged in regional aeromagnetic and gravity surveys over the RSH, E of longitudes 36°00'and N of latitude 16°00' all the way to the Egyptian border, during the years 1970-74. This study resulted in the production of aeromagnetic and gravity anomaly maps at 1 : 200 000 and 1 : 500 000 scales, respectively. This work was followed by detailed investigations of target areas selected for mineral exploration, including trenching and pitting, until 1978. The Derudeb area was mainly covered by the regional studies.

The Bureau de Recherches Geologiques et Minieres (BRGM) in cooperation with the Geological Research Authority of the Sudan (GRAS) (1988) conducted a geological mapping over the RSH at 1 : 1000 000 scale as part of the regional geological and mineral prospection programme in the Sudan. According to this work the Derudeb area is largely built up of volcano-sediments of greenschist facies, andesitic volcanic rocks, and metasediments of amphibolite facies rocks intruded by syn- to late-orogenic granitoids, all of which are presumably of Proterozoic age. Cenozoic volcanic rocks have also been identified. As a result of this work the sulphide and manganese mineralisations near the Abu Samar valley and the wolframite occurrence on the granitic ridge of Jebel lyub, both in the far NW (Figure 4.1), were temporarily explored.

More recently Hassan (1991) and El Labib (1991) conducted detailed geologic studies over adjacent areas in the central part of the map sheet. Hassan (1991) dealt with the classification of the Cenozoic rocks in the Odi area and ascribed their occurrence to the Red Sea rifting and the associated

extensional graben structure, with their geochemistry indicating characteristics of Mid Oceanic Ridge Basalt (MORB). El Labib (1991) focused on the petrology and structure of the post-orogenic ring complexes, in addition to syn- and syn- to late-orogenic emplacements, in the area. He ascribed them to characteristically subduction-related within-plate and syn-collisional magmatism, respectively.

An adjacent area to the E (S of Tokar) was studied by Kroner *et al.* (1991). According to this work the metavolcanic rocks in the area represent an early expression of extensional tectonics in an evolving arc complex with an associated back-arc basin. These authors interpreted the involved arc terrane as one of the oldest in the Arabian-Nubian Shield (ANS) with considerable growth of juvenile crust some 840-870 Ma ago, and that collided with the African continent some 720 Ma ago. Drury and Berhe (1993) also identified the area W of the Baraka Suture as a crustal segment older than the area to the E on their remote sensing based study of northern Eritrea.

Some reference to the geodynamic settings of the Abu Samar sulphides in the NW, (Figure 4.1) and the adjacent rocks, as representing an ophiolitic sequence were first made by Abdel Rahman (1993) based on rock assemblages and the associated exhalative sulphide mineralisation. He identified mafic-ultramafic rocks structurally overlain by association of silicified barite, quartzite, ochres, manganese ores and iron gossans all of which overly massive volcanogenic copperiferous sulphide deposits. The structural development of the Emasa shear zone, just NW of the map area, has been described by Wipfler (1994) whereby up to four deformation events were distinguished. According to this work the 0.5-1 km wide and about 5 km long Abu Samar Ophiolite belt is related to the northern Emasa Shear Zone through a rift mechanism that preceded the collision of the Haya and Gebeit Terranes (Figure 2.1). In both works a southeasterly plunging slab has been assumed for the Abu Samar Ophiolite during this accretion event.

1.3 Present Work

1.3.1 Objectives

Available geological maps covering the Derudeb area are either too old (eg. Delany, 1956; 1 : 250 000) and need principal contextual improvements, or too general (eg. GRAS, 1988; 1 : 1 000 000) and demand remapping with a reasonable detail. The Derudeb area, therefore, lacks any systematic geological map at a scale that might be used as a base for future exploration activities. The area is among those geologically least known in the RSH, and it has only been broadly contained in the crustal accretion models proposed for the Nubian sector of the ANS in the last two decades. Furthermore, the existing additional data pertaining to the Derudeb map sheet such as aeromagnetic, gravity and topographic maps, which are from different sources, of varying scale and quality are poorly documented and were hardly used in conjunction with each other.

Within the framework of Special Research Project "Geological Problems in Arid and Semi-Arid Areas, NE Africa (SFB-69)" the Derudeb area was selected as a pilot map sheet by the remote sensing subproject F5/E4. The following were the main objectives of the present study.

1. To conduct a geological study of the Derudeb map sheet (NE 37-1) of the southern RSH, Sudan, with the production of a geological map at the scale of 1 : 250 000, by principally using remote sensing methods and Geo-Information System (GIS) techniques, together with limited field data. This work was also expected to present the geological set-up of the area in the context of the regional geological models proposed for the surrounding region.

2. Digital image processing of Landsat TM and MSS data for enhancement of lithologic and structural information, and thereby facilitating improved visual geologic interpretation. This also includes evaluations of some image processing methods, with the aim of detecting gossans associated with sulphide and gold mineralisations (as alteration markers) in the area, using Landsat TM data.

3. To establish the effect of desert varnish on different rock types, particularly in mapping gossan bodies, in the context of Landsat TM data.

4. Systematic processing, visualisation and interpretation of aeromagnetic and gravity anomaly data in order to augment the geologic understanding of the region, and their integration with other data (Landsat, topographic, mineralogical, geological and GPS) pertaining to the Derudeb area in a Geo-information System (GIS).

1.3.2 Methods of investigation

Field methods

One reconnaissance visit to the region (2 - 25.11.92), and two field trips to the study area with a total of 21 days were conducted between November 8 - 23.1993 and November 9 - 16.1994. Geocoded and processed images at a scale of about 1 : 100 000 were used as base maps in addition to topographic maps obtained from the Sudan Survey Department at the same scale. Verifications of the preliminary interpretation maps were conducted during these times, and structural measurements were also made. Furthermore, several rock samples were collected, among which 62 were prepared for further microscopic, spectral and/or chemical analyses. Observation points were recorded during field campaigns using a Global Positioning System (GPS) receiver (Trimble-Scout).

Laboratory methods

The collected rock samples were cut for thin sections and analysed for rock identification, micro-structural information, and for establishing metamorphic grades in the case of basement rocks. Extent and type of alterations and/or weathering were also noted.

Chemical analysis aimed for determining the iron and manganese concentrations for the exposed surfaces of 15 rock samples was conducted at the Technical University of Berlin, Germany, by Dr. G. Matheis. Details of the procedure are described in Section 5.3. Reflectance measurements of exposed and cut surfaces from selected rock samples in the wavelength 0.4-2.5 jum were conducted under laboratory conditions with an aim of establishing the effect of desert varnish on Landsat TM data. Few samples with desert varnish were also processed by P. Böttcher for Scanning Electron Microscope. Details of the analytical procedure are given in section 5.1.

Absolute whole rock ages of seven samples from the Cenozoic volcanic rocks were determined using K-Ar (and partly Ar-Ar evaporation) techniques at the University of Leeds, UK, by D. C. Rex. The adopted analytical procedures are described in Rex (1994).

For the purpose of mapping the Derudeb map sheet part of Landsat TM data covering the Odi subscene (of about 77x62 km^2) was selected as a test-site based on the diversity of lithologies available in the area, in order to save computer memory and processing time. The selected subscene was digitally processed whereby several enhancement techniques were applied in the context of lithologic discrimination and structural mapping (Section 4). The image processing procedure with substantial results was applied to the data covering the whole of Derudeb map area and used as a basis for image interpretation, with additional information also from images obtained by other enhancement techniques. Hard copy outputs from an IRIS-3047 printer were obtained at a scale of 1 : 170 000 for visual geologic interpretation.

During the image interpretation methods akin to photogeological interpretation were used. Different lithologies have been considered as a unit when among others they are primarily characterised by a distinctive and substantially homogeneous spectral response, consist dominantly of one lithologic type or combination of types, have easily recognizable geologic boundaries, and are large enough to be represented on the geologic map at the desired scale of 1 : 250 000.

In addition to the interpreted geological map analogue aeromagnetic, Bouguer gravity, residual gravity and topographic data were digitized and integrated with the other digital data to produce a GIS database (Section 6). This was followed by data visualisation, analysis and interpretation in a geological context. Information from field work,

Landsat image processing and interpretation, and GIS database were then merged and analysed to produce the final geological map at 1 : 250 000 scale. Figure 1.2 shows the procedure adopted for mapping in the Derudeb area.

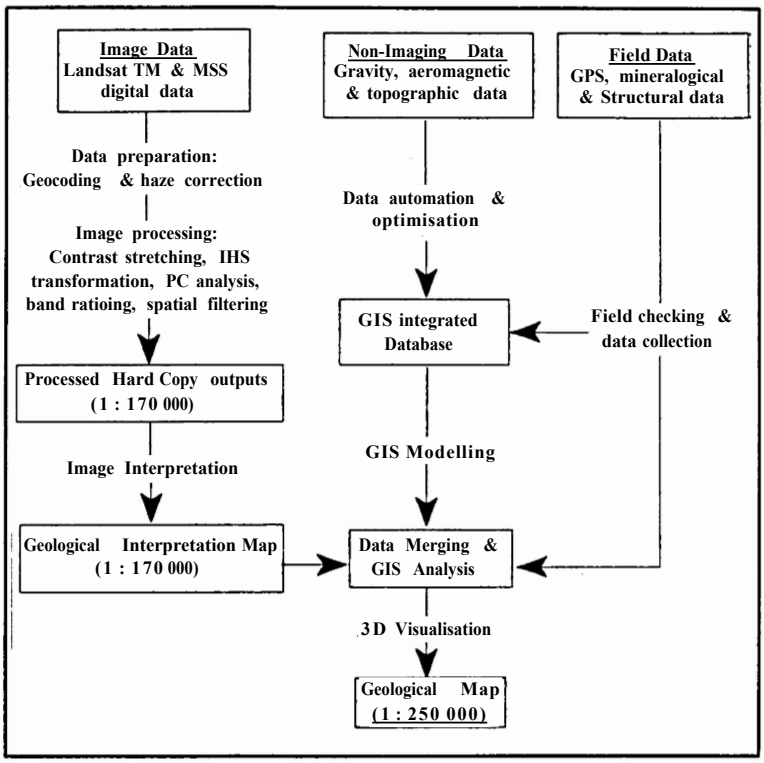

Figure 1.2. A flow diagram showing the procedure adopted for preparation of the geological map of sheet Derudeb (NE 37-1) at the scale of 1 : 250 000.

2 GEOLOGY

2.1 Regional Settings

The basement rocks of the Sudan and the adjacent areas can be grouped into two major domains associated with different geodynamic environments: the older sialic continental plate with its high grade gneissic complexes, and the younger juvenile ANS (Vail, 1988). The former is generally constituted by granulite facies gneisses and is believed to be of Archaean age (older than *ca.* 2500 Ma). In the Sudan, this reworked pre-Pan-African sequence (Abdel Rahman, 1993) is known to occur mainly in the southwestern part, along the lower sections of the Nile valley, and also in the W and NW bordering Chad and Libya, respectively, presumably constituting the older Nile Craton (Vail, 1988). Rocks of this group are migmatitic ortho-gneisses, biotite-hornblende gneisses, calc-silicates, quartzite, and are not known to occur in the RSH.

The ANS is understood to encompass the area E of the River Nile extending over the RSH of the Sudan and Eastern Desert of Egypt up to western Saudi Arabia (Kroner *et al.,* 1987; Vail, 1988), although the recent work of Schandelmeier *et al.* (1993) is not insignificant to raise doubts as to its western limits. It has been identified as part of the Pan-African crustal accretion episodes of generally Neoproterozoic age; *ca.* 1100-500 Ma (eg. Gass, 1981). Lithologically the ANS is constituted by crystalline calc-alkaline volcano-sedimentary sequences of rocks, calc-alkaline granitoids and migmatites, and mafic-ultramafic complexes (Drury and Berhe, 1993) mantled by a thick sequence of undeformed Phanerozoic cover in NE Sudan, western Saudi Arabia and the Eastern Desert of Egypt (Vail, 1988). Prominent shear zones and major transcurrent fault systems with varying orientations (eg. Abdelsalam and Stem, 1993) in addition to dikes of both acidic and basic composition ranging in age from Precambrian to Tertiary (eg. Vail, 1985, 1988) are known to occur in this region.

Stratigraphically, between these two major domains, rocks of Lower-Middle Proterozoic age *(ca.* 2500-1000 Ma) are thought to widely occur in the Sudan (see Vail, 1988). In the RSH they comprise acidic gneisses, hornblende schists, micaceous psammites and marbles usually in the amphibolite facies of regional metamorphism (Vail, 1988). Although doubts about the latter group of rocks, particularly in reference to the RSH, still exist (eg. Kroner *et al.,* 1987) some recent investigations, supported by geochronological and isotropic constraints, however, suggest the involvement of components from older crust in parts of the Eastern Desert (Sultan *et al.,* 1990) and the RSH (Kroner *et al.,* 1991). Drury and Berhe (1993) also put forth a similar interpretation for part of northern Eritrea mainly based on interpretation of images from Landsat and Large Format Camera.

Based on the notion that dismembered ophiolitic sequences and associated shear zones represent discrete sutures (eg. Berhe, 1990) Vail (1985) subdivided the ANS into different tectonic terranes. Kroner *et al.* (1987) further promoted this approach and defined five distinct terranes in the southern part of Eastern Desert and the RSH. From S to N they are known as Tokar, Haya, Gebeit, Gabgaba and Gerf Terranes (Figure 2.1). Lithologic similarities corroborated by geochemical and geochronological data have also encouraged broad correlations across the Red Sea (eg. Kroner *et al.,* 1987, 1991; Camp, 1984). Accordingly, the Haya Terrane has been correlated with the Asir Terrane, and the Gebeit Terrane has been interpreted to be an extension of Hijaz Terrane of Arabia (Stem *et al.,* 1990; Kroner *et al.,* 1987, 1991). Figure 2.1 shows the different terranes of the ANS and the respective sutures.

On the basis of the already available data, Shackleton (1994) attempted to bracket ages of the various magmatic activities in parts of the Nubian Shield. According to this work ophiolites of the Nakasib Suture range between 870-839 Ma, the lower age limit demarcating the obduction age of

the ophiolites. The associated arc magmatism, represented by calc-alkaline metavolcanics and tonalite-granodiorite intrusives, ranges between *ca.* 880-700 Ma. In parts of the Haya Terrane syn-orogenic plutons and metavolcanics of 870-830 Ma old have been reported by Kroner *et al.* (1991). Post-orogenic plutons in these areas are believed to be about 720-550 Ma old (Shackleton, 1994).

One of the proposed tectonic models for the Nubian Shield in particular assumes progressive accretion of intra-oceanic island arc and back-arc basin complexes onto hinterlands along ophiolite-decorated sutures (eg. Embleton *et al.,* 1983; Kroner *et al.,* 1987). Other workers have ascribed the evolution to a rather repeated rifting and closure of an older crust that had intermittently developed into oceanic basins (eg. Stem *et al.,* 1991; Abdel Rahman, 1993). In the latter case the different ophiolites in the region possibly denote the old rift-related structures. A Wilson Cycle model between these end-member models was also proposed by Abdelsalam and Stem (1993). In all cases it is generally agreed that the accretion tectonics of the RSH progressed from S to N (Shackleton, 1994), younging from Tokar Terrane through Haya, Gebeit and Gabgaba terranes to Gerf Terrane, in the same direction.

The major rock associations in the Nubian sector of the ANS may be grouped into four: the older gneissic complex, arc assemblages, ophiolitic suites and granitoid intrusives (eg. Vail, 1985; Kroner *et al.,* 1987). The most commonly adopted name for the group of high grade rocks in the RSH is the "Kashebib Series" (Gabert *et al.,* 1960). It has been described as consisting of supracrustal metasedimentary gneisses and migmatites regionally metamorphosed under amphibolite facies conditions (Vail, 1988; Hassan, 1991). The primarily metasedimentary rocks in the northwestern part of the Derudeb map area, also known as "Toilik Series", are considered to be correlative with this sequence of rocks, and all of them are generally thought to be of Lower-Middle Proterozoic age (Vail, 1988). The Kashebib Series is known to structurally occupy a lower position in the stratigraphic sequence of the RSH (Abdel Rahman, 1993).

The calc-alkaline volcanics and volcanoclastic arc assemblages, also known as "Nafirdeib Series" (Gabert et al., 1960) or "Greenschist Assemblages" (Vail, 1988) in the Sudan, are widely distributed over the RSH. These rocks appear generally less deformed and metamorphosed than the Kashebib Series and are, therefore, considered to be younger (Kroner *et al.,* 1987). In the Derudeb area a similar rock association has been termed as "Odi Schists" by Delany (1956). Embelton *et al.* (1983) suggested a lateral transition between these greenschist rocks and the high grade metasediments, but implied each to constitute a distinct crustal entity.

Ophiolitic sequences of rocks in the RSH are often thought to represent boundaries between old discrete crustal segments (Berhe, 1990). They are interpreted as younger rock associations that were deformed during the different accretion tectonics (eg. Kroner *et al.,* 1987). One such belt is the Amur-Nakasib Suture (Figure 2.1) that is believed to demarcate the boundary between the Gebeit Terrane (830-700 Ma) in the N and the Haya Terrane (900-800 Ma) in the S (Abdelsalam and Stem, 1993). Almond *et al.* (1989) suggested an age older than 720 Ma for the same suture, in agreement with the time of accretion in the ANS (Abdelsalam and Stem, 1993). Recent work by Abdel Rahman (1993) suggests that the rock association in the area of Abu Samar valley in the NNW part of the map area (Enclosure) also represents an ophiolitic sequence with SE subduction. Wipfler (1994) extended this idea and related the Abu Samar ophiolite with a thrust zone along the nearby Himasa Shear Zone to the N.

Large masses of gabbroic to granitic plutons, to which the term Batholithic Granites has been applied, are widespread in the RSH (Vail, 1988). Klemenic and Poole (1988) identified two phases of granitoid plutonism in the RSH: an early diorite/granodiorite phase 815-724 Ma ago, and a younger granitic phase of 717-515 Ma old. Furthermore, they ascribed these two granitoid groups to subduction-related emplacements along continental margins and fractionates associated with volcanic arcs, respectively. In the area SW of Nakasib Suture, Küster (1993) has related gabbro-diorite-tonalite associations with the beginning of a convergent plate margin tectonics earlier than 809

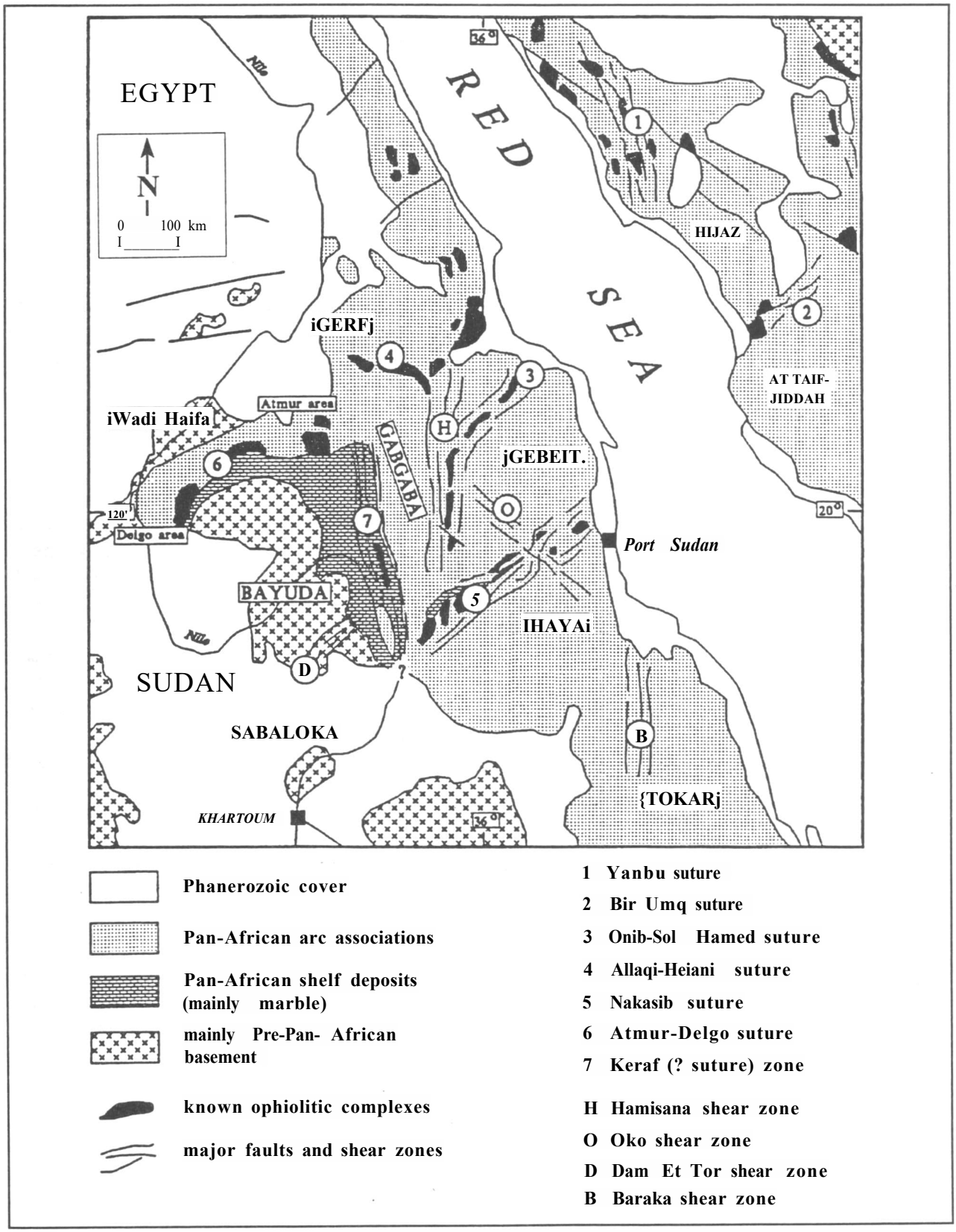

Figure 2.1. The different tectonic terranes of the Red Sea Hills and its surrounding areas decorated by ophiolitic sutures. After Schandelmeier et. al. (1993).

Ma ago, and the intracontinental magmas of about 525 Ma old with the end phase of subduction related magmatism in intra-oceanic island arc terrane. Kroner *et al.* (1991) obtained an emplacement age of *ca.* 650 Ma for post-orogenic granites S of Tokar (E of the map area). These are in good agreement with the time range of 720-550 Ma given by Shackleton (1994) for post-orogenic magmatism in the region. Anorogenic plutons of syenitic composition and dikes of bimodal character, thought to be unrelated to the Proterozoic evolution of the Nubian Shield, post-date all these rock types (eg. Vail, 1988).

Generally, sedimentary rocks of Ordovician to Quaternary age, and other post-Pan-African sequence of rocks, are widely exposed in the Sudan (Vail, 1988). On the other hand such rocks are rare in the RSH. Sedimentary rocks of mainly Jurassic to Cretaceous age (GRAS, 1988), known as Nubian Supergroup (Vail, 1988), whilst widespread in northern and central Sudan, are known to occur in a couple of localities in this region. According to Semtner (1993) the sediments in Jebel Dirurba area, NW of Port Sudan, are of Ordovician age for they contain Cruziana. She also recognised minor Mesozoic strata, and ascribed the whole sequence to an old large basin that originally extended over northern Africa and central Arabia. Tectonic movements that produced graben structures are responsible for their preservation in the Dirurba area (Semtner, 1993). The sedimentary rocks unconformably resting over the basement rocks of the Derudeb area are believed to be part of the Nubian Supergroup (Hassan, 1991).

Volcanism has been active in the Sudan during the Cenozoic invariably in the form of intraplate magmatism although most such centres presently exhibit dormant character (Vail, 1988). The opening of the Red Sea, as part of the East African Rift System, appears to be the major event in the NE Sudan, and the Afar rift to the south, that is linked to this event. In adjacent areas like Eastern Egypt, Yemen, Saudi Arabia and Ethiopia similar volcanic activities, mainly of Tertiary age, are also well known and have been ascribed to a large mantle plume that extended for about 2000 km (eg. Almond, 1986; Menzies *et al.,* 1992). The volcanic rocks of the Dirurba area, close to Sasa Plain NW of Port Sudan, though less studied, are thought to be associated with pre-Red Sea uplift/ doming and rift structures (Semtner, 1993). In addition, a sequence of volcanic rocks known to occur in the Derudeb area of the southern RSH have also been interpreted to represent a similar rift-related phenomenon (Hassan, 1991). On either sides of the Baraka Suture/ Lineament to the E, comparable sequences of rocks have been identified and related to the same Cenozoic volcanism (GRAS, 1988).

2.2 The Derudeb Area

According to the terrane classification proposed by Kroner *et al.* (1987) the Derudeb area forms part of the Haya Terrane, bounded to the N by the NE trending Amur-Nakasib Suture and to the SE by the submeridionally striking Baraka Suture/ Lineament (Figure 2.1). It is closely delimited by the less known Abu Samar Ophiolite (Abdel Rahman, 1993) and the Himasa Shear Zone (Wipfler, 1994) to the NNW.

In the following sections the major lithologic units are discussed following a lithostratigraphic sequence established by considerations of the regional and local geological settings. Structural developments in the area are then dealt with separately adopting the same approach. Table 2.1 gives the established lithostratigraphy of the rocks mapped in Derudeb area, including possible regionally correlative/known names. Descriptions given below refer to the geological map of Derudeb, where major locality names are also indicated (Enclosure). The prefixes Jibal (J.) and Khor (K.) that are locally used to imply mountain or mountain chain and drainage channel or valley, respectively, have been adopted accordingly.

2.2.1 Stratified basement rocks

High-grade metamorphic rocks

High-grade metamorphic rocks found in the area are mainly quartzofeldspathic and graphitic gneisses, migmatites, amphibolites, quartzites, marble, in addition to minor gametiferous micaschists and other psammitic schists. They are extensively exposed S of the Adadi Thrust and Transpressional Shear Zone (ATTSZ) in the eastern and southeastern parts of the map area, and partly being covered by the Cenozoic volcanics in the central S. To the E they appear to be bounded by the Baraka lineament, whereas towards the SW their limit is less obvious. A correlative association of rocks known also as "Toilik Series" is exposed NE of the Tihilla ridge in the NW (also Kroner *et al.,* 1987). All the above rocks invariably occupy a subdued topography, attained more likely through matured morphology, with the exception of those exposed over the later uplifted Jibal Adar Ribad in the NE. These high-grade rocks are all thought to represent the oldest rocks in the area and thus correlative to those known as "Kashebib Series" (Gabert *et al.,* 1960) in the rest of the RSH. The rocks were generally metamorphosed under mid-amphibolite facies conditions (see also Vail, 1988).

The amphibolite is chiefly constituted by hornblende crystals, with major retrogressive overprints of epidote, and some feldspar and micas. Growth of muscovite and iron oxides at the expense of hornblende and further chloritization of muscovite during the retrograde phase have also been noted. The minerals are often elongated and well aligned parallel to the main foliation. At outcrop scale they may display a segregation of feldspars to define a gneissic texture. In few instances (W of J. Qawayateb and E of J. Arqawi) amphibolite bands have been observed as circular structures close to shallow syn- to late-orogenic intrusives. The latter are well distinct on the processed satellite imageries (Section 4.3.1).

In thin-section, the graphitic gneiss contains potash feldspar, quartz and relicts of muscovite in addition to the dominant graphite. In one case rounded titanite has been observed in this unit, possibly indicating the high grade of metamorphism witnessed by the rock. In addition to the well developed gneissic texture the rock exhibits effects of strong migmatization, indicating significant liquid movement under high temperature conditions.

Quartzitic bands observed in association with these rocks often form rounded hills. The bands are frequently fractured and folded. In the southern part of the area they display a brownish colour in hand specimens due to ferruginization; a feature that makes them easily recognizable on the processed images (Section 4.3). The marble layers associated with the quartzofeldspathic gneiss and the amphibolite are more frequently whitish, poor in iron, and sugary in texture. Close to J. Qawayateb in the E, they occur in association with minor bands of unmapped pyroxenite.

This sequence of graphitic schist/gneiss, marble, intercalated quartzite, amphibolite and guartzo-feldspathic gneiss is interpreted to probably define an association of originally deep-sea sediments deposited in a reducing environment, followed by shelf sediments towards the SE. This association possibly represents a previously NE-SW extending passive continental margin, as also shown by the high percentage of cement quartz in the marble, whereby the presently amphibolites were extruded as intra-continental volcanics. This interpretation is comparable to that suggested by Kroner *et al.* (1987) for a similar association in the Sasa Plain (S of Gebeit) and S of Wadi Amur.

Metavolcano-sedimentary rocks

This bulk name refers to the greenschist facies (in few cases up to amphibolite facies) rocks that often define a rugged topography in the map area. The rocks are widely exposed in the western, central and northern parts of the study area. The major rock types constituting the metavolcanic sequence are meta-andesite, metatuff, metarhyolite and various schists (see also Hassan, 1991; El Labib, 1991) with very limited basic components. The metasediments are mainly graphitic schists, marble, meta-conglomerate, mica schists, minor

metamorphosed siltstone and mudstone. Rocks belonging to this group are thought to be correlative to those known as "Nafirdeib Series" (Gabert *et al.,* 1960) in the rest of the RSH or called as "Odi Schist" by Delany (1956) in the map area (Table 2.1). These rocks have broadly been identified as volcanic arc/back arc assemblages in most parts of the RSH (eg. Kroner *et al.,* 1987, 1991; Abdelsalam and Stem, 1993).

A two-fold subdivision of this sequence was identified in the Derudeb area: rocks which exhibit some evidence of amphibolite facies metamorphic conditions, and rocks generally ascribed to greenschist facies. The former are exposed around the ATTSZ and in a close spatial association with large plutonic bodies. In these cases the high metamorphic grade has been related to either intense shearing and/or contact metamorphic imprints induced by large granitoids (see also Kroner *et al.,* 1991). On the processed images these rocks display a spectral signature well comparable to the high-grade rocks, possibly due to the presence of iron-bearing minerals (see Section 4.3, 4.4). The greenschist assemblages occur extensively exposed N of this shear zone.

Table 2.1. Lithostratigraphy of the rock units in the Derudeb area in relation to known nomenclatures and age limits obtained for correlative units in parts of the RSH, Sudan.

Red Sea Hills	Derudeb Area	Lithology	Remark
Recent Sediments	Quaternary Deposits	Wadi deposits, unconsolidated sediments	
Tertiary Volcanics (GRAS, 1988)	Odi Volcanics & Adar Ribad Volcanics	Quartz porphyry Rhyolite Dacite Basalt	Red Sea rift-related volcanics *(ca.* 31-22 Ma, this work)
Nubian Supergroup (Vail, 1988) Dirurba Formation (Semtner, 1993)	Odi sedimentary rocks	Sandstone, Siltstone, Mudstone, limestone and Conglomerate	Fluvial and marine sediments (Early Paleozoic (Semtner, 1993) - Cretaceous (Vail, 1988))
Granitoids	Post-orogenic Granitoids	Granite, Gabbroids	Within-plate magmatism *(ca.* 720- 550 Ma; Shackleton, 1994)
	Syn-late-orogenic Granitoids	Metagranite, Metagabbro, Talc Schist, Serpentinite, Metagranodiorite, Metaharzburgite, Metapyroxenite, Talc Schist	Volcanic arc, Syn-collisional intrusives *(ca.* 815-724 Ma; Klemenic and Poole, 1988)
	Syn-orogenic Granitoids	Metagranite, Metagranodiorite	
Nafirdeib Series (Gabert et al., 1960) /Odi Schist (Delany, 1956)	Metavolcano-sedimentary Sequence	Metasediments (metapelites, marble, graphite schist , metaconglomerate)	Pan-African metavocano-sedimentary sequence (ca. 800-900 Ma arc/back-arc assemblages; eg. Abdelsalam and Stern, 1993)
		Intermediate - acidic volcanics (metarhyolite, meta-andesite, metatuff, various schists), minor metabasalt	
Kashebib Series (Gabert et. al., 1960) /Toilik Series (cf. Vail, 1988)	High-grade Metamorphic Rocks (Gneisses)	Gneisses (amphibolite, quartzite, quartzofeldspathic gneiss, marble, graphite gneiss)	Presumably Pre-Pan-African crustal segment *(ca.* 2500-1000 Ma; Vail, 1988)

The metarhyolites are generally fine to medium grained and foliated rocks mainly composed of quartz, plagioclase, and orthoclase with biotite as the only mafic mineral. The meta-andesite often exhibits a porphyroblastic texture represented by plagioclase. Biotite is present in small amounts mostly being altered to chlorite, and iron-oxides make up the major part of the accessory minerals. The metatuff is well exposed in the NW, and it is characterised by plagioclase porphyroblasts in a fine grained groundmass of microcline, biotite, chlorite and epidote. Iron-oxides and zircon are the accessories. Amphibole is the main constituent in the chlorite-amphibole schists, where epidote and chlorite, at the expense of amphibole, are also abundant in retrograded varieties. El Labib (1991) ascribed the geochemical characteristics of these metavolcanic rocks to arc magmatism that may extend to within-plate environment.

The graphitic schists are similar to those occurring in the high-grade rocks, but lack migmatisation effects and gneissic texture. The metapelites generally contain quartz, chlorite, muscovite, biotite and porphyroblasts of plagioclase. Calcite and sericite may be present in some varieties, with some iron-oxides, zircon and zoisite as accessories. Garnet-rich schists are also not uncommon nearby the chlorite-amphibole schists. The marble associated with these rocks is often banded, being distinct from those varieties associated with the high-grade rocks even on the processed images (Figure 4.1). Pyritisation appears to be a common feature in most of these rocks. The mudstone and siltstone derived schists dominantly contain quartz, sericite, and epidote, with minor biotite and graphite. Occurrence of meta-conglomerates containing pebbles from most of the above rocks has been reported by El Labib (1991). These metasediments are thought to occupy the core of a large synformal structure in central Derudeb overlying the dominantly acidic metavolcanics (also El Labib, 1991).

The stratigraphic relationship between the meta-volcanic and metasedimentary rocks has been difficult to establish mainly due to the repeated folding (Section 2.2.4) and frequent intercalations of the different rocks. Although the possibility of lateral transition can not be excluded (Embleton *et al.,* 1983), good examples of tectonic contact between these two groups of rocks exist in Derudeb area (Section 2.3).

2.2.2 Intrusive rocks

Plutonic rocks in the area include granites, granodiorites/diorites, gabbros, and ultramafic rocks. These rocks are believed to have been emplaced in different times in the tectono-magmatic history of the basement rocks in the area. They have accordingly been termed as syn-, syn- to late-, and post-orogenic granitoids.

Syn-orogenic granitoids

In the Derudeb area intrusives belonging to the syn-orogenic group are granitic bodies exposed in the SW close to the ATTSZ, in the NW associated with a similar ductile shear zone, and in the eastern part within the gneissic rocks. In the former case their emplacement appears to have been dictated by the shear and thrust zone. In all occurrences, except in the latter case where small elliptical bodies predominate, the rocks are characteristically elongated with the major axis trending NW-SE to E-W following older regional structures; a feature also revealed by aeromagnetic anomaly data (Section 6.5.1).

The rocks are generally deformed, often deeply weathered, and are thought to be associated with the D_2/D3deformation events (Section 2.2.5) in the area. Their distinction from the syn- to late-orogenic granites is rather difficult but cross-cutting relationships observed on processed Landsat images provide substantial clues (see below). According to El Labib (1991) syn- and early- to late-orogenic granitoids in the northern Derudeb area are related to volcanic arc and syn-collisional emplacements.

Syn- to late-orogenic granitoids

Metagabbros, metagranodiorites, meta-ultramafics and metagranites constitute the major rocks belonging to the syn- to late-orogenic granitoids that

comprise a significant proportion of the map area. They occur in different parts of the study area in various associations and magnitude, but they happen to be relatively widespread in the area W of the Adit-Langeb Lineament, with a preferred alignment along this structure (Section 2.2.4). Most of these rocks look partly fresh and massive, and they frequently display sharp to diffuse contacts with the country rocks.

Metapyroxenite, metaharzburgite, serpentinite and serpentine-talc schists are the different types of meta-ultramafic rocks observed in the study area. In the NW the first two occur as discontinuous lenses close to a thrust fault having a southward dip. Few stretching lineations measured along this plane gave a dip of 55° towards S, possibly as an effect of later deformations. The rocks invariably form elongated ridges, and are often deformed, although some massive varieties are also not uncommon. In thin-sections the pyroxenite and harzburgite show partial alteration of large pyroxene and olivine crystals to serpentine. Epidotization effects were also observed in few cases. Serpentinised talc schists are well exposed in the SW along the western extension of the ATTSZ. In this area the ultramafics are strongly sheared, with well developed penetrative shear foliation, and occur as dismembered bodies of some hundreds of metres wide; for which reason they have been considered as tectonized lenses. They occur in association with marble, gabbroic rocks showing a layered structure, and amphibolites and chlorite-schists thought to represent metamorphosed basaltic lava. In the vicinity of J. Sanay in the SW presently unmapped minor occurrences of metapyroxenite and serpentinite have as well been observed in association with the gabbroic rocks.

The metagranites are well exposed along the prominent Adit-Langeb Lineament in the central Derudeb. They frequently measure over tens of kilometres in diameter, being often semi-elliptical in shape and forming a relatively subdued topography partly covered by sand and Quaternary sediments as an effect of deep weathering and erosion. At outcrop scale the metagranites show dense fracture systems. In this area they host several granitic younger dikes of latitudinal trend. The metagranites range from leucocratic to pinkish varieties and may look grey when the mafic constituent becomes significant. In thin-sections they are equigranular, coarse to medium grained with biotite as the major mafic mineral. A few quartz crystals with undulöse extinction are interpreted to suggest deformation effects. In the SW a good example of the emplacement relationship between the syn- and syn- to late-orogenic granitoids occurs where a younger syn- to late-orogenic granite with elliptical shape appears to have pushed aside the older elongated granite and the regional foliation (Figure 4.1).

The granitic body forming the Arqawi ridge in the NE is thought to belong to this group, despite the lack of evidence for deformation in the field, since it appears to have witnessed ductile shearings that affected the area. In this occurrence brownish colour that gets diffused away from the contact, as seen on the enhanced TM images (Section 4.3, Figure 4.1), is well displayed by the country rocks. This observation may be interpreted as an effect of heating from the pluton, whose distribution has been facilitated by the intense and cross-cutting fracture systems that probably favoured fluid movements in the area. This unit is also characterised by large negative Bouguer and residual gravity anomaly values (Section 6.5.2).

Metagranodiorites are limited to the northwestern part of the area, mainly W of the Adit-Langeb Lineament. The main body has an elliptical shape, with the long axis striking nearly E-W, and extending over tens of kilometres. Megascopically it is massive and coarse grained, with foliated texture observed in thin-sections. Hornblende appears to be the major mafic mineral, in addition to minor muscovite and biotite that at places become significant and gives it a grey appearance, where otherwise a granitic composition predominates. The unit has been intensively dissected by latitudinally trending younger dikes of mainly granitic composition and contains lenses of metapyroxenite presumed to be older. The meta-granodiorites in the Derudeb area may be roughly correlated to the early granitoids of 815-724 Ma (Klemenic and Poole, 1988) that have been ascribed to mantle-origin plutons emplaced above a Neoproterozoic subduction zone. The above described rock unit is not easily to be recognised from the Landsat images, but it is well distinct by its very low negative Bouguer and residual anomaly values (Section 6.5).

Metagabbros occur in the southwestern, southern, central and northern parts of the Derudeb area. Megascopically they are massive to poorly foliated, medium to coarse grained dark-grey rocks. One occurrence, N of the ATTSZ in the SW, is remarkable not only for its long extension over the NE-SW trending ridges but also for its association with unmapped marble, meta-ultramafics, and amphibolites probably representing metabasalts. Furthermore, the gabbroic rocks display a textural and compositional variation from medium grained (with finer varieties occurring at places) equigranular and massive looking ones to porphyritic types enriched by elongated plagioclase crystals that give the rock a leucocratic appearance and cumulate texture; a feature indicating a layered structure. In the rest of the map area the gabbroic rocks are often spatially associated with syn- to late-orogenic granites; a case described as ring complex by El Labib (1991). In most cases pyroxene (both ortho- and clinopyroxene) has been altered to amphibole and iron-oxides. In some samples olivine occurs as inclusions in plagioclase crystals, whereas in others the mafic components are lesser, giving it a dioritic composition. Most of these rocks are typified by a relatively higher negative Bouguer anomaly (Section 6.5.2).

On the processed image (Figure 4.1) a gabbroic body apparently surrounded by a granitic pluton is clearly displayed in the SE (E of J. Qawayateb) by the compositional contrast. This feature has been considered as a ring-structure, and it is presumed to be of late-orogenic emplacement for its much subdued topography unlike that of the younger post-orogenic intrusives described below.

Post-orogenic granitoids

The intrusive bodies included in the group of post-orogenic granitoids are by and large massive and circular in shape, with often sharp and steep contacts discordant to the country rocks and older tectonic boundaries. The granitoids are consistently massive except along the margins, coarse grained, with fine grained texture exhibited by those in dike forms because of faster cooling. El Labib (1991) related the geochemistry of late post-orogenic granites of the Derudeb area to an exclusively intraplate magmatism, possibly subduction-related.

The major occurrence of such rocks in the study area is the Tihilla ridge in the NW where a gabbro-norite body is rimmed by a younger granite. Granitic dikes of E-W strike and the regional foliation appear to be cut by these plutons. Ahmed (1977) described the Tihilla granitoids as shallow level intrusions that have likely evolved through magmatic differentiation and display a distinct structure. The gabbroic body yielded a K-Ar whole rock age of about 636 Ma whereas the granite from the same complex was dated at a maximum age of 597 Ma (Vail, 1988) by the same method. The Tihilla ring complex also displays a unique pattern of Bouguer and residual gravity anomalies, whereby the central gabbroic rock and the surrounding granite are characterised by relative low, and large negative anomaly patterns, respectively. Compositionally these rocks are comparable to their older equivalents.

The Jebel lyub ridge, NE of Tihilla, is one such post-orogenic granite that has been partly explored by the GRAS-BRGM geologists for its tungsten/ wolframite mineralisation. The rock is leucocratic, massive and medium to coarse grained in texture. Recent chemical analyses of samples from this unit showed anomalous W, Rb and F concentrations (G. Matheis, pers. comm.). The emplacement of these post-orogenic plutons is thought to be related to crustal relaxation which accompanied basement uplifting that followed the cessation of the accretion tectonics.

Ophiolitic rocks

The association of mafic-ultramafic rocks that are structurally overlain by an assemblage of silicified barite, quartzite, manganese ores and iron gossans all of which are underlain by the massive volcanogenic copperiferous sulphide deposit in the Abu Samar area (in the N) has encouraged Abdel Rahman (1993) to identify it as an ophiolite sequence. In this area the mafic-ultramafic assemblage consists of very coarse grained pyroxenite and hornblendite that grades into layered gabbro up the section, massive basalt and doleritic

dikes of a couple of metres thickness (Abdel Rahman, 1993). Most of the mafic-ultramafic rocks show slight effects of deformation, with the exception to bands of talc-schists that are possibly mantle derivatives. The ophiolite and sulphide association has been ascribed to a paleo-destructive plate margin (Abdel Rahman, 1993). Results from some chemical analysis of the amphibolites from Abu Samar area by Wipfler (1994) seem to indicate oceanic basalt.

As it has been described earlier, an association of strongly deformed ultramafics, mainly pyroxenite and talc schist, have been observed along the western extension of the ATTSZ (see Enclosure). In this area these rocks occur in association with fairly thick marble layers and gabbros that grade from very coarse grained ones with large elongated plagioclase crystals to medium grained massive looking varieties. The latter display a layered structure. In one locality N of the Odi depression a thin serpentine band has been observed, and SE of J. Arqawi (in the NE) deformed pyroxenite has also been noted in a couple of places, depicting the continuation of these rocks along the shear zone.

The observed rock association close to the ATTSZ and preliminary structural interpretation are fairly encouraging to assume a possible ophiolitic sequence. However, limited encounters of equivalents of basic volcanics, absence of sheeted dikes parallel to the shear zone etc. in addition to the lack of chemical analysis make this interpretation very tentative, at least at the present stage, and requires more investigations.

Dikes

In addition to the rocks described above there are dikes of both basic and acidic composition that occur in the basement rocks and are believed to be related to the Pan-African events in the region (see also Vail, 1993). One such occurrence is in the NW, E of Tihilla granite, where there are principally granitic, and minor dioritic, dikes that chiefly trend E-W for tens of kilometres and whose eastward continuation seems to have been terminated by the Adit-Langeb Lineament (Section 2.2.4). Aeromagnetic anomaly data also indicate a steep dip (Section 6.5.1) in this area. The dikes form swarms of few kilometres wide and are interpreted to represent the fracture zones that contributed to the emplacement of the younger Tihilla granite to the W, as they appear to be truncated by the latter. They were possibly emplaced after the D_2/D_3 NW-SE oriented compression has been released (Section 2.2.4), and they precede the intrusion of the post-orogenic Tihilla granite corollary to crustal relaxation. An absolute age dating of a similar granitic dike just NW of the Derudeb area gave an age of 633 Ma by the K-Ar technique (Vail, 1993). Most of the above describe units are upper crustal rocks and may imply less development of mountain range, or limited denudation levels since Pan-African, or combination of both.

The second set of dikes strike NW-SE and occur mainly in the S and SE. As seen on Landsat images, in the area SW of Hamashkoreb village they form a swarm of about 1.5 km wide and extend for over 6 km. Here also the dikes are dominantly granitic. The abundance of these dikes in the region is attributed to the widespread extensional tectonics following the regional compression and plate collisions during the Pan-African orogenesis (see also Vail, 1993).

Less prominent dikes with a submeridional trend also occur in the SW. They are often basic, less commonly granitic, and have been intruded into the metavolcano-sedimentary sequence of rocks. Vail (1993) described the N-S trending dikes in NE Sudan to be alkali in composition and correlates them with chemically similar rocks of 140-130 Ma old.

2.2.3 Phanerozoic cover rocks

Phanerozoic cover rocks in the area are mainly sedimentary rocks along the Odi-Langeb extension that are dominantly sandstones, and basic to acidic volcanic rocks, of which the latter make the major part. Lithologically the volcanic rocks are mainly basalt, rhyolite, dacite, quartz porphyry and minor tuff. They occur as two major and one minor exposures in the Derudeb area. In the central S (called herein “Odi volcanics”), where these rocks are most abundant, they define a N-S elongated

structure that is upto 28 km across, in its central part, and approximately 100 km long, extending further S out of the study area. The second exposure is in the northeastern comer of the map area on the western half of the uplifted mountain range of Adar Ribad (hereafter named Adar Ribad volcanics) whereas the third and the least significant occurrence is between the above two areas close to Khor Windi (Enclosure).

The Odi sedimentary rocks

The major rock types comprising the Odi sediments are sandstone, conglomerate and mudstone, in addition to limestone and marl beds reported by Delany (1956) and Hassan (1991). The sedimentary rocks occur mainly in the central S, along the Odi valley, after which they have been named, and also along the courses of K. Langeb and its tributaries to the N. They generally lie unconformably above the basement rocks. A basal conglomerate that grades upwards to sandstone frequently marks the lower part of the sedimentary sequence, although in one case (E of Hamashkoreb settlement) a paleo-soil of about 1.5 m thick has been observed between these sediments and the gneissic rocks. In many occurrences the angular unconformity has variable dips possibly indicating an uneven old topography. The sedimentary rocks exhibit variable dips; in the northern part they are subhorizontal whereas in the S they dip at 15-30° centrally towards the Odi depression. Their total thickness appears to be variable in response to weathering and the old morphology, ranging from few to some tens of metres with a general increase southwards *(ca.* 150 m at most). The top part of the sedimentary rocks are presently exposed at an elevation of about 480 m. This increase in thickness has been ascribed to variations either in the original depositional basin or in the extent and mode of uplift after deposition that prevailed in the area.

The sandstone is often poorly sorted, medium to coarse grained and brownish to whitish in colour. It mainly contains monocrystalline quartz and feldspar crystals with poor sphericity set in a cement comprised of iron-oxide, quartz and clay minerals. Primary sedimentary structures like cross-bedding and graded-bedding are well displayed and younging directions appear frequently up-right. Hassan (1991) classified the Odi sandstone as dominantly subarkose, with minor exposures showing arkosic and quartz-arenitic compositions. The basal conglomerate consists of poorly rounded quartz pebbles and clasts of the basement schists ranging from 5 mm up to 30 cm in diameter. The grain size generally gets coarser up the sections. The mudstone and siltstone are very fine grained and light coloured rocks that occur in beds of 1-3 m thick each.

According to Hassan (1991) the Odi sedimentary rocks generally form part of the Nubian Supergroup (Vail, 1988) known in the rest of the Sudan and represent a continental lacustrine environment. A generally Cretaceous age has been suggested for the Nubian sediments and those occurring in the Sasa graben, about 150 km NNW of Port Sudan (Almond, 1986). Later studies by Semtner (1993), however, ascribed the latter to a Lower Paleozoic age based on index fossils.

The various sedimentary rocks are also known to occur as intraformational layers, of often few metres thickness and partly containing rounded volcanic fragments, within the volcanic stratigraphy in parts of the Derudeb area. This observation indicates that the sedimentation process was intermittently interrupted by subaqueous volcanism and was finally dominated by rift-related subaerial volcanicity. The contact between the sedimentary rocks and the overlying younger volcanic sequence described below, is thus conformable.

The Odi volcanics

The Odi volcanic occurrence has been relatively more studied (eg. Delany, 1956; Hassan, 1991) not only for its well preserved succession of the different rocks but also for its relative accessibility permitted by its moderate topography and proximity to the main road. The type locality where the complete sequence of these rocks has been observed is on the sides of Jabal Oman, around the Khor Odi-Langeb confluence (Enclosure). Here a succession of interlayered basalt and tuff horizons lie conformably over each other, to be topped by

rhyolite and agglomerate, with a thickness totalling about 150 m. In this area the rocks dip 20-40° centrally towards the Odi depression. The observed stratigraphy has been summarised in Figure 2.2.

Basalt is the most widespread volcanic rock in this area, and up to 10 uninterrupted layers of variable thickness assumed to represent different flows were observed. Generally, the basalt is fine grained and massive, although amygdaloidal varieties are not uncommon, the latter being attributed to a possibly water-bearing environment during extrusion. The amygdules, and plagioclase phenocrysts, often increase in size and abundance up the layers. Mineralogically the basalts contain plagioclase (labradorite), olivine, augite and iron-oxides (magnetite), with the former two as phenocrysts in porphyritic varieties. Occurrence of olivine both as phenocrysts and groundmass is interpreted to indicate an under-saturated alkali melt. Flow folding has as well been noted at outcrop scale in a few instances. Spheroidal weathering is very common and iron oxidation effects give the rock a brownish colour on capping layers.

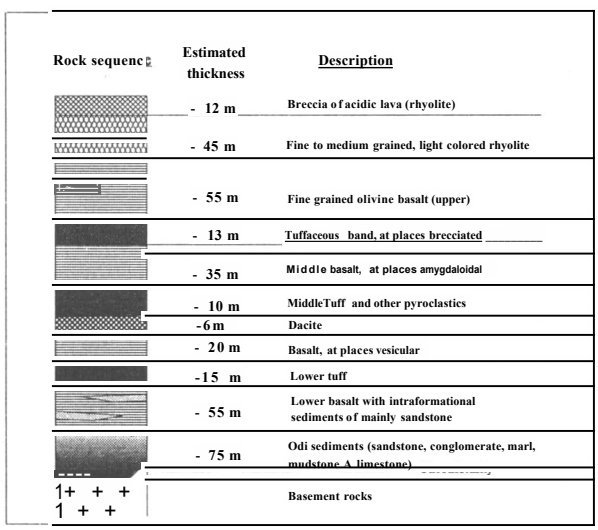

Figure 2.2. Generalised stratigraphic section of the Odi area (based on observations along Khor Tashalal). Rocks dip (-20°) consistently southwards. Section not to scale.

Two samples from the Odi area (Table 2.2) were dated for absolute age by a whole rock K-Ar methods at the Leeds University, UK. The sample from the bottom of the sequence gave an age of *ca.* 30.8 Ma whereas the one from the layer towards the top yielded an age of -26.6 Ma, depicting basaltic volcanism towards the Late Oligocene. The obtained ages conform with the relative stratigraphy observed in the area (Figure 2.2). These magmatic activities correspond very well with the early volcanism that occurred in the southern sector of the Red Sea, which the Derudeb area is a part, and are thought to have accompanied the initiation of rifting (Makris and Rihm, 1991). Hassan (1991) described the geochemical character of the Odi basalt as a subalkaline-tholeiitic, primitive, almost Mid-Oceanic-Ridge-Basalt (MORB) type. He further relates these rocks to an upper mantle partial melting derivation associated with the early phase of Red Sea rifting. Table 2.2 gives the radiometric ages obtained for some volcanic rocks of the Derudeb area.

Dacite occurs in one locality N of the Odi depression, lying conformably over the basalt. It is a brownish rock quite often with amygdules as large as 15 cm in diameter. The amygdules are ellipsoidal in shape and mostly filled with quartz, calcite and greenish (probably chlorite) material. The abundance of amygdules that gave a pumice like appearance, may indicate wet ground over which the lava flowed.

At least three tuff layers have been identified in the Odi area. The layers are 2-5 m thick and generally occur between the basalt and rhyolite units (Figure 2.2). Occurrence of tuffaceous layers within the basaltic sequence suggests intermittent explosive volcanic activity with more viscous magma. The rocks are fine grained, often weathered and whitish in colour. The tuff bands are discontinuous but persistent in the volcanic sequence S of Tashalal-Langeb Lineament and on the eastern part of the volcanic basin. A sample from the middle layer provided a whole rock K-Ar age of -28.3 Ma, and a step-wise evaporation of the same sample by the Ar-Ar method gave an age of 29.5±0.3 Ma (Table 2.2). These results are self-consistent as such small discrepancy in K-Ar and Ar-Ar methods may be ascribed to the fact that tuff often incorporates clasts of older rocks. The Ar-Ar evaporation generally gives a more reliable age, as compared to the K-Ar method.

Rhyolite, as the second most abundant volcanic rock in the area, is well exposed around the Odi depression. Where observed it conformably rests over the basalt and is characterised by moderately negative aeromagnetic anomalies (see Section 6.5). The rock is often of beige to reddish colour, fine to medium grained and porphyritic in texture. The phenocrysts are mostly potash feldspar, and spheluritic quartz occurs as the characteristic constituent. Flow banding is also well displayed in some varieties. A sample from the upper layer was dated at *ca.* 22.8 Ma by the K-Ar whole rock method. The age ranges obtained for the tuff and rhyolite layers are in good agreement with the magmatism of the central Red Sea region which took place as the volcanism that was initiated in the southern part propagated northwards (Makris and Rihm, 1991).

Quartz porphyry is exposed N of the Odi depression in two minor occurrences. It has a similar composition with the rhyolite but contains remarkably large phenocrysts of quartz and potash feldspar, up to 8 mm in diameter and over 5 cm long, set in a fine-grained groundmass. Vertical columnar jointing is apparently well developed. The acidic rocks (dacite, rhyolite and quartz porphyry) of the Odi area have been ascribed to lower crustal partial melting associated with the injection of the basaltic magma (Hassan, 1991).

The Adar Ribad volcanics

The Adar Ribad volcanics are represented by basalts and rhyolites. Like in the Odi area, here also the rhyolite lies conformably over the basalt which in turn rests unconformably over the basement rocks. In this area no sedimentary rocks equivalent to the Odi sediments have been observed between the basement and the volcanic rocks. This is interpreted to be related either to the early commencement of uplifting in this area that long preceded the Red Sea rifting and thus facilitated extensive erosion, or localized sedimentation in the Odi area in a lacustrine environment (see Section 2.3).

The basalts are compact, fine grained and dark coloured. They are compositionally similar to the Odi basalts but here no amygdaloidal and porphyritic varieties have been observed. The rhyolite also exhibits a composition similar to the rhyolite of the Odi area. The volcanic rocks in this area occupy the western half of the Adar Ribad ridge and invariably show a moderate (~ 40°) westerly dip. This structure is ascribed to tilting of the whole sequence following the uplifting of the western shoulder/horst of the Red Sea, being bounded to the W by the submeridionally striking Osir Walab Fault (see Figures 2.6 and 4.1).

Table 2.2. Radiometric ages obtained for selected volcanic rocks of the Derudeb area using K-Ar method. § shows samples also dated by Ar-Ar evaporation method.

Sample number	Stratigraphical unit	Location (Longitude , Latitude)	K_2O (Wt%)	vol ^{40}Ar rad (scc/g x IO^{5})	^{40}Ar rad (%)	Age (Ma)
98	Basaltic Dike	36°32'57" E, 17°4'H"N	0.304	0.0352	46.0	29.5±1
115	Adar Ribad Basalt	37°10'43"E, 17°30'56"N	0.154	0.0168	18.7	27.9±1
121 (§)	Adar Ribad Rhyolite	37°14'53"E, 17°38'59"N	4.718	0.4532	27.7	24.5±1
179a	Odi Rhyolite	36°42'54" E, 17°12'24"N	2.762	0.2460	54.3	22.8±1
179c (§)	Middle Tuff	36°43'17" E, 17°13'5"N	3.700	0.4099	61.9	28.3±1
183a	Upper Odi Basalt	36°40'37"E, 17°16'28"N	0.285	0.0297	13.1	26.6±1
183b	Lower Odi Basalt	36°40'30" E, 17°16'40"N	0.352	0.0425	18.7	30.8±1

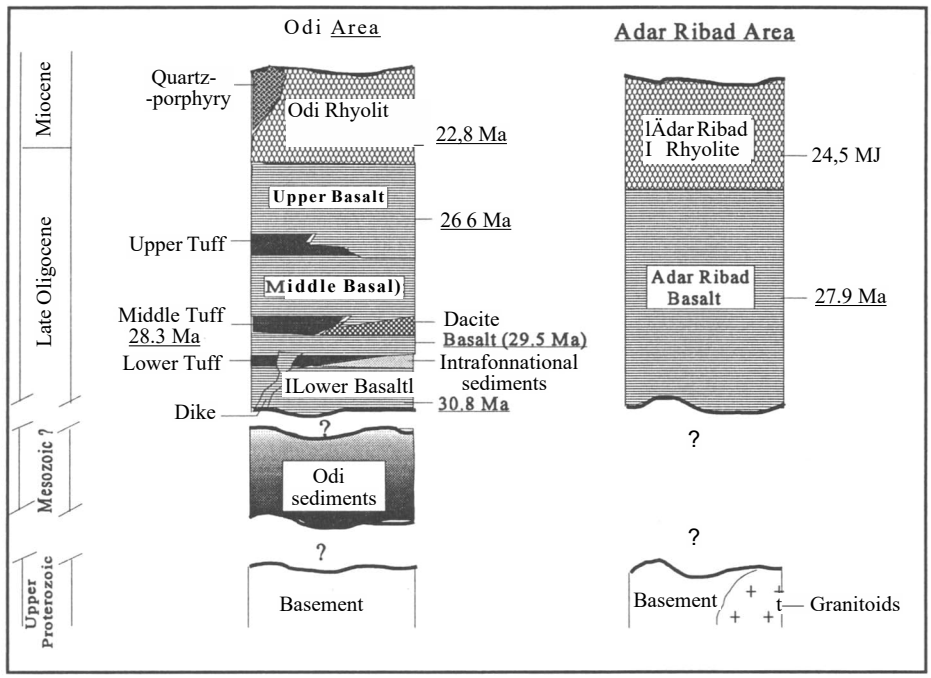

Figure 2.3. Summarised stratigraphic relationships between the Phanerozoic rocks of the Derudeb area based on K-Ar age determinations and field observations. Bold undulöse lines indicate possible erosional surfaces.

A K-Ar absolute age dating conducted for one sample from each basalt and rhyolite in this area gave whole rock ages of *ca.* 27.9 and 24.5 Ma, respectively (Table 2.2). The latter was also dated by the more reliable Ar-Ar evaporation and yielded an average age of *ca.* 28.5 Ma. With the exception of this limited discrepancy, the results by and large conform with the relative stratigraphy, and indicate that the volcanic activities in the Odi and Adar Ribad areas were coeval. Furthermore, it may also be inferred that the basic and acidic volcanisms in the Odi and Adar Ribad areas belong to the same regional magmatic events that also prevailed in this part of NE Africa and SW Arabia.

The Khor Windi volcanics

The third exposure of volcanic rocks around Khor Windi is represented only by basalts. The basalt shows a composition and a texture similar to the Adar Ribad occurrence, and here also no sedimentary rocks have been observed. The basalts occur as NE-SW trending densely emplaced dikes whose aggregate maximum thickness reaches few hundreds of metres. They are partly discontinuous and the length of a single body may extend for about half a kilometre. These basalts are thought to represent a zone of weakness, related to extensional tectonics, possibly connecting the two major occurrences of volcanic rocks in a form of transfer/transcurrent fault that exploited a Pan-African weak zone (see Section 2.2.4). Although no absolute age determination has been conducted for this occurrence it is presumed to be of comparable age with the other two major exposures discussed above. No remarkable extension is presumed to be represented by the Khor Windi occurrence.

Dikes

In addition to the above mentioned rock types there are several dikes believed to be related to the

Cenozoic volcanism in the area. As can be seen from the Landsat imagery they occur typically concentrated along the southern part of the Odi basin and in close association with the Adar Ribad volcanics often in the form of swarms. In the former occurrence the dikes frequently show steep dip, predominantly trend submeridional, with a less pronounced set striking NE-SW, and have a width of about 3-8 m. Jointing is often well displayed. Both basic (doleritic) and acidic (rhyolitic) varieties occur. While the latter are less common and seem to be restricted to the western margin of the central Odi-area, the former are overwhelmingly abundant and widespread.

A basic dike from the Odi area has been dated at *ca.* 29.5 Ma (Table 2.2) using K-Ar whole rock method. This result is comparable with an age of 30.8 Ma obtained for the lower basaltic sequence of the same area, since dikes commonly have excess Ar from degassing of basement rocks. This observation, added to the abundance of the basaltic dikes, close spatial association and compositional similarities between the basic dikes and the basalts, allows the conclusion that the latter were extruded as fissural eruptions with the former as feeder-ways through fractures that were developed during extensional tectonics (Section 2.2.4). In the Adar Ribad area the dikes exclusively trend N-S and both acidic and basic varieties occur. Here, they form a swarm of several kilometres wide and extend for tens of kilometres along strike cross-cutting the basement structures.

The age relationship between the basic and acidic dikes appears to be less explicit; however, the basic dikes are probably older than the acidic dikes considering the stratigraphic relationship between their extrusive equivalents. The time relationship between the NE-SW and N-S sets of dikes seems also less obvious. Nonetheless, the NE-SW striking dikes are presumably older than the N-S trending ones, in view of the tectonic development of the corresponding lineament sets (Section 2.2.4).

Quaternary sediments

The Quaternary sediments in the study area mainly include wadi deposits, unconsolidated sand and gravels. Post-volcanic sedimentation of some conglomerates and arenites have been reported to occur just N of the Odi depression overlying the rhyolite of J. Oman (Hassan, 1991). These conglomerates contain rounded pebbles from the underlying pyroclastic rocks whose relation to the volcanic rocks is an angular unconformity (Hassan, 1991). Such conglomerates have not been observed either in the field or on the processed images during this work.

Recent sediments are ubiquitous along the major drainage channels in the area. They range in thickness from few metres up to several tens of metres, with good examples occurring along Khor Langeb. In most sections variation in grain size is not uncommon. Change in the course of flow has been noted along the same river just N of J. Oman whereby Recent sediments of up to 120 m thick occur about 300 m away from the present channel. These are indicatives of possible neotectonic activities in the region that are to be associated with the Red Sea rifting.

Another area of relevance is the Odi depression where Recent sediments occur extensively. This area is a recent depocentre for the drainage systems S and SW of the area and draining northwards. Its relatively broader depositional area has been considerably reduced at least in the past decades, as seen on images obtained in 1979 (see Section 2.2.4), due to environmental changes.

2.2.4 Structures

The structural history of the Derudeb area is admittedly more complex to be completed by this work, with a limited ground-truth data, and requires more detailed investigations. Some regional aspects have been given by Abdelsalam and Stem (1993), and detailed references to the adjacent areas have been made by Wipfler (1994) and Haenisch *et al.* (1996). In the following section a brief account to the Derudeb area is given based on field observations and interpretations of Landsat images (1 : 170 000) in addition to hard copy outputs from Large Format Camera (frame 1321, 1 : 75000, c=306mm, H=230 km). The structural developments in the area may be broadly grouped

into two: structures related to the basement rocks (principally Pan-African) and those which were active since then (mainly Cenozoic).

Basement structures

At least four major ductile deformation episodes have been identified within the basement rocks of the Derudeb area. The first phase (DJ is interpreted to be related to the high-grade rocks and is characterised by complex fold structures. This interpretation is rather indirect since limited structural elements belonging to this event were observed in the field. Possible exceptions include intrafolial folds seen within the metasediments in the SE whose primary layers have been tightly folded. As it has been seen in the field the gneissosity often parallels the primary layerings and it variably strikes between NE-SW and NW-SE.

On the Landsat images it has been seen that both in the SE (N of J. Qawayateb) and SW (S of J. Adni) fold patterns of complex nature are displayed by the quartzite-amphibolite bands and graphitic gneiss/schist, respectively (Figure 4.1). These often tight- to close-folds, and certainly modified by the later D_2/D_3 overprints, appear to have axial plane strikes varying from E-W to N-S. These complex folded structures seem to be lacking in the northern part of the area where the greenschist-dominated metavolcano-sedimentary sequences are exposed. Planar structures that belong to the Dj event are the gneissic foliations that presently display variable orientations due to later folding phases.

In the Derudeb area the second (D_2) and the third (D_3) deformational events are rather well displayed by the metavolcano-sedimentary sequences at variable scales. The D_2 deformation is possibly the earliest event witnessed by these rocks. This episode produced the penetrative S_2 foliations that mostly strike NNE, as it has been observed over folded primary layers in a couple of localities. This was consecutively followed by the D_3 deformation that refolded the D_2 structural elements in a similar pattern. Folds of D_2/D_3 events are tight to isoclinal, with axial planes striking ENE-WSW and frequently dipping N or S. The fold axes often plunge at shallow to moderate angles towards SW or NE and were possibly generated through NW-SE oriented principal stress that produced co-axial but not co-planar foldings.

Orientations of structural elements produced by the D_2/D_3 events suggest crustal shortening in the NNW-SSE direction that occurred at deeper crustal levels under ductile conditions. A good example of the D_2/D_3 structural relationships is the fold closures seen on the Landsat image in the central part of the area (Figure 2.4, inset-2 of Figure 4.1). On this image it is evident that the interference between these deformation events gave rise to a hook-shaped pattern (Ramsay, 1967), and the distinction between D_2 and D_3 structural elements is apparently possible. This relationship has also been observed at outcrop scale in a number of localities.

Another prominent feature belonging to these events is the NE-SW trending thrust fault in the central part of the area (Enclosure). This thrust zone is interpreted to represent the late phase collisional tectonics, that was developed through progressive deformation of D_2/D_3, between the crustal segments on either sides (Section 2.3). It is thought to have been developed as an accommodation to the progressively intense compression that led to crustal shortening, through displacements involving vertical components. The sense of movement along this thrust fault has been deduced from some stretching lineations measured in the field, and fold vergences which consistently indicate a northward plunge. Interpretation of these structural elements indicates a generally NNW-SSE tectonic transport with northwesterly underthrusting. The thrust fault was modified by the later D_4 shearing (Enclosure).

The fourth deformation episode (D_4) that affected the basement rocks of the Derudeb area is related to the development of transpressional ductile shear zones. One of such prominent features is the Adadi Thrust and Transpressional Shear Zone (ATTSZ), named after the main ridge in the area, that occurs in the central-southern part of the map sheet. This high-strain zone strikes about N45°E and can be continuously traced for over 45 km along strike, after which it becomes less pronounced and trends about N10°E for another 10 km. In its central part it has a width well over 6 km whereas to the NE it becomes as narrow as 1.5 km. The ATTSZ can be

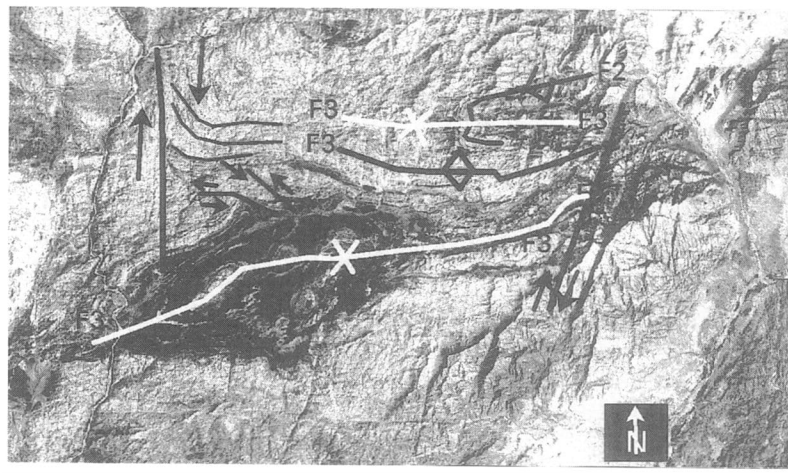

Figure 2.4. Interference relationships between D_2 (F_2) and D_3 (F_3) folds and later conjugate sets of dextral and sinistral shearing (D_4) as seen from Landsat TM imagery. Block size 48.4 x 27.8 km^2. Inset-2 of Figure 4.1.

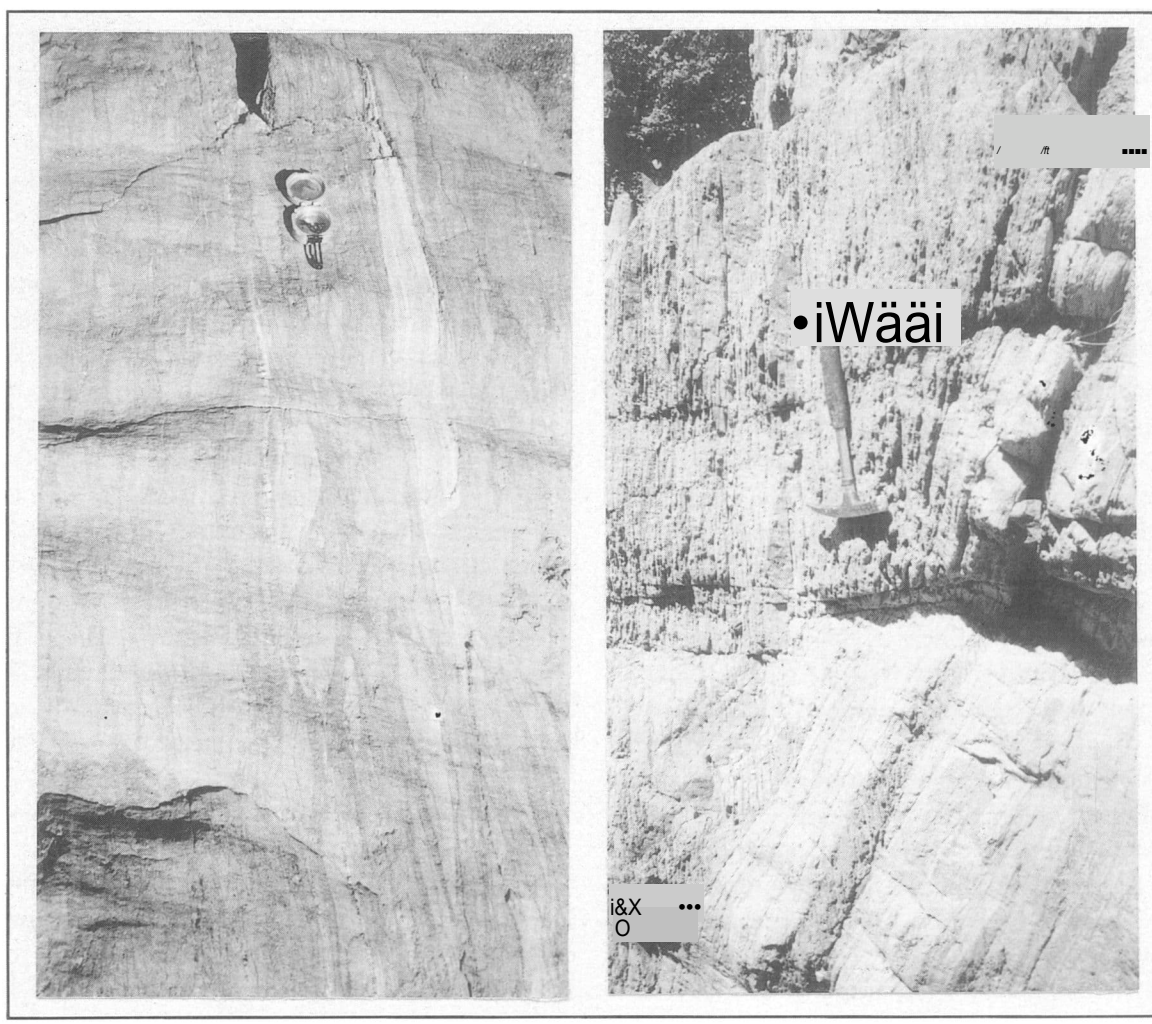

Figure 2.5. Highly stretched and displaced boudinages (left) and well developed penetrative shear bands (right) observed within the metavolcanics along the ATTSZ (parallel to the handle of the hammer and compass length).

followed further to the SW where it becomes as wide as 10 km and shows modifications by the late-orogenic plutons. In this area its central zone is typified by dismembered ultramafics (mainly severely fractured talc schists), as also seen on the processed Landsat imagery (Figure 4.1). Shear sense indicators such as S-C fabrics, typical shear bands, asymmetrically boudinaged and fractured leucocratic "inclusions" with pressure-shadows set in a rather dark country rock, and vertical asymmetric-folds indicate the involved significant lateral movements. Thin-section study of few samples from this zone also revealed an ultramylonitic texture. Figure 2.5 shows some features observed along this structure.

According to field data both dextral and sinistral movements appear to have prevailed in the ATTSZ, the former being less frequent than the latter. The left-hand displacement has also been confirmed from small scale Landsat imageries. Striation lineations and grooves observed on the S_2/S_3 surfaces at few localities show a subvertical northeasterly plunge, implying the involved compression. Furthermore, an asymmetric "Z" fold observed in one locality plunges 60° towards N70°E. This is interpreted to indicate that the dextral shearing did involve some vertical component, implying a transpressional character of this shear zone, at least at its early stage. The rather sinistral and regionally expressed shearing appears to be a younger event that took place due to the change in the stress field. In this case the shallow plunging stretching lineations are interpreted to show a principally strike-slip tectonic transport. The narrow "Arqawi Shear Zone" in the N (Figure 4.1), having a similar NE-SW strike with left-lateral movement, is thought to be geodynamically related to this structure.

The next prominent high-strain zone of "Tihilla Shear Zone", occurs SE of Tihilla ridge (Figure 4.1) and is defined by highly crushed quartzofeldspathic bands and quartz mylonite. The shear zone trends SE-NW with a mylonitic foliation measured at a place having a dip of 75° towards N50°E. It has been difficult to determine the sense of movement within this zone, although Wipfler (1994) identified the Himasa Shear Zone, further to the NW (out of the map area), as a left-laterally displaced zone. The Tihilla Shear Zone is thought to have possibly contributed to the emplacement of the nearby Tihilla ring complex.

A less prominent but similarly trending shear zone seen in the NW within the acidic metavolcanics (E of Abu Samar, Figure 4.1), however, shows a sinistral sense of movement. All the shear zones with NW-SE trend are to be geodynamically related to the prominent Oko Shear Zone further N in the Nakasib area (Abdelsalam, 1993) which has the same sense of movement and runs parallel to them (Figure 2.1). The Oko Shear Zone is known to be post-dating the Amur-Nakasib Suture (Abdelsalam, 1993).

In the southern part of the area a narrow high-strain "Kibirit Shear Zone" represented by sheared biotite schist, on which well pronounced stretching lineations marked principally by biotite crystals occur, were observed. The lineations plunge subhorizontally either to the NE or SW. On the Landsat imageries the shear zone shows a sinistral sense of movement and appears to be extending for over 20 km (Figure 4.1). This structure has been displaced by a dextral E-W trending semi-ductile shear, and later on reactivated as brittle fault affecting the Odi basalts. This observation, in addition to its alignment with the Khor Windy volcanics, may indicate the significance of this shear zone in connecting the two volcanic occurrences (see below).

The fifth deformation episode (D_5) generally produced brittle structures in the Derudeb area. One such structure of regional significance is the Adit-Langeb Lineament, which shows a less pronounced left-handed displacement over the gabbroic pluton in the far N (Figure 4.1). On mosaicked Landsat images this structure can be followed northwards up to the Red Sea coast with a total strike-length reaching well over 300 km (eg. Haenisch *et al.*, 1996). From these images it is also evident that several Pan-African syn-orogenic granitoids occur along this fault, suggesting that the lineament is presumably a deep-seated structure that served as a weak zone for their emplacements. Most of the latitudinally striking Neoproterozoic dikes in the NW are apparently truncated by this structure. This lineament also marks the western boundary of the Odi volcanics, suggesting its later reactivation

during the Cenozoic. Other brittle structures related to the basement rocks in the area are represented by the various lineament orientations: NNE-SSW, E-W, and NW-SE sets considered in the coming Sections.

Cenozoic structures

These sets of structures are ascribed to brittle deformation that are believed to be principally related to the tectono-magmatic events associated with the sedimentary and volcanic rocks of the Derudeb area. They are thought to be primarily related to the nearby Red Sea rifting/opening, and include different types of faults, fractures, uplifts, extension, etc. Figure 2.6 shows a possible tectono-magmatic model proposed for the Odi and Adar Ribad areas for the time between Late Oligocene and Early Miocene.

As it could be seen on the mosaicked Landsat images the prominent Adit-Langeb Pan-African lineament (Section 2.3) makes the western boundary of the Odi sediments and the Cenozoic volcanics. To the E these rocks are bounded by another lineament that runs close to Khor Langeb. Supported by the centrally dipping attitude of the primary layers and striation lineations observed in a couple of places along these surfaces, it is interpreted that these lineaments are essentially normal faults that define a graben structure (see Figure 2.6). This structure is thought to be the main basin in which the Odi sediments were deposited. The axial trace of this rift basin extends southwards out of the map area with its length reaching well over 100 km, and it has a maximum width of about 28 km in the central Odi area. Volcanic rocks could be traced all along this structure, but its southern peripheiy is covered by Quaternary sediments. The Odi rift basin, therefore, most likely represents one of the earliest extensional tectonics that preceded the Red Sea rifting, although it appears presently difficult to constrain its upper age limits (Section 2.3).

In addition to the above event of graben formation, two later major phases of extension are to be recognised in the Odi area: an early phase related to the basaltic extrusion that are genetically related to the submeridional basic dikes, and a later event associated with the emplacement of the acidic rocks (Figure 2.6). It is worth noting that no direct observations have been made which prove that extension was not continuous during the magmatism that ranged between *ca.* 31-22 Ma in the Derudeb area. However, supported by the distinctly recognised extension phases for the Red Sea (Voggenreiter *et al.,* 1988) it is assumed that similar events most likely prevailed in the study area.

The earlier phase has been recognised based on the interpretation that the abundant basic dikes parallel to the axial trace of the rift basin indicate fissural eruption of the basaltic flows. Since these dikes represent new material injected into the upper crust, their age and aggregate thickness may give a clue as to the time and amount of extension that was needed to keep the isostatic equilibrium, respectively, though extension by dyking is generally insignificant for the very limited volume involved.

An age of 29.5 Ma obtained for a basaltic dike in the Odi area, is believed to be correlative to the Lower Basaltic unit (Figure 2.3) that also gave an age of about 30.8 Ma. The above mentioned extension is thus interpreted to have started about 31 Ma ago being accompanied by the volcanism that certainly lacked an acidic component. This interpretation conforms well with the one suggested for the rifting in the southern Red Sea based on the study of the Jizan Group (As Sirat), SW Saudi Arabia (Voggenreiter *et al.,* 1988), although the volcanism there was bimodal. In the absence of substantial subsurface information extension estimates are obviously difficult, especially where fault planes are not well exposed.

The last major extension event is related to the emplacements of acidic volcanics and it appears to have been prominent around the Odi depression. On Landsat MSS image captured on the 2nd August 1979, a lake of about 10 km^2 could be seen covering this area. As stated earlier, the rocks dip at about 25° towards the centre of the depression. The structure is also well depicted on residual gravity anomaly data (Section 6.5). Similar pattern, where the surrounding rocks show inward dips, has been seen in SW Ethiopia (C. Ebinger, pers. comm.). This feature is thought to have been developed

because of thermal subsidence related to post-rift cooling rather than anything structural. Its proximity to the Tashalal-Langeb transfer fault along which the younger acidic rocks are confined, and the displaced nature of the rocks on its sides (see below) also augments the idea that this zone behaved as a centre of extension. The extension direction was thus more of NE-SW parallel to this transcurrent fault. The above observations suggest that the latest major rifting took place about 22 Ma ago (Figure 2.3, 2.6) when the acidic volcanics and intrusives were emplaced. This age conforms well with the period of rapid extension and per-alkaline volcanism indicated by Almond (1986) for the Red Sea opening, and the major rifting event in the central Red Sea (Voggenreiter *et al.,* 1988).

Using processed Landsat imagery, displacement measurement along this fault gave a roughestimate of about 7 km, assuming no dip-slip component and supported by field observations. This figure is valid as the upper limit of extension, and to the N and S of this fault extension estimates are certainly much lower. Using large scale images, information over the least extension estimate shows few hundreds of metres, using dikes along an E-W section across the Odi rift. For the subhorizontal strata! dips a maximum of 2 km extension is estimated anywhere in the Odi basin.

Another set of lineaments in the Odi area shows a NE-SW trend with a left-lateral displacement. These lineaments are properly displayed over the rhyolite and basalt units, where they are partly filled by thin dikes, and are believed to be younger than the N-S trending ones. One major lineament with a similar trend traverses across the central-Odi volcanics and along the Tashalal-Langeb extension. This structure connects 2-3 initially separated normal faults, and appears to delineate the northern subhorizontally lying volcanics over a relatively narrow block *(ca.* 10 km wide) from the centrally dipping wider block *(ca.* 15-18 km) that possibly underwent more extension. It should also be noted that the younger and saturated volcanic rocks (dacite, rhyolite, tuff and quartz porphyry) are closely associated with this lineament possibly depicting a volcanic migration, and the accompanying chemical differentiation, towards the centre of the rift basin. Based on these facts it is suggested that this structure represents an active zone that behaved as a transfer fault during the rifting. Its eastwards continuation into the structures of ATTSZ, as seen from the processed Landsat imageries, is a manifestation of the truth that this lineament exploited a similarly trending and identically displaced Pan-African weak zone. Similar observations have been made in different parts of the Red Sea (eg. Makris and Rihm, 1991; Schandelmeier and Pudlo, 1990).

The RSH as a whole represents a block that has been uplifted (Almond, 1986) by events related to the Red Sea rifting, and it exhibits a westerly gentle slope (eg. Abdel Rahman, 1993). As stated earlier, the Adar Ribad block in the NE, with thick Cenozoic volcanics on its western part, represents one of the most elevated ridges in the area and it is interpreted to be an uplifted block during this event (Figure 2.6). The volcanic rocks are presently exposed at elevations between 300 and 1300 m a.m.s.l. The lack of these rocks on its eastern part, but the occurrence of basalts just E of the Baraka Suture in a subdued elevation as seen on the work of GRAS (1988), suggest that this block acted as a hanging-wall and the basaltic flows through the reactivated Baraka fault were extruded on the foot-wall towards the E (see Figure 2.6). Alternatively, volcanic rocks have been removed from the hanging wall by erosion, though it seems less likely.

The volcanic layers on the western part of the Adar Ribad block show a consistent westerly dip of about 45°, and are thought to indicate a westward tectonic tilting (Figure 2.6). The block-tilting appears to have been bounded to the W by the prominent Osir Walab Fault (OWF) that trends NNE, and extends for several kilometres northwards out of the study area, being obscured by Quaternary sediments (Figure 4.1, Enclosure). The large stratal dip is, therefore, ascribed to the combination of tectonic tilting and late rift-flank uplift associated with the Red Sea. Although fault dips have not been measured in this area they are presumably higher than the stratal dips. This may further hint larger extension in this part of the study area as compared to the Odi area.

In the same area, several closely spaced dikes with a submeridional trend make a remarkable feature on the Landsat images and are interpreted to

be feeders to their volcanic equivalents. These, often basic, dikes appear to be parallel to the left-lateral brittle faults seen on these images and those which possibly accompanied the uplifting. The Adar Ribad block also seams to have truncated the northeastern extension of the ATTSZ, as seen on these imageries, and comparison of lithologic units along its western part appear to crudely imply left-lateral displacement. These observations may encourage the interpretation that the uplifting event had some northwards lateral movement, in a form of decoupled blocks, though more field data is still needed.

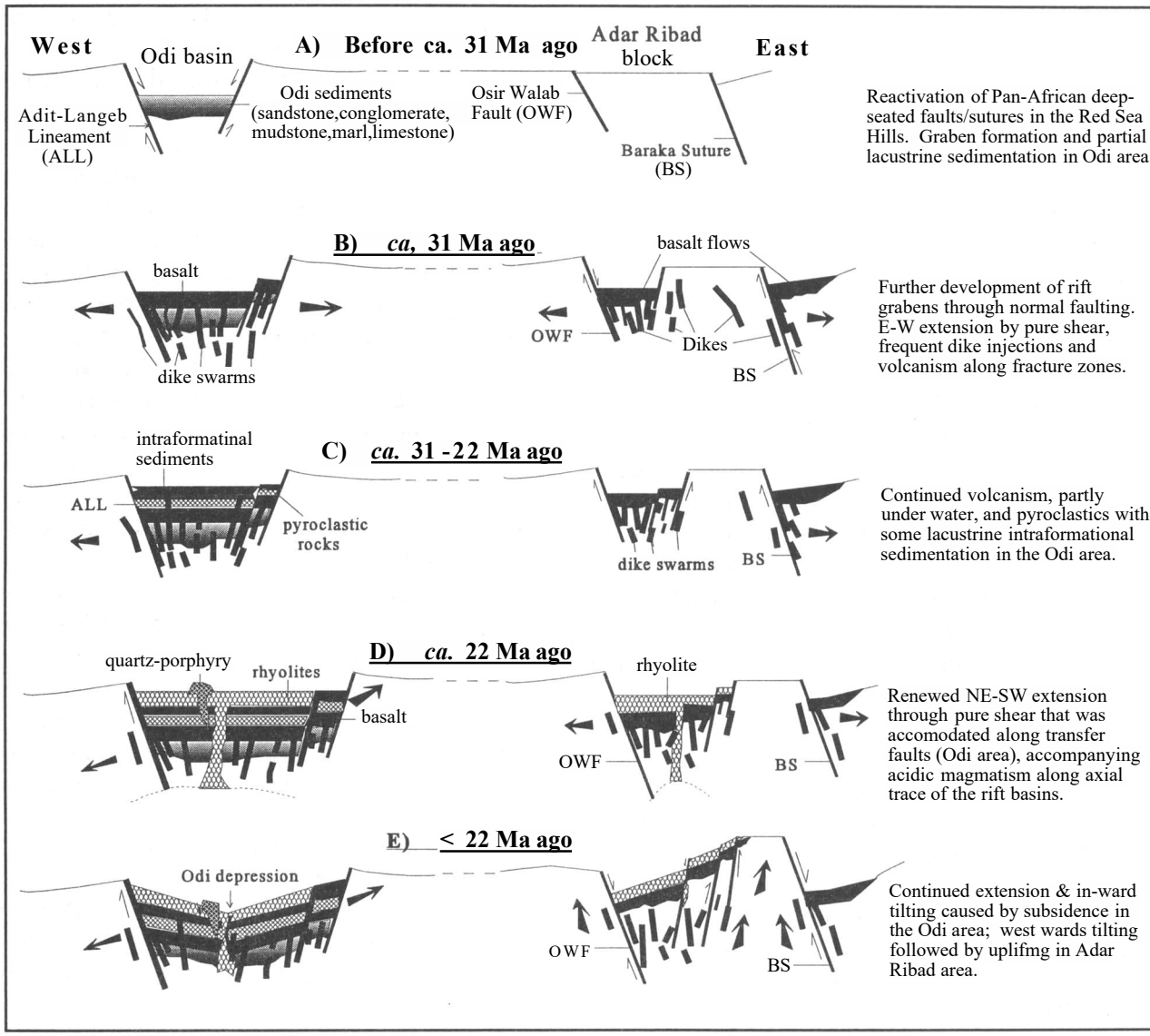

Figure 2.6. A schematic diagram showing the tectono-magmatic events during the Late Oligocene-Early Miocene that led to continental rift-basin developments in the Derudeb area. Stratal dips simplified to illustrate basinal stratigraphy. In A-D, dips approach 20° in the Odi area, and stratal dips are now about 40° in the Adar Ribad area indicating post-depositional tilting probably in the past 20 Ma. Geochronological data represent K-Ar ages (see text). White areas in the sections symbolise basement rocks, and arrows indicate presumed movement directions.

Lineament analysis

For the purpose of lineament analysis Landsat TM data was initially processed using directional filters chosen after a broad observation of the structural pattern of the area. A colour composite image has then been produced at the scale of 1 : 170 000 using these three images, from where lineaments well over 3 km long were manually traced. The resolution of the minimum width is dependent on the spectral contrast with the adjacent units but few metres can generally be picked up on the images. In this approach a total of about 1107 lineaments were recognised and analysed. Section 4.6.1 elaborates the image processing technique adopted.

In order to simplify interpretation, the obtained lineament map has been divided into six different domains for statistical analysis, depending on distribution and tectonic characteristics (Figure 2.7a). Domains I and II seem comparable but separated to observe if the Adit-Langeb lineament, as a "master fault", had influenced the structural distribution in both areas. Domains III and VI are separated from the other sectors to be able to possibly "discriminate" Pan-African and younger Cenozoic structures. Domain IV covers the ATTSZ while domain V is ascribed to the gneissic rocks. Figure 2.7 shows all the lineaments along with the domain boundaries and the corresponding rose-diagrams plotted for direction against total length of the lineaments in each 10° sector expressed in percentage.

In domain-I, a predominant N-S and a secondary trend of E-W are apparent, in addition to which subsidiary ones striking at 060° and 130° exist. In area-II the prominent trend is centred around 020° in addition to which secondary and ternary strikes occur around 080° and 045°, respectively. Areas III and VI also exhibit a significant meridional trend centred at about 010° followed by minor distinct orientations around 045° and 090°, respectively. In a similar way the major orientation in domain-IV falls around 060° whereas in area-V it is centred about 020°; the secondary orientations are centred around 010° and 090°, respectively, in addition to a 020° ternary strike in the latter.

Some of the N-S trending faults in domain-I shows sinistral sense of movement, including a major fault just E of the master Adit-Langeb fault (see Figure 4.1). It is also known from image interpretation that significant amount of dikes display the same trend in this domain. A principal compressive stress oriented at about 335° would generate the NNE-SSW trending major sinistral lineaments including the Adit-Langeb fault and the other 130° trending less pronounced dextral faults. These are thought to be conjugate sets associated with the D_2/D_3 events.

Compression events which led to thrust tectonics towards the late phase of D_3 possibly gave way to a right-handed E-W (090°) shearing/ displacement and was more likely intensified during D_4. These events also gave rise to lineaments striking NE-SW (around 050°), and which possibly represent compression associated thrust faults and/or tensional fractures parallelling fold hinges in domains I and II. The relatively pronounced E-W trending lineaments in section I, that are apparently truncated by the prominent Adit-Langeb lineament, are more possibly attributed to dike swarms that were initiated through a sublongitudinal crustal dilation (post D_3) and that consequentially promoted the emplacement of post-orogenic Tihilla ring complex to the W. E-W trending aeromagnetic anomaly are also thought to be related to these dikes (Section 6.5).

The orientations of lineaments in area V is also similar to domains I and II. Pan-African dikes trending NW-SE and E-W are known to occur in this area. This could be related to major extensional tectonics in ENE-WSW direction, and may be ascribed to the same D_2/D_3 events, in the absence of orientations of structural elements belonging to the Ü! phase.

The relatively broad and prominent orientation of domain-IV centred around 060° and a minor trend of 010° obviously denote the ATTSZ that has been developed through a subhorizontal principal compressive stress (D_4) oriented NNE-SSW (around 035°). The second set of 010° strike in domain IV and the dextrally displaced lineaments trending about 020° in domain II are thought to be concomitant with this shearing event; the latter frequently occur close to this structure and are less developed in domain-I.

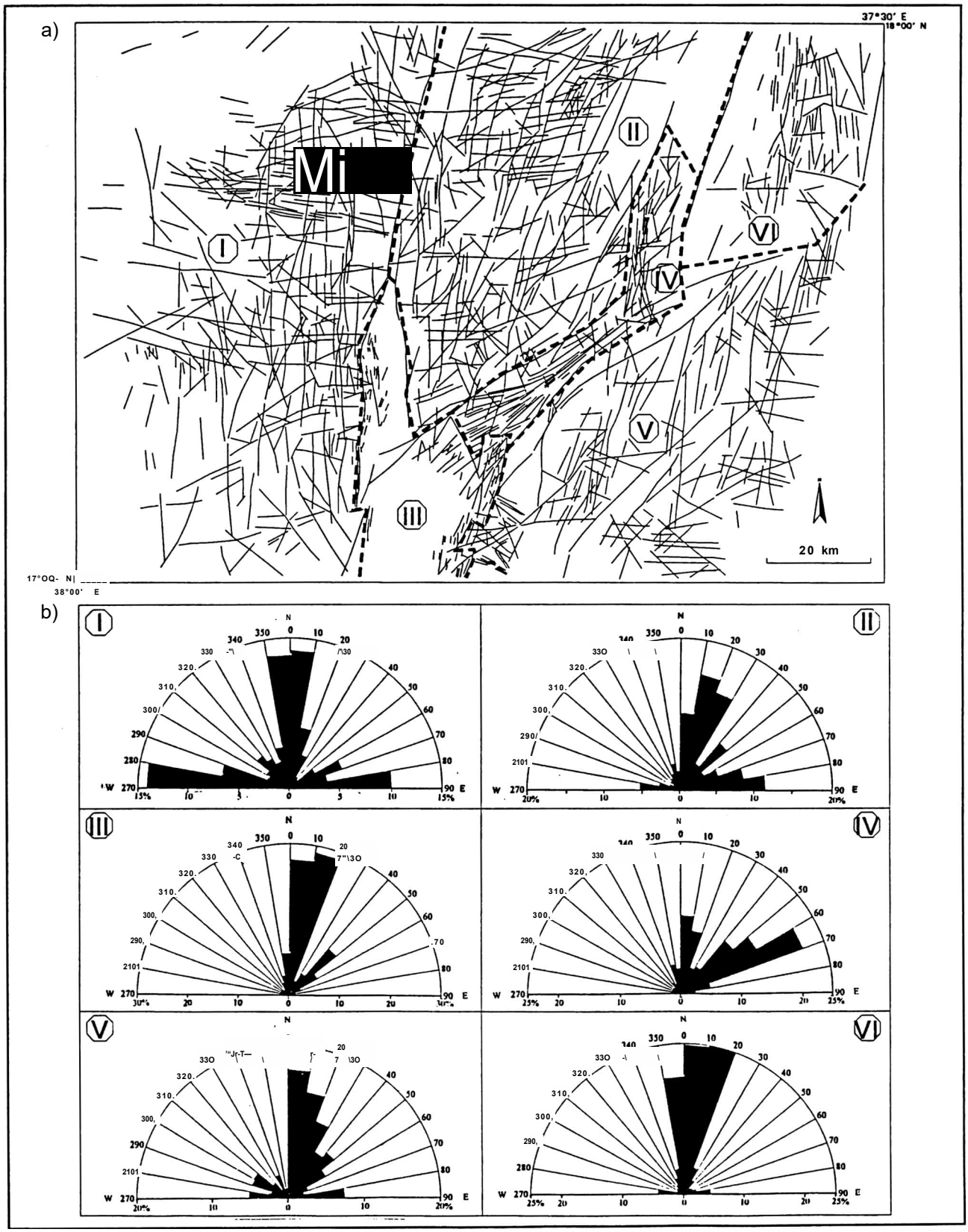

Figure 2.7. Lineament map of the Derudeb area, with different domains (I-VI) demarcated by brocken lines (a), and the corresponding rose-diagrams for total length (in percent) versus direction in sectors of 10° (b).

In domains in and VI the N-S lineaments are known to represent significant proportion of dikes and normal faults having submeridional orientation. A maximum extensional stress centred around 090°would generate longitudinal extensional fractures which then gave way to fissural eruptions in these domains. The secondary lineaments striking 040° in domain III are attributed to left-handed transtensional fractures interpreted to be a transfer faults. It should be noted that the N-S lineaments in both domains and the E-W ones in domain-VI are not only subparallel but also extend further into those in the other domains, suggesting a substantial reactivation of Pan-African fracture systems during the Cenozoic. The younger N-S oriented lineaments and drainage patterns indicate Neotectonic events of extension and uplifting that are related to the Red Sea trend.

2.2.5 Relationships between magmatic and tectono-thermal events

Based on thin-section study, field observations and interpretation of processed imageries the following relationships has been established between the deformation, metamorphism and plutonic emplacements for the basement rocks of the Derudeb area. The earliest deformation (DJ, recognised only in the gneissic rocks, is thought to have been accompanied by a metamorphic phase of mid-amphibolite facies (MJ. This prograde phase is represented as gneissosity within these rocks, and it is often marked by elongated amphibole (hornblende) crystals in most of the metapelites. No plutonic emplacement related to this activity has been identified by this work. It is broadly assumed that this tectono-magmatic event is related to an early passive margin environment that was developed some 1000 Ma ago as indicated for parts of the Nubian Shield (Vail, 1988).

The next prograde regional metamorphic episodes (M_2/M_3) are mainly related to the metavolcano-sedimentary sequences which generally witnessed greenschist facies conditions. In most of the metasediments, micas make the largest component defining the S_2/S_3 foliations. Very close to the ATTSZ the M_2/M_3 phases reached lower- to mid-amphibolite facies conditions, as represented by the development of hornblende as the major constituent in intermediate rocks.

In the high-grade gneissic rocks post-hornblende recrystallisation of biotite at high-angle marks these events. It has been difficult to distinguish between the M_2/M_3 phases during this work, and both are thought to be associated with D_2/D_3 progressive deformations which locally gave way to the thrust tectonics that in turn partly gave rise to lower amphibolite facies metamorphism. The syn-orogenic plutons in the area are possibly ascribed to the arc/ back arc magmatism of 900-850 Ma old suggested for the Haya Terrane (eg. Abdelsalam and Stem, 1993).

The syn- to late-orogenic granitoids of the Derudeb area are supposed to have accompanied the $M2/M_3$ thermal events. In regional context they may be related with syn-collisional mantle-origin plutons of 815-724 Ma old proposed by Klemenic and Poole (1988). If the distinction between these thermal phases is well substantiated, this interpretation may indicate subduction similarities between both events.

Since the post-orogenic plutons in the Derudeb area cut across the major shear zones, as could be seen on the processed images, they certainly post-date the D_4 shearing events. Their emplacement in a subduction related environment (El Labib, 1991), dominantly N of ATTSZ, possibly resulted in crustal thickening. Widespread contact metamorphism (M_4) along the boundaries of these plutons marks this phase. Good examples occur in the NE around J. Arqawi (Figure 4.1). Lack of any preferred orientation in these plutons suggests a relatively stress-free environment, as also revealed by their circular features. These rocks may possibly correspond to within-plate magmatism in the RSH 550-720 Ma ago (Shackleton, 1994).

The last metamorphic phase (M5) is a retrograde event represented by epidote and chlorite after amphibole and/or biotite. This event is relatively widespread in the region and it possibly occurred following the crustal relaxation which gave rise to post-orogenic granitoid emplacements in the area.

The structural and magmatic relationships of the Phanerozoic rocks in the Derudeb area have been considered in section 2.2.4 and a simplified developments of events and their timings are given in Figure 2.6. It is to be noted that in the study area no evidence of uplifting before magmatism has been observed, and the early magmatic events were certainly preceded by, or synchronous with, extension. But for the later acidic volcanics it is most likely that magmatism predated extension, similar to what has been observed in Yemen (Menzies *et al.,* 1992), and were finally followed by uplifting.

2.3 Regional Implications

The Haya Terrane of the RSH is known to make part of the juvenile Nubian segment of the Pan-African sequence that is bounded by Nakasib Suture in the N and the Baraka Suture in the S (Kroner *et al.,* 1987). Abdel Rahman (1993) interpreted the Abu Samar area to represent an ophiolite sequence within the Haya Terrane, and this idea has also been promoted by Wipfler (1994). Drury and Berhe (1993) suggested that the area W of the Baraka Suture (Baraka Terrane) is quite distinct from the younger metavolcano-sedimentary rocks that comprise tectonically juvenile terranes to the E. Involvement of older crustal elements *(ca.* 840-870 Ma) in the area E of the Baraka Suture has been indicated by Kroner *et al.* (1991). If these interpretations are valid, the western limit of the Baraka Terrane and the eastern boundary of the sector S of the Abu Samar Ophiolite need to be constrained.

As it has been discussed above, structural pattern of the first deformation (D,) displayed by the high-grade rocks does not appear conformable with those displayed by the greenschist assemblages. The relatively mature morphology (with low-relief outcrops) of the former against the rather rugged and tectonically juvenile nature of the latter in conjunction with their distinct spectral expressions (of high albedo caused by silica-rich minerals within the gneisses) to be attributed to mineralogical variations also corroborate this difference. Furthermore, the occurrence of NW-SE and E-W trending dikes (see also Drury and Berhe, 1993) exclusively associated with the gneisses, coupled with the association of high-grade rocks lacking ultramafics both on the images and in the field, conform with this disparity.

The ATTSZ, as a ductile shear zone subparallel to the regional strike, represents a prominent sinistrally displaced structural pattern unique to its surroundings, but identically displaced like the Nakasib-Bir Umq and its western extension Oshib-Amur sutures (eg. Abdelsalam, 1993) of the central RSH. Although less pronounced, older dextral shearing comparable to those in the Nakasib Suture (Abdelsalam and Stem, 1993) and which occur within the large "S" structure are also evident in the ATTSZ (Section 2.2.4). Few stretching lineations measured along this zone have been interpreted to suggest early compressional tectonics that were later predominated by transpressional events. Rocks along the ATTSZ, at least partly, show amphibolite facies metamorphic conditions possibly attributed to the intense shearing and their spectral signatures appear similar to that of the high-grade rocks. In its western extension, intensely sheared and dismembered ultramafics (talc schists, pyroxenite and minor serpentinite) occur as small elongated ridges in association with marble, minor basic metavolcanics (amphibolites) and some gabbroic rocks interpreted to exhibit a layered structure (Section 2.2.2). Presently unmapped serpentinite bodies were observed in its central part and minor pyroxenites have as well been noted in the northeastern extension of the same shear zone (Section 2.2.2). These rocks may be ascribed to arc or lower crust assemblage of oceanic origin, but requires more work.

It can been seen on the geological map (Enclosure) that the distribution of syn- to late-orogenic plutons is largely confined to the area N of the ATTSZ and it defines an arc running parallel to this zone. El Labib (1991) interpreted the tectonic settings of some of these granitoids to be related to volcanic arc magmatism that also indicate a syn-collisional environment. He ascribed the geochemical characters of post-orogenic granitoids in the area exclusively to within-plate magmatism possibly associated with subduction zones, ensialic

rifting or rift-related alkaline to subalkaline magmatism.

Further to the E, about 30 km out of the map area (S of Tokar), Kroner *et al.* (1991) reported the involvement of older crustal component (840-870 Ma) within metavolcanics whose geochemical characteristics has been ascribed to extensional tectonics. They further suggested that these rocks have been evolved near the ancient continental margin of Africa. According to Drury and Berhe (1993) these rocks fall within their relatively juvenile and younger terranes. Little data is available over the Baraka Lineament at the eastern boundary of the map area (Enclosure), but it has been recognised as a Pan-African strike-slip fault representing a crustal boundary or suture (eg. Vail, 1985; Kroner *et al.,* 1987) separating the older Baraka Terrane in the W (corresponding to the high-grade rocks, this work) from rather juvenile metavolcanic terranes to the E (Drury and Berhe, 1993). These are in conformity with Embleton *et al.* (1983) who implied that the high and low grade rocks constitute distinct crustal entities.

Based on the above observations and the regional set-up in this part of the RSH, it is proposed that the ATTSZ possibly represents a tectonic boundary demarcating an interface between discrete crustal components; an older terrane in the S that is the western continuation of the Baraka Terrane suggested by Drury and Berhe (1993), and a relatively younger and juvenile segment to the N that makes part of the Haya Terrane of Kroner *et al.* **(1987).** The ATTSZ shows significant similarity with the Nakasib Suture to the N in both strike and deformation styles (where NNW-SSE oriented co-axial folding and thrusting as well prevailed; Abdelsalam, 1993), and also with other similarly trending sutures in the region (Stem *et al.,* 1990). Its dominantly strike-slip nature shows a later event may be interpreted either as the less developed equivalent of the Oko Shear Zone (Figure 2.1) in the context of large scale collision, or related to NE-SW oriented compression that later produced the Oko displacement (Abdelsalam, 1993).

In the above context the compressional structures (D_3) are interpreted to suggest oblique collision in NW-SE direction that possibly followed NW subduction of the Baraka Terrane. It has been difficult to constrain the axial trace of the main thrust zone, but the present central axis of the shear zone is seemingly a representation of among several such planes. Progressive deformation and possible dextral shearing further complicated the deformation events, and gave way to the chiefly left- lateral transpressional tectonics (D_4) at a later stage, accompanying a change in the stress field. The latter facilitated the emplacement of some of the late-orogenic plutons by serving as a migration path, whereas those N of this zone are thought to represent a subduction/collision related magmatic arc. The D_2/D_3 events are believed to make part of the Pan-African accretion tectonics over the Nubian Shield that took place against the now reworked Nile Craton to the W/NW (see also Abdelsalam and Stem, 1993). The collision was followed by uplift/mountain-building and denudation, and no evidence of post-orogenic extension has been observed.

However, the limited observations made seem encouraging to interpret the ATTSZ as an ophiolite-decorated suture, lack of substantial information over geochemical characteristics of the adjoining rocks, detailed history of structural developments, lithologic association, absolute age dates, and implications on tectonic settings etc., leave many arguments open. Nevertheless, in addition to the suggestion by Abdel Rahman (1993) that the Abu Samar area in the NW represents an ophiolite sequence, as also referred by Wipfler (1994) and Haenisch (1997), to be considered in accretion models to be proposed for the region, the present work may also provide some constraints on Pan-African evolution of the Haya Terrane of the Southern RSH and particularly to the area S of the Abu Samar Ophiolite.

Rocks of the "Toilik Series" in the NW, which are metamorphosed under regional amphibolite facies conditions (Kroner *et al.,* 1987), have been related to Lower-Middle Proterozoic rocks of the Sudan (Vail, 1988). If this distinction is valid, as for the gneissic rocks of eastern Derudeb map-sheet defining the Baraka Terrane, their isolated occurrence is likely to be related either to erosional effects that left behind remnants of the underlying gneissic sequence after plutonic emplacements at shallow levels or a possibly tectonic juxtaposition.

In the latter case they represent an exotic terrane whose occurrence is to be related to the geodynamic evolution of the nearby Emasa Shear Zone (Wipfler, 1994) and the Abu Samar ophiolite (Abdel Rahman, 1993). A contact metamorphic effect from the batholithic plutons in the area suggested by Kröner *et al.* (1987) looks unlikely to explain similar extensively exposed rocks occurring further N around Emasa Shear Zone (Haenisch, 1997) and in the southeastern part of the study area (Baraka Terrane, this work). In view of the above facts the relationship between the high-grade and the greenschist rocks is also interpreted to be a tectonic contact, at least in this part of the study area, in contrary to Embleton *et al.* (1983) who proposed a gradational relationship, and Hassan (1991) who thought the former were derived from the latter.

Sedimentary rocks in the area of interest have been related to lacustrine environment and they are believed to make part of the Nubian Supergroup (Hassan, 1991), that ranges between Ordovician and Cretaceous (Vail, 1988). On the other hand, Semtner (1993) indicated the occurrence of mainly Paleozoic sediments, with minor Mesozoic strata, near the Sasa Plain NW of Port Sudan, all of which were previously given a Cretaceous age (Almond, 1986). In the absence of substantial evidences, it appears difficult to classify the Odi sedimentary rocks in any of these age groups. Furthermore, such correlation may be erroneous since the deposition was probably restricted to individual basins which may not have been connected.

Nonetheless, if the regional correlation is substantiated, the Odi sediments may be correlated to the Dirurba Formation (Semtner, 1993) for its similarly rift-controlled nature and geographic proximity coupled with the comparable lithologic association. Their restricted occurrence in the Odi area, in this case, is to be ascribed to a major pre-Oligocene uplifting event over the RSH as a whole which facilitated significant erosion from its most parts. On the other hand, normal faulting and graben formation associated with subsequent volcanism are certainly responsible for their preservation in the Odi area. The absence of these sediments in the NE (Jibal Adar Ribad) is to be explained by longer and intense erosion in this part long before the onset of volcanism during Oligocene, possibly related to this uplifting (see also Almond, 1986) which progressed westwards, and the lack of conducive environment for preservation. Although it is difficult to estimate the amount of sediments eroded or the extent of uplift involved, from the available data, this interpretation, however, conforms with what has been proposed by Semtner (1993) for the Dirurba Formation.

If the above regional correlation is not valid, which most likely the case is, it is apparent that the sedimentation was rather restricted to a local sedimentary rift basin. This interpretation is supported by the fact that the conglomerates contain rock fragments exclusively from the basement units, which implies rift-flanks not covered by sedimentaiy rocks. Furthermore, occurrence of intercalated Oligocene volcanic rocks within the sedimentary sequence (Section 2.2.3) and the observed subaqueous extrusive units indicate low-elevation conditions with no/negligible uplifting/doming before magmatism. Lack of angular unconformities between the volcanics and the underlying sediments can also be used to support that uplifting did not pre-date magmatism (31 Ma ago). Similar interpretation has been given by Menzies *et al.* (1992) for the same regional magmatism that extended over NE Africa and Arabia based on studies in southern Yemen. No indications were also observed, for the Odi are, that favour block faultings that were initiated through uplifting but through crustal extension. The fact that the distribution of the volcanic rocks is controlled by the fault blocks further corroborates this argument.

The Odi rift basin may then represent one of the earliest Phanerozoic extensional tectonics of unknown dimension in the area. However, the upper age of the sediments remains to be unconstrained in both cases, although Almond (1986) indicated tectonic stability of the region until the Late Mesozoic. In contrary to Semtner (1993) who suggested an uplifting phase for the Dirurba area before the Red Sea doming, the Odi rift basin is thought to have been preceded by extension, as bimodal volcanicity is commonly related to rifting environments (eg. Stem *et al.,* 1991). Although fission track data are lacking in order to establish the time relationships between magmatism, rifting

and uplift it may be suggested that the existing data may not easily fit into the known active or passive models of rifting. As Menzies *et al.* (1992) suggested a possibility of more complex relationship (magmatism-extension-uplift) for Yemen, it is likely that for the study area the relationship rifting-magmatism-uplift applies for the early tectono-magmatic phase. This time relationship is in good agreement with what has been suggested by Almond (1986), that Afro-Arabian doming occurred around 10 Ma ago, and early crustal extension in the region was related to subsidence and not uplift/doming, in addition to the generally accepted exhumation in Saudi Arabia, Yemen and southern Red Sea to have started 20-15 Ma ago (Menzies *et al.,* 1992). In this context the Late Oligocene magmatic activities identified in the Odi and Adar Ribad areas are not only coeval, but also belong to the same regional exhumation episode that prevailed in parts of Ethiopia, Yemen, Saudi Arabia and Egypt during this time.

Although extension estimates appear difficult with the available limited data, a maximum of 2 km has been suggested for the Odi area based on strata! dips. The Adar Ribad area is more complicated and further work is obviously needed, but the area possibly underwent a larger amount of extension (about 45° westerly strata! dips and much steeper faults). It is to be inferred, therefore, that extension increases towards the margins of the Red Sea, similar to the flank uplifting.

The Adit-Langeb Lineament has been identified to be a Pan-African sinistral fault (Section 2.2.4) of regional significance not only for its extension (-300 km) to the Red Sea coast (see also Haenisch *et al.,* 1996) but also for controlling the occurrence of the Odi volcanics. Furthermore, it trends apparently subparallel to the known Baraka Suture (to the E) and Hamisana Shear Zone (Figure 2.1) that represent Pan-African major strike-slip sutures (eg. Vail, 1985; Kroner *et al.,* 1987; Shackleton, 1994). The latter has been evolved *ca.* 620-560 Ma ago (Shackleton, 1994) and have been ascribed by some workers to have significantly controlled major structural patterns during the Red Sea rifting (eg. Schandelmeier and Pudlo, 1990; Makris and Rihm, 1991). It is suggested that the Adit-Langeb lineament is also a deep-seated Pan-African fault of regional importance which have possibly acted as a major detachment zone during later rifting events. Neotectonic events in the area are marked by the N-S drainage pattern parallelling the active Red Sea opening.

The NE trending Tashalal-Langeb Lineament substantially controlled the Early Miocene extension process by acting as an active transfer fault among which the differential movements on either sides were accommodated. This lineament is parallel to the ATTSZ and it has certainly exploited this weak zone. Furthermore, the fault parallels the famous Central African Fault Zone that is known to have possibly acted as a continental transfer fault in the western Sudan (Schandelmeier and Pudlo, 1990), and importantly active during the early stage of Red Sea opening (Makris and Rihm, 1991).

3 Remote Sensing

3.1 Historical Background

Remote sensing is broadly defined as collecting and interpreting information about a target, without being in physical contact with the object, through the link of electromagnetic energy (Sabins, 1987). It focuses on the capture of information about the Earth's properties in the nearly continuous, two dimensional pattern that is characteristic of images, in a spectrum that ranges from gamma-rays to microwave radiation (Drury, 1993).

The historical development of remote sensing started with photographic systems in the early 1830's that were based on optical cameras, and developed to the first photographs from balloons around 1858 (List, 1992). With developments in sensitive film materials since then, the first aerial photographs were obtained from kites in 1890 and from aircraft in 1909 (Lillesand and Kiefer, 1994). Infrared and coloured films were invented in the 1930's, and aerial photographs were first used for operational oil exploration in 1938.

Side-looking airborne radar came into use in the 1950's, and was later refined to Synthetic-Aperture Radar (SAR). The manned Gemini and Apollo missions of the 1960's, followed by the Skylab mission in 1974 and Space Shuttle experiments of the early 1980's marked significant achievements in observing the Earth (Sabins, 1987). These were succeeded by photographs from Shuttle-based Large Format Camera (LFC) and Shuttle Imaging Radar (SIR) in 1984 (Sabins, 1987).

With the advance in semi-conductor technology and computer sciences began a new era in the history of remote sensing; it was marked by the launch of the Earth Resources Technology Satellite (ERTS-1), now named Landsat-1, in 1972. This system carried the Multispectral Scanner (MSS) and Return Beam Vidicon (RBV) that provided data of world wide distribution, to be later followed by Landsat-2 and -3, respectively. These sensors paved the way to the development of the Thematic Mapper (TM) that has been used on Landsat-4 and -5 in 1982-83 and since 1984, respectively. This was followed by orbiting sensor system of the Systeme Probatoire de FObservation de la Terre (SPOT) in 1986, with improved spatial resolution and stereoscopic coverage, and the Indian Remote Sensing Satellites (IRS-1A and IRS-1B) in 1988, of unmanned spacecrafts.

Recent technological advances permitted the design of solid-state scanners that have been used by the Space Shuttle-based Modular Optical-Electronic Multispectral Scanner (MOMS) system (Gupta, 1991). TheERS-1 radar-satellite and other resource satellites like JERS-1 were among those to be in orbit in early 1990's, being followed by the Radarsat (Drury, 1993).

Future prospects for land-oriented remote sensing include the Earth Observing System (EOS) scheduled for 1998. It includes the Advanced Spacebome Thermal Emission and Reflection Radiometer (ASTER) that uses few narrow wavebands strategically placed about useful spectral features important for geologists (Drury, 1993). After the successful use of hyperspectral data for detailed spectral features High Resolution Imaging Spectrometer (HIRIS) and Moderate Resolution Imaging Spectrometer (MODIS) are also among instruments to be on the missions of the EOS series (Drury, 1993). Many standard remote sensing books give substantial information on its historical developments, although data over future prospects are less available for the common reader.

3.2 Some Basic Principles

In remote sensing electromagnetic radiation (EMR) is the communication link between the sensors and the object under consideration. And it is the transported energy that can be measured and provide information on the nature of the radiant object (List, 1992). The wavelength of this spectrum may span from gamma-rays (< 0.001 nm)

to long radio waves (>100 km) (Drury, 1993). In this range the frequency or the wavelength is directly proportional to energy of the quanta; the shorter the wavelength or the higher the frequency of EMR, the greater the energy of each quantum (Drury, 1993).

The Sun is the most important source of radiation reaching the Earth's surface. Incident electromagnetic radiation at a particular wavelength onto a surface may be transmitted through the material, absorbed within it, emitted at another wavelength after absorption, scattered by its constituent particles or reflected by its surface. The latter three are called surface phenomena, since these interactions are primarily determined by surface properties such as roughness, whereas the former two are known as volume phenomena, because internal characteristics of the matter such as density and conductivity determine these interactions (Sabins, 1987). The specific features of surface and volume interactions with a particular object depend on both the wavelength of the EMR and the properties of the object. Absorption (and its inverse transmission), reflection and emission spectra can generally be measured.

Every matter radiates a range of electromagnetic energy that is temperature dependent; the peak intensity progressively shifts towards shorter wavelengths with increasing temperature of the matter. This gives 0.5 */urn* the wavelength with the maximum reflected energy and 9.7 m the highest radiant energy for Sun's 6000°K and Earth's 300°K ambient temperature, respectively (eg. List, 1992; Gupta, 1991).

Different types of reflection are known: specular reflection, diffuse reflection and mixed (specular and diffuse) reflection. Specular reflection occurs when all the reflected energy is directed away at an angle equal and opposite to the angle of incidence whereas in diffuse reflection the reflected energy is directed equally in all directions irrespective of the angle of incidence (List, 1992). Generally, a surface behaves as diffuse if the roughness is greater than that of the wavelength of EMR, and as specular (smooth) if the surface roughness is finer than the wavelength. Most surfaces such as rocks and soils are diffuse reflectors in the visible spectrum.

In remote sensing two types of systems are known depending on the source of radiation used: a passive and active systems. In passive systems the existing radiation is recorded, the source of the reflected or emitted energy being the Sun. Other sources for emitted radiation include flow of radiogenic heat from the Earth's interior, heating of the surface by solar radiation, and human activities (Drury, 1993). The Radar system is a good example of an Active system, involving an artificially induced energy source.

Before reception by a satellite-mounted sensor, solar radiation must pass down through the atmosphere and then back again to the sensor as reflected energy. For emitted energy the path is one way; from the Earth's surface to the sensor. In addition to oxygen and nitrogen the atmosphere contains significant amounts of water vapour, ozone and carbon dioxide. All of them differently interact with EMR, and due to this effect part of the energy is absorbed at specific wavelengths. Because of this only a small part of the EMR is usable by remote sensing of the Earth's surface, being limited to those wavebands that pass relatively unaffected through the atmosphere, also termed as atmospheric windows (eg. Drury, 1993). The atmospheric windows and wavelength ranges affected by the different atmospheric constituents are give in several standard remote sensing books (eg. Sabins, 1987; Lillesand and Kiefer, 1994).

Considering the solar irradiation outside the atmosphere, therefore, it is the reflected energy that is significant for remote sensing in the range 0.4-2.5 */j.m* (visible, very near-infrared, and short-wave infrared) whereas in the ranges 3-14 /zm (thermal or mid infrared) radiant energy is recorded. The microwave region (1 mm - 1 m) is commonly sensed by radar systems that use artificial incident energy. The latter is less affected by the atmospheric constituents including haze, light rain and snow, clouds, and smoke (Lillesand and Kiefer, 1994).

3.3 The Landsat Systems

Landsat represents an unmanned medium to high resolution orbital sensor system aimed at the biological and physical resources of the Earth. It is a Sun-synchronous system that circles the Earth at a near-polar orbit. There are two generations of the Landsat corresponding to different technology and platform: Landsat- 1, -2 and -3, and Landsat-4 and -5. On the first generation of Landsat data were either relayed directly to ground receiving station or recorded by an on-board tape recorder until the platform is above a receiving station. They also carried a non-imaging Data Collection System (DCS) that relayed information from sensors to the receiving stations on the Earth. On Landsat-4 and -5 data are telemetered to the ground either directly or via a series of Tracking and Data Relay Satellites (TDRS) (Sabins, 1987). Table 3.1 gives the major characteristics of the Landsat systems.

The first generations of Landsat were equipped with a three-channel (except Landsat-3 that had high resolution panchromatic mode) Return Beam Vidicon (RBV) and widely used four-band Multispectral Scanner (MSS) aimed at visible and VNIR bands. The MSS is a cross-track scanning system with an oscillating mirror that scans a swath of 185 km wide normal to the orbit path. The scan angle was 11.56°, and image data were recorded only during the east-bound sweep. At an altitude of 918 km the 0.087 mrad Instantaneous Field of View (IFV) produced a ground resolution cell of 79x79 m^2.

Landsat-4 and -5 differ from the older Landsat series in carrying the Thematic Mapper (TM), in addition to the MSS, that not only provides images with an improved spatial resolution but also extended spectral coverages useful for geological studies. The TM is a line scanner system that collects data in both east- and west-bound sweeps seven times per second, which improves radiometric accuracy. Image data are recorded in 7 bands, six in visible and reflected IR and one in thermal IR. With a reduced altitude of 705 km, and a swath of 185 km, the ground resolution in TM is about 30x30 m^2 (except the thermal band which has 120x120 m^2). The MSS on Landsat-4 and -5 are similar to those used during the first generation of Landsat. More details on the operation mechanisms, and data recording and transmission of the Landsat system are given in Sabins (1987). Table 3.2 gives the spectral bands and characteristics of the TM and MSS sensors.

Table 3.1. Some orbital characteristics of the Landsat systems. After Sabins (1987).

Parameters	Landsat-1, -2 & -3	Landsat-4 & -5
Weight of spacecraft	815 kg	2000 kg
Altitude (nominal)	918 km	705 km
Orbital period	103 min.	99 min.
Orbits per day	14	14.5
Number of path	251	233
Orbit inclination at equator	99°	98.2°
Local crossing time at equator (approx.)	9:30 a.m.	9:45 a.m.
Image sidelap at equator	14%	7.6%
Repeat cycle of coverage	18 days	16 days
Distance between ground tracks at equator	2760 km	2753 km

For remote sensing studies the recorded energy are converted to gray ranges or unitless digital numbers (DNs). The DN values for a particular sensor depends on the available range of depth. It is this DN values that are processed in digital image processing. Some more information on relationships between gray values and radiance are given in Lillesand and Kiefer (1994).

3.4 Important Spectra of Rocks and Minerals

Rocks are assemblages of minerals, and so their spectra are a composite of each of their constituents. Elements that in turn comprise minerals, therefore, characterise the spectral features of rocks.

Table 3.2. Characteristics of the Landsat TM and MSS bands and their principal applications. After Sabins (1987).

Band	Wavelength (in *pim)*	Characteristics and principal applications
1	0.45 - 0.52	Blue-green, no MSS equivalent. Maximum penetration of water, useful for bathymetric/coastal studies. Useful for distinguishing soil from vegetation and deciduous from coniferous plants and cultural feature identification.
2	0.52 - 0.60	Green, coincident with MSS band 4 (0.5-0.6 /zm). Matches green reflectance peak of vegetation, which is useful for assessing plant vigour.
3	0.63 - 0.69	Red, coincident with MSS band 5 (0.6-0.7 /zm). Matches a chlorophyll absorption band that is important for discriminating vegetation types.
4	0.76 - 0.90	Reflected IR, coincident with portions of MSS bands 6 (0.7-0.8/zm) and 7 (0.8-1.1/zm). Useful for discriminating biomass content, vigour and vegetation types, and for mapping shorelines and soil moisture discrimination.
5	1.55-1.75	Reflected IR. Indicates moisture content of soil and vegetation. Penetrates thin cloud, used to discriminate it from snow. Good contrast for vegetation types.
6	10.40-12.50	Thermal IR. Nighttime images are useful for thermal mapping, vegetation stress analyses and estimating soil moisture.
7	2.08-2.35	Reflected IR. Useful for discrimination of minerals and rocks (coincides with absorption band caused by carbonate and hydroxyl ions in minerals). Also sensitive to vegetation moisture content.

Electronic transitions within atoms themselves require more energy than vibrational processes within molecules. Therefore, the former generally characterise the short wavelengths (UV, VIS and NIR) whereas the latter mainly dominate features in the longer wavelengths (SWIR).

The most common rock forming minerals and the elements of which they consist are oxygen, silicon, and aluminum together with different proportions of iron, magnesium, calcium, sodium and potassium, and smaller amounts of other elements. Oxygen, silicon and aluminum atoms have electron shells whose energy levels are such that transition between them have little or no effect on the visible to near-infrared ranges. Iron is rather the most influential mineral in this part due to crystal-field and charge-transfer effects (Hunt *et al.,* 1971). The former occurs due to discrete electronic transitions in ferrous (Fe^{2+}) ions in different symmetry, type of ligand, degree of lattice distortions and their coordination (Gupta, 1991). For the same reason absorption features of 0.87 (iron oxide), 1.0 /zm (amphiboles and olivines), 0.7 *fjm,* 1.0 /zrn and 1.8 ptm (pyroxene) appear to be more common. Manganese (Mn^{2+}) exhibits absorption features mainly at 0.41 /zm, 0.45 m, and 0.55 *m*. Charge-transfer effect is often responsible for a broad absorption band at wavelengths shorter than 0.55 /zm in most iron-bearing minerals because of migration of electrons from iron to oxygen (Hunt *et al.,* 1970). Rocks and minerals containing iron oxides and hydroxides, therefore, exhibit yellow, orange and red colours because of this declined reflectance towards the blue end of the spectrum, and a general rise towards the infrared (1.3-1.6 /zm) region.

In the SWIR parts of the spectrum the most important vibrational transitions in minerals are those associated with the presence of anionic constituents of minerals, i.e. hydroxyls and carbonates, or water molecules. Absorption features at 1.9, 1.4, 1.14 and 0.94 /zm are diagnostic of the presence of molecular water in minerals. Many silicates and alteration minerals contain hydroxyl ions, which produce absorption features near 2.3 and 2.2 /zm when bonded to Mg and Al, respectively (Drury, 1993), and when they

occur together, the former band predominates the latter. These features are prominent in aluminous micas and clay minerals and form signatures for other hydroxylated minerals containing magnesium, such as chlorite and serpentines. When iron is substituted for these elements the electronic bands in 0.4- 1.0 /zm predominate (Hunt *et al.,* 1971). Similar vibrational processes also characterise carbonate minerals which give rise to a number of absorption features in the SWIR of which that around 2.3 /zm is the most prominent.

In the thermal infrared part of the spectrum different silicate structures (isolated tetrahedra, chain, layered, three-dimension) exhibit different emission spectra that are related to Si-0 bond vibrations. The peaks (at shorter wavelength) and main troughs (at longer wavelength) of the emission/transmission spectra shift progressively towards longer wavelength corresponding to a transition from felsic to increasingly mafic minerals (Drury, 1993). Phosphates, sulphates and nitrates are also known to exhibit vibrational processes in the thermal infrared.

Mafic igneous rocks commonly contain pyroxenes, amphiboles and magnetite which contain ferrous and/or ferric iron giving absorption bands at 0.7 and 1.0 /zm. In ultramafic rocks the ferrous band becomes increasingly prominent because of more opaque minerals and Fe^{2+}-bearing minerals, whereas granites show weak absorption bands related to OH' and H_2O (Gupta, 1991). Sedimentary rocks generally have a hydroxyl-water absorption bands at 1.4 and 1.9 /zm, in addition to those characterizing carbonate rocks at 1.9 and 2.3 /zm. Water and hydroxyl bands at 1.4 and 1.9 /zm are displayed by many schists, quartzite and marble, in addition to absorption bands at 1.9 and 2.3 /zm that characterise the latter.

Under natural conditions minerals are assembled in different proportions in rocks, and their spectra interfere accordingly. More importantly, they are rarely fresh but covered with thin layers of weathering products or desert varnish in arid areas. Since visible and NIR radiations interact only with the outer few micrometers of the Earth's surface (Buckingham and Sommer, 1983), spectra of fresh minerals rarely influence the reflected radiation recorded by many remote sensing platforms. To a large extent, however, the weathered products of rocks, such as soil, constitute similar minerals as the underlying bed rock and with the exception of altered minerals that display a different mineralogical composition, the spectral features of the bed rock are fairly represented. This problem has been partly dealt with in Section 5, with particular application to desert varnish for mapping alteration zones in the RSH, Sudan.

4 Digital Image Processing

Digital image processing involves the manipulation and interpretation of digital image (Lillesand and Kiefer, 1994), and it generally comprises four major steps: image rectification, registration, enhancement, and classification. Image rectification includes the correction of recorded digital data in respect of various geometric and radiometric distortions, whereas superimposition of different images over one another, or onto a standard map projection is called image registration (List, 1993). Image enhancement includes processes that render certain features of interest in an image more interpretable, and image classification is concerned with categorisation of pixels of a scene into various thematic groups based on spectral response. In the following sections the processing steps undertaken by this work will be discussed.

For the present study all digital image processing was conducted at the Institute of Geology, Geophysics and Geo-informatics, Free University of Berlin, Germany. For this purpose PC-based ERDAS (7.5) on a VAX 4000 server, and ERDAS IMAGINE (8.2) software installed on SUN SPARCstations have been used. Mainly Landsat TM, and in few instances Landsat MSS, data have been processed. The data were captured on 06.10.1985, path/row 171/48, and are cloud free. More specifications about the data used are given in Appendix-1.

With the interest of saving computer space and processing time the Odi subscene (76.8x61.44 km^2) was selected in the central Derudeb map sheet (Figure 4.1) for all image processing steps. The test area has been selected for the occurrence of diverse rock types in a relatively closer range. Processed images were evaluated and interpreted both on-the-screen and by using hard copy outputs from IRIS printer at the scale of 1:100 000. The geological interpretation map made for the Odi subscene, after combining information from different processing algorithms, is shown for comparison on Figure 4.4.

4.1 Data Preparation

4.1.1 Image rectification

Random geometric distortions are often corrected by analysing well distributed Ground Control Points (GCP) whose locations are accurately known in the map and also occur in the image to be rectified (List, 1993). The GCPs can also obtain map coordinates from Global Positioning System (GPS) readings, based upon which coefficients for coordinate transformation are computed. These coordinates will then be used for rectification of the whole image, whereby all the pixels will obtain new map coordinates, and grey value, through a resampling technique (Lillesand and Kiefer, 1994).

The Landsat TM and MSS images covering the study area were georeferenced at the initial stage of the work to ease registration of the different data sets at any stage of the study and to obtain the correct geometric positions of the ground objects. To this end, about 40 GCPs were selected and encoded from topographic maps with a scale of 1 : 100 000 obtained from the Sudan Survey Department. In the georeferencing step the data were transformed to the Universal Transverse Marcator (UTM) coordinate system using the Clarke-1880 spheroid in conformity with the topographic map. The coordinate transformation was conducted by using first order polynomials, and the root-mean-square error tolerance was set at a maximum of 2 pixels (60 m). Finally, the generated transformation matrix was used for resampling of the pixels by employing the "nearest neighbour" method. This method was preferred over the others because the pixel grey values of the original data are retained, unlike high order transformations (ERDAS, 1982-1994), and this is obviously important for such a qualitative study. The pixel size has been kept at 30 m in order not to loose the spatial resolution of the Landsat TM data.

4.1.2 Band selection

The Landsat TM with its seven bands contains a wide range of spectrally diverse data. For the purpose of image display only three bands or band combinations, each directed to one of the primary colour-guns (red, green, and blue), are required. Moreover, since proper band combinations are needed to enhance a desired target, and avoiding the redundancy of information contained in the different bands is often desired, target-oriented band selection remains unavoidable step in most multi-band data processing.

Various workers have suggested different statistical methods in which *a priori* knowledge is not required in band-triplet selection for geological purposes. The Optimum Index Factor (OIF) proposed by Chavez *et al.* (1982) is obtained by normalizing the sum of the standard deviation of the bands (in band composite) by the sum of the absolute values of their correlation coefficients. The band-triplet having the maximum OIF should have the least amount of redundancy and maximum information (Chavez *et al.,* 1982).

The method proposed by Sheffield (1985) involves computation of the determinant for each band-triplet using its 3x3 variance-covariance matrix. Generally the determinants are considered to be proportional to the volume of the data-ellipsoid, that means the composite having the largest determinant contains the maximum information (Sheffield, 1985).

Crippen (1989) and Liu and McM. Moore (1989) proposed approaches principally based on correlation coefficients, rather than band variances. According to Crippen (1989) the determinant of the correlation coefficient gives an index which indicates the three dimensional nature of the band-triplet. In this approach a value of one shows perfect three dimensionality and corresponds to the least correlated band-triplet. The Index of Optimum Band Selection (IOBS) by Liu and McM. Moore (1989) gives small values to a band triplet having a correlation cube with the shortest diagonal line and largest volume, thus maximum information. The amount of information is thought to correspond to the spectral contrasts.

The above illustrated methods were computed for the Odi subscene using the four MSS and six reflective bands of the Landsat TM, TM band 6 being omitted for its less informative nature and poor spatial resolution. Tables 4.1a and b show the ranks of the various band-triplets against the different statistical methods, and the obtained results for TM and MSS data, respectively.

As it can be seen from Table 4.1a, for Landsat TM data, no exact corroboration between the different statistical methods is exemplified in selecting a particular band-triplet. However, the results obtained by the methods of Crippen (1989) and Liu and McM. Moore (1989) show significant agreement for obvious reasons. For the other two methods triplets containing band 5 and/or 7 tend to rank high for their high variance (Table 4.2) as expected. In general, band combinations involving only the visible part of the EM spectrum appear to rank consistently low in all the methods because of the very high correlation coefficient (see also Crippen, 1989) and/or low variance, accordingly. It may be summarised that in all the approaches, except the OIF, band-triplets constituted by each band from the visible (VIS), near-infrared (NIR), and middle infrared (MIR) regions apparently rank high (Table 4.1a).

Visual inspections of the various band-triplets obtained for TM data have been carried out in order to support the statistical methods, by often assigning the colours green (G), red (R) and blue (B) to bands with the order of decreasing variance (Sheffield, 1985). Geological information is generally well contained in many of the high ranking band combinations. However, the hue contrast between the different lithologic units is apparently enhanced in band-triplets 7 4 1, 5 4 1, and 5 3 1 (in R G B). Considering the high reflectance of most rocks in TM-5 that may result in data overflow in highly reflective areas (eg. Kaufmann, 1988) like the RSH, and the spectral significance of the TM bands in geologic context (see Crippen, 1989), the first band composite has been selected as the best triplet for further image processing steps as required.

Table 4.1. Results of different statistical methods for best band-triplet selection applied to the Landsat TM reflective bands (a), and MSS data (b) covering the Derudeb area.

a)

Method	OIF (Chavez et. al., 1982)		Determinant (Sheffield, 1985)		Correlation Index (Crippen, 1989)		IOBS (Liu & McM Moore, 1989)	
Rank	band-triplet	value	band-triplet	value	band-triplet	value	band-triplet	value
1	3, 5, 7	21.32	1, 4, 5	402050	1, 4, 7	0.166	1, 4, 7	0.828
2	4, 5, 7	20.77	1, 5, 7	321393	1, 4, 5	0.134	1, 4, 5	0.849
3	1, 5, 7	20.54	3, 5, 7	307336	2, 4, 7	0.125	1, 3, 7	0.867
4	3, 4, 5	20.00	1, 4, 7	259621	1, 3, 7	0.123	1, 5, 7	0.8873
5	1, 3, 5	19.58	1, 3, 5	241258	1, 5, 7	0.116	2, 4, 7	0.874
6	1, 4, 5	19.18	4, 5, 7	231542	1, 3, 5	0.1016	1, 2, 7	0.883
7	2, 5, 7	19.15	3, 4, 5	194030	2, 4, 5	0.1014	1, 3, 5	0.886
8	2, 3, 5	18.26	1, 3, 7	148820	1, 2, 7	0.1012	2, 5, 7	0.893
9	2, 4, 5	17.85	2, 5, 7	125562	2, 5, 7	0.100	2, 4, 5	0.896
10	1, 2, 5	17.14	3, 4, 7	125453	3, 4, 7	0.091	3, 4, 7	0.902
11	3, 4, 7	17.13	2, 4, 5	106472	3, 5, 7	0.089	4, 5, 7	0.903
12	1, 3, 7	16.54	2, 4, 7	62781	4, 5, 7	0.088	3, 5, 7	0.905
13	1, 4, 7	16.15	1, 2, 5	58621	1, 2, 5	0.087	1, 2, 5	0.901
14	2, 3, 7	15.28	2, 3, 5	37650	3, 4, 5	0.073	2, 3, 7	0.912
15	2, 4, 7	14.87	1, 2, 7	32863	2, 3, 7	0.067	3, 4, 5	0.925
16	1, 3, 4	14.61	2, 3, 7	27694	1, 2, 4	0.059	2, 3, 5	0.932
17	1, 2, 7	14.05	1, 3, 4	22358	1, 3, 4	0.057	1, 2, 4	0.934
18	2, 3, 4	13.46	1, 2, 4	6473	2, 3, 5	0.056	1, 3, 4	0.935
19	1, 2, 3	12.58	2, 3, 4	3604	1, 2, 3	0.032	1, 2, 3	0.963
20	1, 2, 4	12.26	1, 2, 3	2837	2, 3, 4	0.031	2, 3, 4	0.964

b)

Rank	band-triplet	value	band-triplet	value	band-triplet	value	band-triplet	value
1	1, 2, 4	12.0	2, 3, 4	1944.89	1, 2, 4	0.068	1, 2, 4	0.925
2	2, 3, 4	10.75	1, 2, 4	1653.2	1, 3, 4	0.054	1, 3, 4	0.938
3	1, 2, 3	9.8	1, 3, 4	1381.0	1, 2, 3	0.047	1, 2, 3	0.950
4	1, 3, 4	9.46	1, 2, 3	1225.6	2, 3, 4	0.039	2, 3, 4	0.954

The above statistical approaches were also applied to the four MSS bands covering the Odi subscene to select the best band composite (Table 4.1b). The result shows that the composite 1 2 4, with the possible exception to the determinant method of Sheffield (1985) where it ranked 2nd, appears to be the best composite in the other three methods. The ranking order of band composites in the methods given by Crippen (1989) and Liu and McM. Moore (1989) are apparently identical, revealing their perfect conformity. The composite 2 3 4 ranked 1st by the determinant method for the reason that band 1 has the least variance/standard deviation (Table 4.2). Visual inspection of the possible four band composites also corroborates the above result.

4.1.3 Haze correction

As stated earlier in Section 3.2, spacebome optical sensors recording data in the range between the visible and short wave infrared spectrum (0.4-2.5 */j,m)* receive solar radiation reflected from the Earth's surface and radiation scattered by the atmosphere. Since the atmospheric effect modifies the radiation reflected at the ground by reducing image contrast, and contributes an additive term, correction for this term is necessary in order to detect "only" the surface reflectance. Accurate estimation of this value requires precise measurements of atmospheric parameters like temperature, humidity, visibility, atmospheric pressure etc., which are unfortunately hardly available over large areas (List, 1993). Crippen *et al.* (1988) summarised the principles of the most commonly used scene-based methods for removing atmospheric scattering or path radiance, or often called haze.

One of the image-based simple but yet effective methods for haze correction has been given by Crane (1971). The method, known as "dark-pixel subtraction" or the "histogram minimum" is based on the assumption that somewhere in the image there is a pixel with zero illumination or reflectance, such that the radiometric contribution from this pixel represents only the additive term. It is further assumed that the atmospheric scattering throughout the scene is uniform. According to this approach the histograms of each band are examined and shifted towards lower grey values by a constant that is supposed to represent the additive term of haze. One disadvantage of the method is that such pixels may not be confidently known to exist in many images (Crippen, *et al.,* 1988).

Examination of the TM scene covering the Odi area shows that the area exhibits highly rugged morphology, as also verified during the reconnaissance field work. The simplicity of the method coupled with the high possibility of the existence of dark pixels in the scene and the seemingly uniform atmospheric condition, have encouraged the adoption of this method. Accordingly, for the Odi area the subtracted grey values were 57, 18, 15, 6, 4 and 1 for TM bands 1 through 5, and 7, respectively, in order to obtain a gain of zero (Table 4.2). For the MSS data values

Table 4.2. Statistics of raw data covering the Odi subscene; MSS (a) and reflective TM bands (b) rounded to the nearest decimal.

a)

Bands	1	2	3	4
Minimum	16	13	7	2
Maximum	70	105	104	80
Mean	41	56	54.9	43.1
Stand, dev.	6.24	10.6	11.7	9.3
Median	43	60	59	47
Mode	40	55	54	45

b)

Bands	1	2	3	4	5	7
Minimum	57	18	15	6	4	1
Maximum	150	91	144	118	220	134
Mean	97.6	47.7	67	54.1	98.7	63.8
Stand, de.	11.6	9.1	15.8	14.1	26.3	17
Median	97	48	67	54	101	65
Mode	99	47	68	53	104	68

of 16, 13, 7 and 2 have been subtracted from bands 1 to 4, respectively.

4.2 Linear Contrast Enhancement

It is a common practice to stretch raw data over the quantized range of grey values (256 for 8-bit data) in order to produce an enhanced image during data processing. The attained enhancement, however, is strongly controlled by the statistics of the input data, namely the mean and the standard deviation. These values significantly influence the resulting colour in image composites since they regulate the brightness of the bands under consideration and thus the corresponding colours. Liu and McM. Moore (1989) proposed a method called Balanced Contrast Enhancement Technique (BCET) in order to overcome such problems, whereby the range and mean are set to user-defined values. The method, however, requires more computational time.

For the present study the colour bias in colour composites caused by the difference in the mean and value ranges has been reduced by individual linear stretching of the raw data of all bands. In this approach, a mean value of 127 and standard deviation of about 41 were obtained. The resulting images have not been interpreted, but used for further processing as stretched data when needed.

4.3 IHS Transformation

IHS transformation is one of the most commonly applied image processing methods used to enhance geologic information. In this process a composite in the RGB colour-space is decomposed into intensity (I), hue (H), and saturation (S) components and manipulated, after which it is retransformed back to the RGB-space for interpretation (Sabins, 1987). Intensity represents the brightness, hue signifies the dominant wavelength, and saturation is related to the purity of a colour (Sabins, 1987). This method is particularly efficient in cases where the bands in the composite are highly correlated and simple stretching brings no satisfactory enhancement. The advantage of this technique also includes that the I, H, or S images may be processed separately at the intermediate step to obtain saturated colours, and that the transformation is independent of the scene statistics (eg. Gillespie *et al.,* 1987).

4.3.1 IHS decorrelation stretching

For the study area IHS transformation was conducted using the band-triplet 7, 4 and 1 in R, G and B, respectively. For contrast enhancement the saturation image has been separately stretched, keeping the hue image substantially unchanged in order to ease interpretation by preserving the spectral information for such a qualitative study (see also Gillespie *et al.,* 1987). The intensity component was also kept unchanged to avoid colour bias to be possibly caused by significant reflectance in such an arid area. The three images were then transformed back to the RGB colour-space and linearly stretched for colour composition.

It has been found that the obtained IHS enhanced image yielded the best result for lithologic discrimination and structural information in the study area. The hue distribution on this composite is similar to its original equivalent but the saturation has been significantly improved thereby facilitating better visual interpretation. Figure 4.1 shows an IHS enhanced image for the whole of the Derudeb area.

On this image, marble, graphitic schists and other metasediments appear in bright blue colour because of absorption bands caused in TM-7 by carbonates and other hydroxylated silicates (Hunt and Salisbury, 1970, 1971). The white marble associated with the gneisses (W of J. Qawayateb) is distinguished from its banded equivalents in the metavolcano-sediments in its light colour (Figure 4.1). Basalt and basic plutons are also in varying dark green to blue colours (high reflectance in TM-1 and 4), against the presence of olivine and pyroxene which contain ferric iron, due possibly

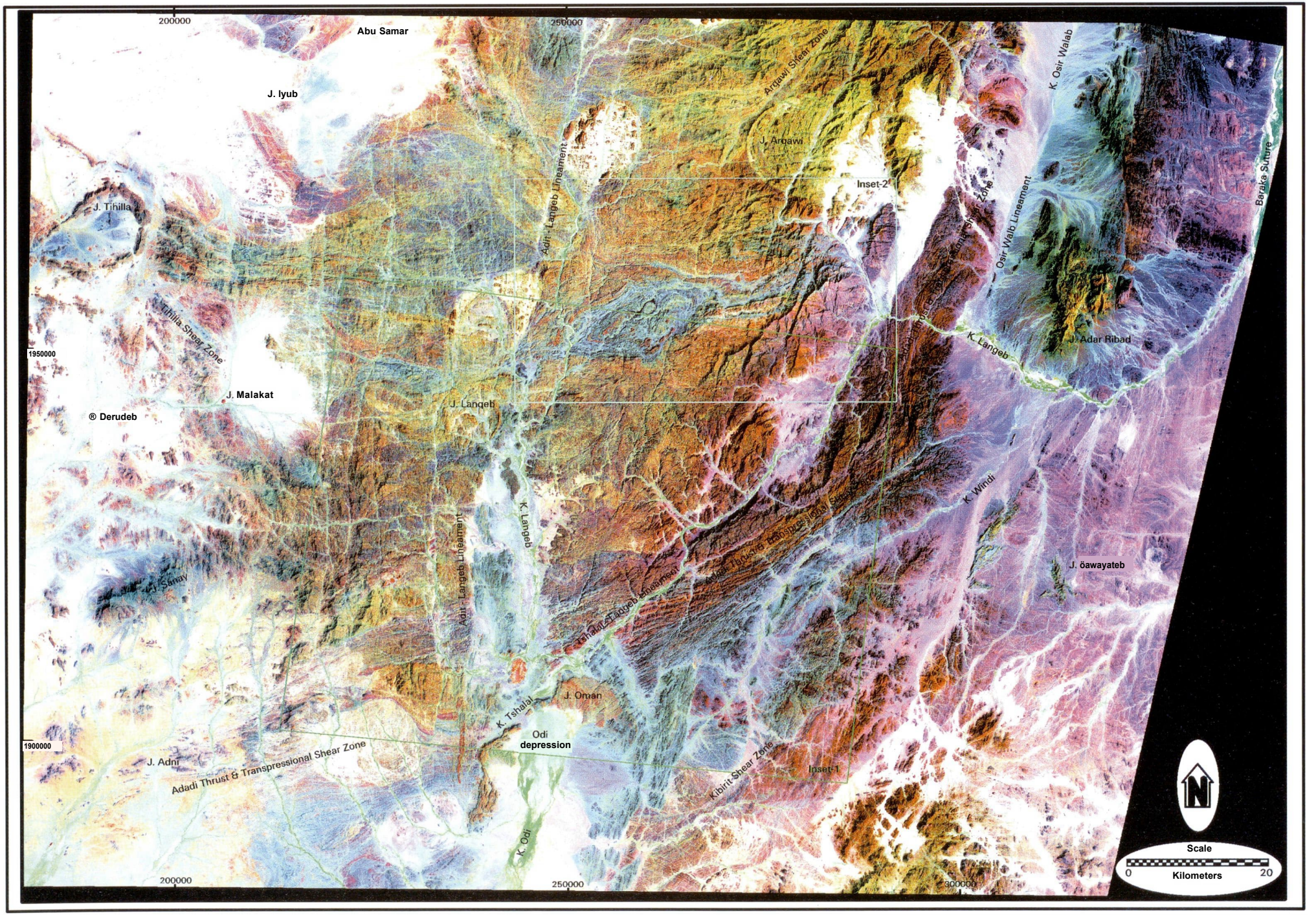

Figure 4.1. IHS decorrelation-stretched image obtained for the Derudeb area using TM bands 7, 4 and 1 in R, G and B, respectively, along with some geographical names referred in the text. Insets 1 & 2 correspond to Odi sub-scene (Figures 4.2a-e & 4.5) and Figure 2.4, respectively. Coordinates are in UTM (spheroid: Clarke 1880). See text for explanations.

to quenching by magnetite that makes absorption bands in the visible range featureless (Hunt *et al.,* 1971) and/or significant absorption in SWIR by hydroxyl-bearing alteration minerals (see Section 5.3) as it commonly the case is. Light coloured rocks such as granite, rhyolite, dacite and quartzofeldspathic schists are generally in hues of red to green for the lack of hydroxylated minerals that have absorption in TM-7 and the overall high reflectance of feldspars and quartz (Hunt and Salisbuiy, 1970).

It should be noted that the granite of J. Arqawi in the NE exhibits a brownish colour that gradually diminishes away from its outer contact, as seen on this image (Figure 4.1). This feature has been considered to display thermal effects whose distribution was facilitated by the abundant fracture systems in the area (Section 2.2.2), as also discussed in Kenea (1997)., unlike a gabbroic rock rimming the granite and defining a ring-structure as suggested by El Labib (1991).

Sedimentary rocks of the Odi area are in distinct light blue to cyan colour, due to major absorption in TM-7 by altered feldspars, carbonate bands, and hydroxyl-bearing minerals. Sandstone on the other hand, with its siliceous cement (Section 2.2.3), exhibits a brownish colour for its compositional similarity with the other acidic rocks. The ultramafics (predominantly talc-schists and pyroxenites) are distinguished from the metasediments in their discontinuous nature and strong morphologic expression rather than hue, as they also contain hydroxylated low-temperature minerals. The high-grade gneisses are in distinct magenta colour because of the absorption by ferric iron in TM-4, and the lack of hydroxylated silicates. Experience has shown that the result can be much improved by using stretched input data. The IHS image has been the basis for image interpretation of the map area.

A similar processing has been conducted using MSS bands 1, 2 and 4 in R, G and B, respectively, selected in section 4.1.4. The obtained image is apparently poor in displaying any lithologic contrast, and distinction of major rock types is rather difficult. This is attributed mainly to the lack of SWIR bands, and low spectral resolution of the MSS in displaying the compositional difference between rock units in conjunction with the high correlation among the MSS bands.

4.3.2 Hue-image composite

Hue images are known to be related to the spectral characteristics of the sensed object (Gillespie *et al.,* 1987) and are thus useful for qualitative studies. They are also free from shadow effects (Liu and McM. Moore, 1989) and may be useful in avoiding topographic effects in relatively rugged terrain like the RSH. In this context it is thought that hue-image composite produced from as many different bands as possible may yield informative results.

In view of these facts an attempt was made to produce hue-image composite using all the TM bands in triplets of 1 2 3, 3 4 5, and 5 6 7 (in B G R), for the Odi area. The band-triplets were chosen so, in order to extract maximum possible spectral information from all the TM bands although repetition of some bands could not be avoided. The obtained composite image appears generally poor for lithologic discrimination, although the hue images are expected to display maximum spectral differences. This is most likely because of the spectral redundancy of most rocks in many of the TM bands. Morphological information appears also generally very poor, making the method less useful for further interpretation.

4.3.3 Cloud-shadow suppression

As one of the primary meteorological factors contributing to atmospheric scattering, cloud cover strongly alters the reflectance from the Earth's surface reaching spacebome sensors. By doing so, it does not only lead to restricted ground coverage, but it also modifies the spectral properties of local objects on the ground and alters the energy budget (Gupta, 1991). An additional problem in such a scene is the shadow of the cloud which again covers additional adjacent area in most data acquired at low sun elevations. It is desirable to

reduce the effect of both the clouds and the cast shadows from such scenes, although it appears to be only possible for relatively thin cloud coverages.

In the early phase of this work only the Landsat TM scene (171/48) acquired on 29.01.1987 was available. The scene contains about 20% of partly dense and patchy cloud covers in its eastern and northeastern parts. It seemed, therefore, worthwhile to investigate the possibility of restoring the image information for such parts of the scene. Close observation of these parts of the scene revealed that some spectral information is still preserved in the shadowed areas, and that they exhibit grey ranges well over the expected value of zero in all the reflective TM bands. The reflectance is higher towards shorter wavelengths due to the higher atmospheric back scattering in this part of the spectrum. The thermal band of the TM contains significant topographic information and is free from cloud-shadow, for the penetrative nature of emitted energy through shadows, whereas the clouds themselves are darker for their low temperature.

Based on the knowledge that hue images are free of shadows (eg. Liu and McM. Moore, 1990), the RGB-IHS-RGB transformation has been used for suppression of cloud shadows from a Daedalus Airborne Thematic Mapper (ATM) data by Liu and McM. Moore (1993). The same method has been tested by the present work using Landsat TM data. In this approach a common band is subtracted from the three bands desired to make a composite, for band subtraction and ratioing are effective methods to suppress topographic shadows (Sabins, 1987). This operation is equivalent to shifting the spectral curves by a value of the subtrahend, and thus does not change the hue but increases the saturation and decreases the intensity (Liu and McM. Moore, 1993). The resulting images are then transformed to IHS-domain, after which the intensity image is replaced by TM band-6, followed by back- transformation to the RGB colour domain.

The above procedure was applied to the Odi subscene using bands 7, 4 and 1, and band 5 as subtrahend. Interestingly, the intensity image is cloud free whereas cast shadows are shown by darker pixels. Examination of the hue image shows that it is fairly free from shadow while the cloud has been suppressed. The saturation image is also shadow free. The resulting image, after substitution of the intensity image by TM-6 and retransformation to the RGB domain, however, shows only a limited improvement in suppressing the shadow effect. The difference in the sensor characteristics possibly accounts for the restricted applicability of the method to spacebome data as demonstrated by Liu and McM. Moore (1993).

A similar procedure conducted without the subtraction of a common band yielded a comparably similar result. Further attempts have been also made using PC transformation of all the TM bands. In the latter case the obtained result revealed that while PCI and PC2 mapped shadows as dark pixels, PC3 and PC4 are rather free from shadows. Replacement of the intensity and the saturation images by the latter two, respectively, followed by the back-transformation step yielded an improved result. The latter approach may also provide better results for airborne data.

4.4 Principal Component Analysis (PCA)

Principal Component (PC) transformation is a commonly used image processing technique in which a new coordinate system is calculated from a multispectral data set (eg. Sabins, 1987; Kaufmann, 1988). It is a multivariate statistical method used to compress multispectral data sets by removing redundancy in such a way that each successive linear combination (PC) has a smaller variance (eg. Rothery and Hunt, 1990; Gillespie *et al.,* 1986; Singh and Harrison, 1985; Crosta and McM. Moore, 1989). The other important feature of this method is that the PCs are scene dependent and totally uncorrelated (eg. Singh and Harrison, 1985; Gillespie *et al.,* 1986).

4.4.1 Unstandardized PCA (i/PCA)

Principal components are commonly calculated using the covariance matrix obtained from the input multispectral data whereby the corresponding eigenmatrices are also determined. This approach has been termed as "unstandardized PCA" by Singh and Harrison (1985) since the difference in variance of the input multispectral data strongly influences the resulting PCs. In the following sections different «PCs computed for the test site are discussed.

Six-bands wPCA

Using the six reflective TM bands an wPCA has been performed over the Odi subscene. Table 4.3 shows the covariance and eigenmatrices used for the transformation. As expected, wPCl, with 94.83% variance and positive loadings from all the TM bands, contains significant albedo and topographic information that often accounts for the high direct-correlations between the input bands. wPC2 appears to display better lithologic contrast, and topographic information is also present to a good extent. «PC3 and wPC4 display fair lithologic contrast, although the latter is too bright, possibly because of large input from TM-7 (Table 4.3), to show reasonable spectral contrast. On the other hand, wPC5 and uPC6 show more noise (in the form of striping) and appear to be less informative. A composite of wPC-1, 2 and 3 in R, G and B, respectively, has been found to provide the best lithologic discrimination with an overall better colour contrast. Histogram equalisation of this composite has improved the colour saturation, and yielded a more pleasing image.

Figure 4.2a shows the composite «PC-1, -2 and -3 in R, G and B, respectively, obtained for the Odi subscene. On this image basalt and basic plutons display a cyan colour in contrast to the meta-sediments that show more greenish colour. Undifferentiated sedimentary rocks appear poorly outlined, and likewise the contrast between basalt and gabbroids is low. Granites, sandstone, rhyolite, dacite and acidic metavolcanics of greenschist facies are difficult to discriminate, like on most raw-data composites. Graphite schists are shown in light green distinct from other metasediments, and similarly migmatized graphite gneiss and gneisses are also fairly distinct. Quaternary sediments are also differentiable. The image is generally less sharp, partly because of topographic shadows, and poor in contrast. The significant variance of «PCI, and less importantly by «PC2 (Table 4.3), accounts for the colour bias displayed by this image as magenta which consequently reduced hue contrast among the major rock types.

Table 4.3. Covariance matrix of the six reflective TM bands (a) used for unstandardized PCA, and the corresponding eigenmatrices (b), for the Odi subscene. Values rounded to the nearest decimal.

a)

TM	1	2	3	4	5	7
1	135.1					
2	103.3	82.6				
3	176.3	141.7	248.6			
4	152.8	123.9	217.8	199.6		
5	268.4	218.0	386.3	346.4	692.9	
7	167.4	135.7	240.2	213.6	436.9	288.7

b)

Eigen-vector	uPC 1	wPC 2	uPC3	«PC 4	i/PC5	«PC 6
TM-1	0.27	0.45	-0.59	-0.35	-0.44	-0.25
TM-2	0.22	0.30	-0.15	-0.01	0.14	0.90
TM-3	0.39	0.44	0.04	0.16	0.72	-0.34
TM-4	0.35	0.34	0.59	0.39	-0.52	-0.01
TM-5	0.66	-0.44	0.26	-0.55	0.03	0.02
TM-7	0.42	-0.45	-0.47	0.63	-0.07	-0.01
Eigen-value	1562	62.14	12-13	6.76	3.34	0.87
var.(%)	94.83	3.77	0.74	0.41	0.20	0.05

Similarly, using raw data of the four MSS bands an unstandardized PCA transformation has been conducted for the Odi subscene. As commonly the case is, the first component is dominated by albedo and topographic information through positive loadings from all bands. The second component exhibits relatively more spectral information, in addition to the distinction between VIS and SWIR bands as negative and positive values (Table 4.4), respectively, whereas the last two components predominantly contain noise. A composite of bands 4, 2 and 1 in R, G and B, respectively, yielded the best contrast among the major rock units, although no additional geologic information was obtained from this image. A similar processing procedure conducted using stretched data gave little improvement in colour saturation, whereas haze-corrected data produced no further enhancement. Table 4.4 shows the band covariances and the eigenmatrices used.

Table 4.4. Covariance matrix of the four MSS bands (a), and the corresponding eigenmatrices (b) used for unstandardised PC transformation for the Odi subscene.

a)

MSS	1	2	3	4
1	38.89			
2	64.30	112.38		
3	70.30	122.34	138.42	
4	53.91	94.87	107.72	87.16

b)

Eigen-vector	wPC1	wPC2	wPC3	wPC4
MSS-1	0.31	-0.52	-0.46	0.64
MSS-2	0.55	-0.49	0.65	-0.20
MSS-3	0.61	0.18	-0.55	-0.54
MSS-4	0.48	0.67	0.26	0.50
Eigen-value	368.74	5.31	1.48	1-32
var.(%)	97.85	1.41	0.39	0.35

Four-bands uPCA

Instead of the usually six input bands of the TM for PC transformation, four may be used whereby the fourth order PC is expected to be dominated by noise, while the first three make a colour composite. The advantage of this approach is that limited input bands believed to contain the necessary spectral information may be selectively used for the transformation in order to avoid data redundancy. Some of the highly correlated bands are generally omitted to this end.

Applying this approach to the Odi subscene bands 1, 4, 5 and 7 of the TM were selected for the wPCA transformation based on the fact that channel 5 is the least correlated band (Table 4.5) with the selected band triplet (Section 4.1.3). Individual study of the resulting images shows that «PC2 contains good spectral and morphologic information whereas «PCI is rather dominated by morphology, as expected. wPC3 and «PC4 appear primarily poor in spectral and morphological information, and contain noise in the form of grainy texture. This led to bands 4, 2 and 1 in R, G and B, respectively, as the best composite for lithologic differentiation.

On this image the distinction between the sandstone and acidic metavolcano-sediments, and between dacite and rhyolite appears good. On the other hand, undifferentiated metasediments, basalt and basic intrusives show a similar greenish colour, and unconsolidated Quaternary sediments are not discriminateable from sedimentary rocks. The image is spectrally similar to the uPCA composite (1,2 and 3 in R, G and B, respectively) obtained from the six input bands but with improved contrast. Reduction of the number of input bands helped in avoiding data redundancy in the PC images and thus better contrast. It is often the case that spectral contrast is frequently mapped by the 2nd PC and the other higher-order components are poorly informative in rock discrimination thereby giving less colour contrast on composite images.

A modification to the above approach operates with the first order PC which often contains about 95% variance and is known to map the correlative topographic and albedo information. According to

Kaufmann (1988) this component is better avoided from PC-composites in order not to convolve and confuse the spectral information. Omission of PCI from such colour composites, however, means the loss of topographic information which is important for geologic image interpretation. A good alternative would, therefore, be to multiply PCI with other three PCs and scale the result back to the allowed dynamic range such that the other PCs are also comprised of topographic information (see also Crippen, 1988).

For the study area the above described method was applied to the four-band PCA images (Figure 4.2b). Individual study of the obtained images shows that they have commonly retained good spectral contrast where the bright and dark areas remained the same as in the original images. More significant improvement, however, was obtained by convolving topographic information in all the modified images as compared to their original equivalents. This resulted in a more interpretable image for both lithologic and structural features, since these information are also contained by the high order PCs, permitting a greater number of comparably good composite images. The PCs appear to yield aesthetically more pleasing composite in the order PC2, PC3 and PC4 in R, G and B, respectively (Figure 4.2b).

On this composite improved distinction was obtained between the similar-looking rocks such as granites, sandstone and dominantly acidic metavolcano-sedimentary rocks, basalt and graphite schists, dacite and rhyolite, and also graphite gneiss. Furthermore, undifferentiated sedimentary rocks are very distinctive by their bluish colour unlike on the six-band PC image (Figure 4.2a). The meta-sediments look fairly different from graphite schist. On the other hand, distinction between gabbroic rocks and basalt remained poor. Quartzite-amphibole bands are less distinct on this image. In general, the modified 4-band PCA yielded an improved geologic information for the test site, as compared to the previously described PCA methods.

Three-bands i/PCA

Unstandardized PCA was also conducted using raw data of the best band-triplet (1 4 7) selected for the study area. The resulting image gave no major improvements over the composite 1, 2 and 3 in R, G and B, respectively, of the six-band uPCA. This may be attributed to the reduced number of dimensions from the input data, which further restrict the effect of data compression in PCA when there are less than four bands. Application of the same method to stretched data yielded no further improvement in lithologic discrimination with the exception of minor enrichments in colour saturation. The three-band PCA has shown that for three input bands (that are needed for a colour composite) PC transformation yields hardly enhanced images, since the third component is chiefly constituted by noise. At least four bands are thus required to benefit from such operations.

4.4.2 Standardized PCA (sPCA)

Singh and Harrison (1985) demonstrated the use of correlation coefficients, instead of covariance matrices, in PC transformations. Correlation coefficients can be obtained by dividing the covariances of the band-pairs under consideration by the product of their standard deviations (Davis, 1986). Through the standardisation process the input bands will have equal weight thereby avoiding the bias introduced through the difference in variance (Singh and Harrison, 1985).

Standardized PCs were obtained for the area of interest using the six reflective TM bands following the above steps. Individual study of the sPCs has shown that sPC5 provides the best lithologic contrast and significant morphological information, being consecutively followed by sPC6 and sPC2. The remaining components, despite the preserved topographic expression, appeared to be less informative in the present context. The relatively high positive loadings from SWIR bands possibly account for the bright-look of sPC2. sPC4 appears to display very good

structural features and drainage patterns, and the existing little vegetation is certainly mapped by sPC3 with additional positive inputs from other features in TM band 4. These observations gave rise to the composite 2, 5 and 6 in R, G and B, respectively, as the best sPC-triplet to display the various lithologic units and structural information (Figure 4.2c). Overlooking the effect of vegetation (TM band 4), this composite consists of components dominated by bands from VIS, NIR and SWIR regions; for sPC6, sPC5 and sPC2 are largely loaded by TM bands 2, 5 and 7, respectively (Table 4.4), in agreement with features observed in section 4.1.3. Table 4.5 indicates the correlation-coefficient matrix and the corresponding eigenmatrices, and Figure 4.2c shows the obtained image.

On this composite sandstone, dacite, basic plutons, and granites appear very well discernable among themselves and also against the similar looking units of basalt, metasediments and graphitic schists. Undifferentiated sedimentary rocks, gneisses, quartzite and graphite gneisses also appear distinct. Metavolcano-sediments of amphibolite facies are fairly separable from those of greenschist facies. As compared to the wPCA image this composite provides significant spectral enhancement without mixing spectral signatures of rocks with shadows, and along with clear morphologic expression (Figure 4.2c). The image by and large yielded an improved enhancement than all the results obtained by the PC transformations.

Table 4.5. Correlation coefficients of the six reflective TM bands (a), and the corresponding eigenmatrices (b), used for standardized PC transformation of the Odi subscene.

a)

TM	1	2	3	4	5	7
1	1.00					
2	0.98	1.00				
3	0.96	0.99	1.00			
4	0.93	0.97	0.93	1.00		
5	0.88	0.91	0.93	0.93	1.00	
7	0.85	0.88	0.90	0.89	0.98	1.00

b)

Eigen-vector	sPC 1	sPC 2	sPC 3	$PC 4	.sPC 5	sPC 7
TM-1	0.40	-0.44	-0.60	-0.47	-0.16	0.19
TM-2	0.41	-0.32	-0.08	0.41	0.18	-0.72
TM-3	0.42	-0.21	0.19	0.49	0.27	0.66
TM-4	0.41	-0.13	0.71	-0.32	-0.45	-0.08
TM-5	0.41	0.48	0.06	-0.43	0.64	-0.07
TM-7	0.40	0.64	-0.30	0.30	-0.50	0.02
Eigen-value	5.65	0.24	0.07	0.02	0.02	0.01
var.(%)	94.14	4.06	1.10	0.31	0.26	0.13

Table 4.6. Correlation coefficients of the four MSS bands (a), and the corresponding eigenmatrices (b), used for standardized PC transformation of the Odi subscene.

a)

MSS	1	2	3	4
1	1.00			
2	0.97	1.00		
3	0.96	0.98	1.00	
4	0.93	0.96	0.98	1.00

b)

Eigen-vector	sPC1	sPC2	sPC3	jPC4
MSS-1	0.50	-0.70	-0.50	-0.10
MSS-2	0.50	-0.16	0.79	-0.30
MSS-3	0.50	0.21	0.04	0.84
MSS-4	0.50	0.66	-0.35	-0.45
Eigen-value	3.89	0.07	0.02	0.01
var. (%)	97.25	1.86	0.56	0.33

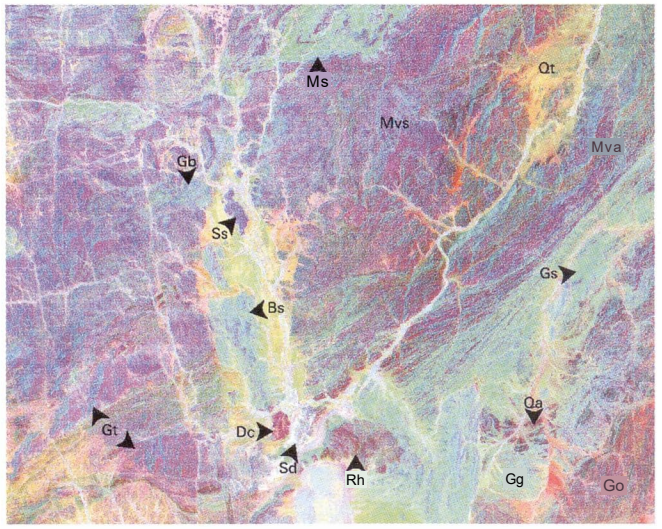

a) uPCA composite (1, 2 & 3 in R, G & B, respectively) obtained for the Odi sub-scene using the six reflective TM bands.

c) sPCA composite (2, 5 & 6 in R, G & B, respectively) obtained for the Odi sub-scene using the six reflective bands of the TM.

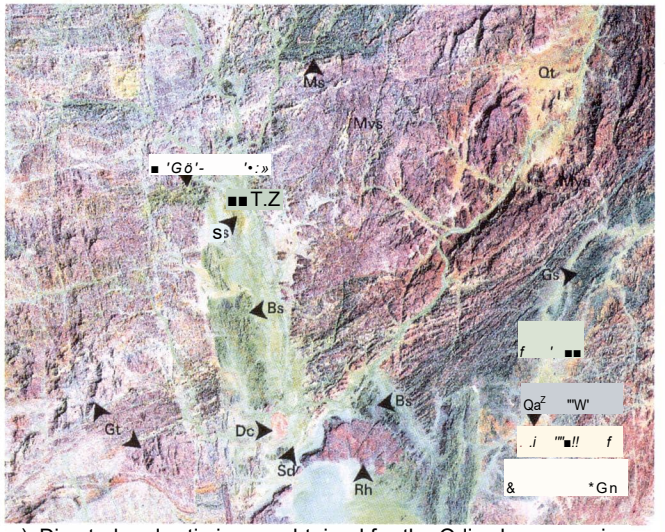

e) Directe band ratio image obtained for the Odi sub-scene using ratios 7/5, 5/4 & 3/1 in R, G & B, respectively.

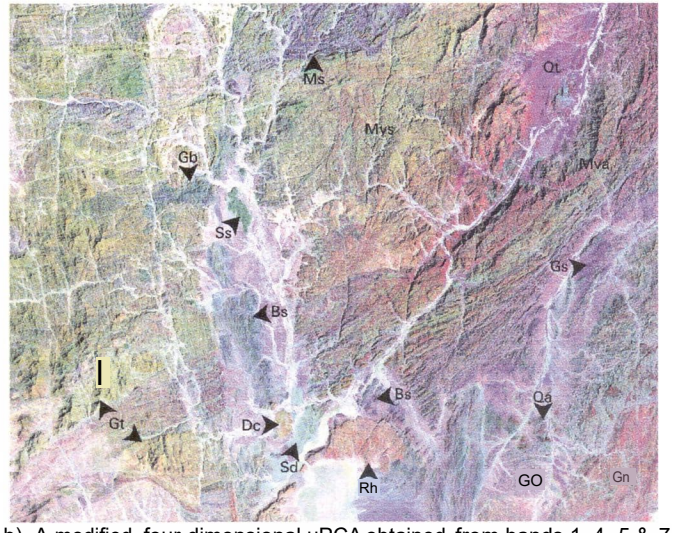

b) A modified four-dimensional uPCA obtained from bands 1, 4, 5 & 7 by convolving PC1 with PC2, PC3 & PC4 (in R, G & B, respectively).

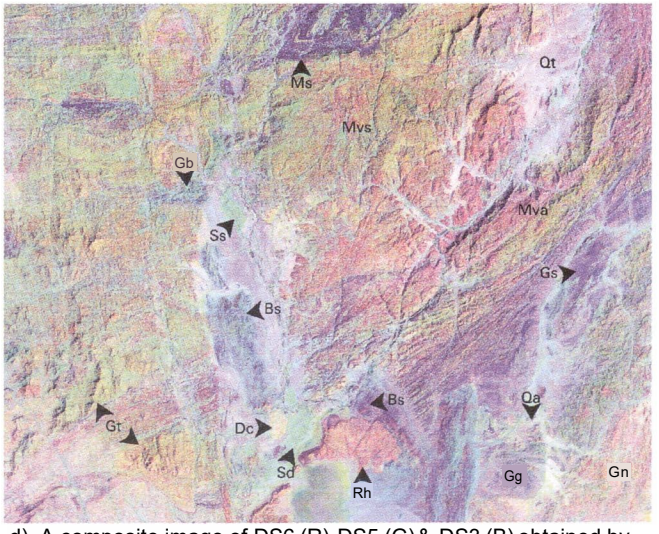

d) A composite image of DS6 (R), DS5 (G) & DS3 (B) obtained by decorrelation stretching of uPCA using the six reflective TM bands.

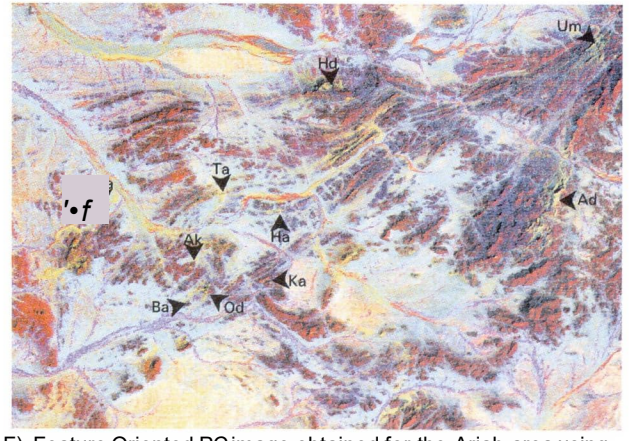

F) Feature Oriented PC image obtained for the Ariab area using bands 1, 3, 4 & 7 and, 1, 4, 5 & 7 for "iron-oxide" and "hydroxyl" mapping. Yellowish areas of exposed rocks indicate gossan bodies as alteration markers for sulphide and gold mineralisations. Block size 52.62 x 36.72 km. For key to locality names see Figure 4.6.

Figure 4.2. Some results of the different image processing algorithms applied for spectral enhancement of the Odi sub-scene using Landsat TM data. For a, b, c, d & e block size is 76.8 x 61.44 km. Rock types: Qt=Quaternary sediments, Dc=dacite, Rh=rhyolite. Bs=basalt, Ss=sandstone, Sd=undiff. sedimentary rocks, Gt=granite, Gb=gabbroid, Ms=metasediments, Mvs= metavocano-sediments (greenschist facies), Mva=metavolcano-sediments (amphibolite facies), Gs=graphite schist. Gg=graphite gneiss, Qa=quartzite & amphibolite, and Gn=gneisses.
See text for explanation.

For the Odi subscene a standardized PCA transformation was also computed using the MSS data. Individual study of the obtained images shows that the first PC has mapped topographic and albedo information, as often the case is, through an equal loading from all MSS bands (Table 4.6). The second component, being dominated by inputs from the least correlated MSS bands 1 and 4 (see below), displays the best spectral contrast among the major rock units. Unlike their unstandardized equivalents the 3rd and the 4th components, being dominated by inputs from MSS bands 2 and 3, respectively, are much less influenced by noise and appear to contain more spectral information. Although no additional geologic information has bee obtained the band composite 2, 3 and 4 in R, G and B, respectively, gave an improved lithologic contrast for the study area unlike the unstandardized transformation.

Comparison of t/PCA and sPCA

In case of the Landsat TM data the first three components in z/PCA account for over 99% of the total variance whereas the first five components are needed to achieve the same amount of compression in sPCA (compare Tables 4.3b and 4.5b). In the former case PCI is positively loaded by all TM bands whose contribution in a decreasing order follows the sequence 5, 7, 3, 4, 1 and 2; a trend that pursues their decreasing variance (standard deviation as a representation of variance, Table 4.2b). On the other hand, in case of the standardized trans-formation the input bands are more or less uniformly weighted in the first PC. Interestingly, bands 5 and 7, which are also moderately correlated (Table 4.5a), are the ones having the maximum loadings in sPC2, and not in sPC1 where the least correlated bands 1, 4, and 7 relatively contribute the minimum. TM bands 5 and 7 are rather dominant in z/PCl (Table 4.3b) for their obviously high variances. Figure 4.3 shows a graphical representation of the eigenvector loadings in both transformation types for Landsat TM and MSS data.

In both approaches the difference between VIS/NIR and SWIR bands is depicted as dark and bright pixels in PC2; that is bands 1 to 4 of the TM are in contrasting mode with bands 5 and 7 (Figure 4.3b). The variance contained in sPC2 is greater than that of z/PC2 (compare Tables 4.3b and 4.5b, or see Figure 4.3b) making it more informative, as also supported by visual inspection (also Kenea and Heanisch, 1996). sPC6 mapped TM band 2 in dark pixels, whereas band 2 is predominant in wPC6 as bright pixels overshadowed by noise. Similarly, sPC5 displays a rather good lithologic contrast unlike their unstandardized equivalents where they are overwhelmingly noisy. The significant inputs from TM bands 5 and 7 in to sPC5 may explain this effect as these bands are important to display lithologic contrasts (eg. Crippen, 1989) unlike in wPC5 (Figure 4.3e). And TM bands 3, 4 and 5 apparently dictated the improvements in sPC6 in contrast to that of z/PC6 (Figure 4.3f). Comparison of the composites sPC2, 5 and 6 (Figure 4.2c), and wPCl, 2 and 3 (Figure 4.2a) in R, G and B, respectively, shows a remarkable enhancement of geologic information in the former over the latter.

Ready and Wintz (1973) demonstrated that noise in multispectral data set appears as additive term to the eigenvalues during PC transformations using covariance matrices. Singh and Harrison (1985) illustrated that random noise is not uniformly distributed in multispectral data, and it varies among others with spectral bandwidth and sensitivity to the atmosphere. The eigenvectors computed using standardized variables are, however, equally sensitive to all spectral bands irrespective of the distribution of variance or signal-to-noise ratio (SNR) in the original data and provide a set of unbiased eigenvalues (Singh and Harrison, 1985).

The above demonstrated overall visual enhancement is also corroborated by the improved signal-to-noise ratio (SNR) obtained. Following Ready and Wintz (1973) SNR can be determined as the ratio of the first eigenvalue over the maximum covariance (also Singh and Harrison, 1985). Accordingly, using the covariance matrix (Table 4.3a), SNR = 1562/693 = 3.53 dB;

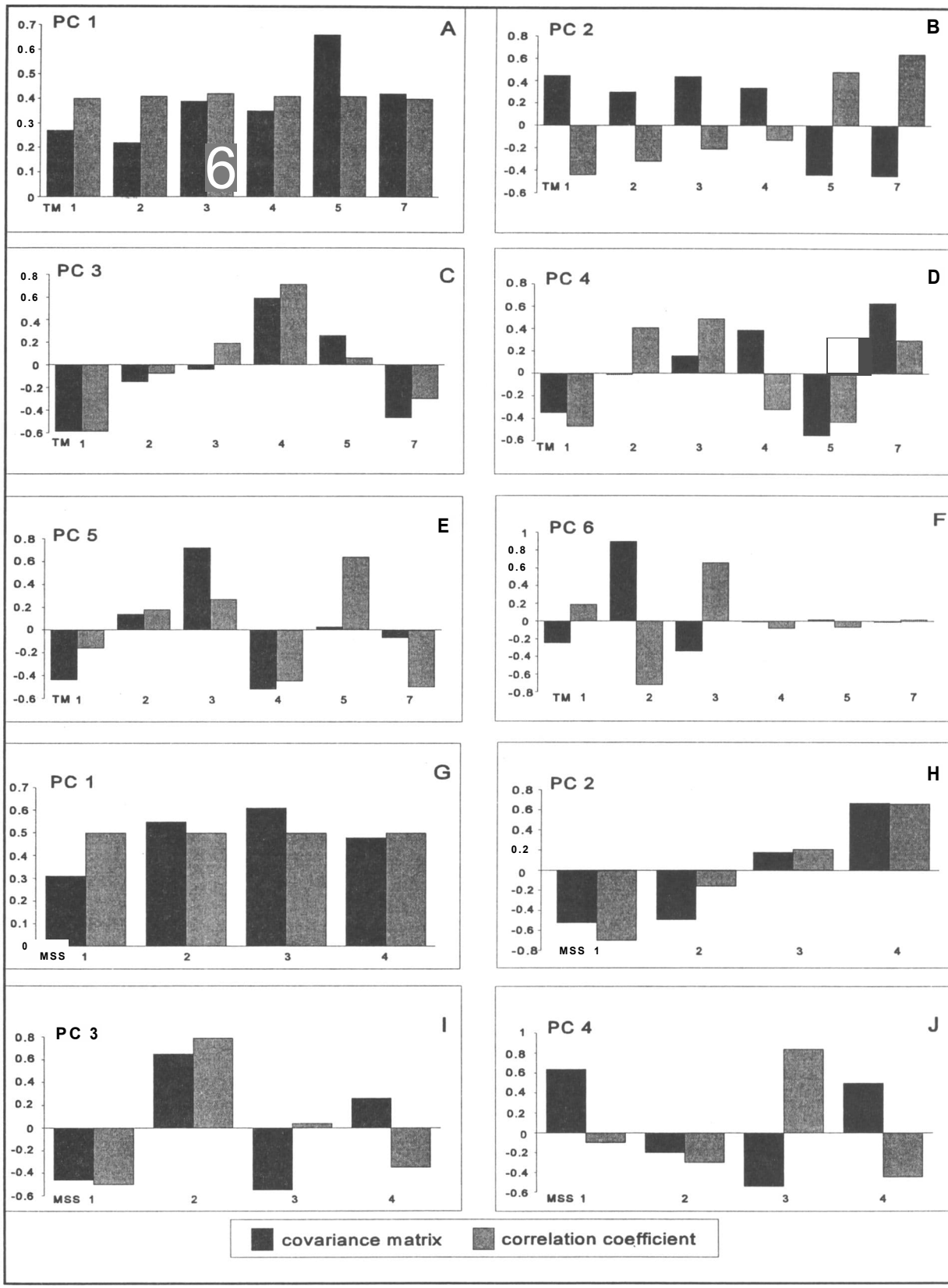

Figure 4.3. A graphical representation of eigenvector loadings (vertical axes) of TM (Figures a - f) and MSS (Figures g - j) bands in PC transformations using covariance matrices (uPCA) and correlation coefficients (jPCA).

whereas using correlation-coefficient matrix (Table 4.5a), SNR = 5.65/1.0 = **7.52** dB.

The difference (7.52-3.53) of 3.99 dB in SNR illustrates the obtained enhancement by using the correlation coefficient instead of covariance matrix (see also Kenea and Heanisch, 1996).

A similar comparison made for MSS data also depicts significant improvement obtained through standardized transformation. For the standardized PCA, PCI is equally loaded by all bands unlike its unstandardized equivalent which has inputs from bands 3, 2, 4 and 1 in a decreasing order following their variances (Table 4.4 and 4.6), analogous to TM data. With a variance of 1.86%, the sPC2 appears to show some improvement over its unstandardized equivalent that has a variance of about 1.41%. Interestingly, both PC2s exhibit the difference between the visible and reflected infrared parts of the spectrum as dark and bright pixels, respectively, and are invariably dominated by loadings from the least correlated MSS bands 1 and 4 (see Figure 4.3h, or compare Tables 4.4 and 4.6). Similarly, improvement of sPC3 over wPC3 is depicted by the variance load in these components as 0.56% and 0.39%, respectively. .vPC4 is dominated by positive loading from MSS band 3 unlike «PC4 which has a negative input form the same band. These features explain the reason for which composites involving sPC2, .vPC3 and sPC4 give better results for visual discrimination of the different rock types.

Computation of SNR for the MSS data following the above procedure also corroborates the obtained visual improvement. For the wPCA transformation (Table 4.4a),

SNR = 368.74/138.42 = **4.25** dB; whereas for the sPCA (Table 4.6a), SNR = 3.89/1.0 = **5.89** dB.

A difference of **1.64** dB **(5.89-4.25)** reveals the obtained enhancement by using standardized transformation. The result also testifies that the visual improvement in SNR obtained by using standardized transformation over MSS data is much inferior than that obtained from TM data.

4.4.3 PC Decorrelation stretching (DS)

It has been stated that in PC transformation new statistically independent axes are calculated from the input data set (Section 4.4). In order to conduct decorrelation stretching, also known as inverted PCA (Williams, 1983), the obtained PC images are stretched and then transformed back to the original axes (eg. Gillespie *et al.,* 1986), using the transpose of the eigenmatrix (see also Rothery and Hunt, 1990). As an effect the resulting images are chromatically enhanced and decorrelated thereby being more interpretable than the original PCs (Rothery and Hunt, 1990; Gillespie *et al.,* 1986) in addition to subduing the "noise" inherent in the higher order PCs (Williams, 1983).

Six-bands DS

Following the above described method decorrelation stretching was conducted for the Odi area using the unstandardized PCs obtained from the six reflective bands of the TM. In this exercise all «PCs were "forced" to an equal mean and standard deviation through linear stretching (with DN values around 127 and 42, respectively) in order to achieve unbiased colour enhancement (Section 4.2).

Observation of the individual images revealed that DS2 contains much noise for incorporation of significant load (0.90) from wPC6 which is predominantly noisy (Section 4.4.1). While DS1 is of inferior quality for a similar reason of noise incorporation from PC5, DS4 also appears geologically less informative. Unlike the high order PC images that often are saturated by noise (Section 4.4.1) DS5 and DS6 appear to provide a very good lithologic contrast and topographic information. For this particular example this is attributed to the very low inputs from »PC5 and wPC6, and the rather high loadings from the low order «PCs which are less affected by noise (Section 4.4.1). This gave the DS composite 6, 5

and 3 in R, G and B, respectively, as the best triplet in displaying geological features (Figure 4.2d).

An interesting feature clearly displayed only on this composite is that basaltic layers N and S of the Tashalal-Langeb transfer fault (Figure 4.1) exhibit distinct colours possibly attributed to chemical differences between different flows (Kenea, 1997). Furthermore, rhyolite and dacite appear very distinct in contrast to most images obtained from the other enhancement methods conducted. Sandstone is also exceptionally distinct from other acidic rocks with its greenish colour, unlike that obtained by «PCA. Other rock units such as undifferentiated meta-sediments and graphite schist, migmatized graphite gneiss and graphite schist, and granites and metavolcano-sediments (greenschist facies) are also more dissimilar on this aesthetically pleasing image (Figure 4.2d).

The above result could be improved by slightly modifying the computation, whereby the coefficients of those «PCs with significant noise is set to zero during retransformation (see also Rothery and Hunt, 1990). For the area of interest coefficients of »PC5 and «PC6 were set to zero for application of this approach. Individual inspection of the obtained images shows remarkable improvements in components DS2 and DS3 where high loadings from »PC5 and «PC6 (large inputs from TM band 3 and TM band 2, respectively) were omitted. From the obtained result most composites gave images with good geologic contrast but the composite 6, 5 and 2 (3) in R, G and B, respectively, appears to be more enhanced.

On this image graphitic schists, other meta-sediments, rhyolite, dacite and undifferentiated sedimentary rocks appear distinct. Amphibolite facies metavolcano-sediments are also separable from the greenschist facies rocks although the distinction between basalt and gabbroid looks difficult.

Four-bands DS

As it has been demonstrated in section 4.4.1 improved result can be obtained if only four selected TM bands are used for PC transformation, instead of six. In DS of such images the coefficients of the PCs having maximum noise are set to zero during retransformation. The advantage of this technique is that there is a possibility to omit bands in which image data are redundant (sec. 4.4.1). To apply this approach to the study area TM bands 1, 4, 5 and 7 were initially selected. TM band 5 has been chosen for similar reasons given in section 4.4.1 .

After PC transformation of the selected four input bands, the coefficients of «PC4 were set to zero during retransformation, since this component apparently contains the maximum noise, following visual inspection. The result shows that DS2 is poorly distinct, with all the eigenvectors mapped as positive loadings thereby giving a much brighter image (see Table 4.3b). This gave DS4, DS3 and DS1 in R, G and B, respectively, to be the best composite showing substantial geologic information. Though additional geologic information has not been obtained in this particular case the result is well comparable to those obtained from six-band DS, but with no less improvements in hue. A similar processing attempted using stretched data produced an image of inferior quality, because of the already saturated grey value range that hardly changed after PC transformation.

Three-bands DS

PC decorrelation stretching has also been conducted for the best band-triplet (7,4,1) selected for Odi the area (Section 4.1.3). The result appears to be a composite image with a colour saturation slightly better than the one obtained from six input bands. This is thought to be related to the poorly correlated nature of the input bands and the data compression taking place during PC transformation which attains a total variance of 100% only when three input bands are used. An image obtained from stretched data input gave no improvements over the unstretched data for similar reason given above. Its improvement over PC images obtained for three input bands is attributed to the rotation effect of the PC axes during

decorrelation thereby permitting interpretable hue distribution (Gillespie *et al.,* 1996).

DS of MSS data

Using the PC images obtained from unstandardized transformation, decorrelation stretching was also computed for the MSS data. DS4, among others, shows better spectral contrast between the major rock units and appears to have preserved fair topographic information for its high-to-moderate loadings from »PC2 and wPCl (Table 4.4b) that are free from noise. DS2 and DS3 images are generally noisy and appear to contain less information, by and large as an effect of significant loadings from the 3rd and 4th component that are chiefly noisy. DS1 apparently shows slight improvement. Accordingly the composite DS4, DS3 and DS1 in R, G and B, respectively, provided the best lithologic contrast for the Odi area. On this image discrimination of major rock types such as granite, metasediments, basalt, and metavolcano-sediments can be made while units such as graphite schist and metasediments remain indiscriminateable.

Decorrelation stretching of sPCA

Decorrelation stretching of six-bands sPCA was attempted to evaluate the effect of the standard-isation process on PC decorrelation. The resulting decorrelated images appear generally similar to those obtained from the unstandardized data except that in the standardized case there is no single image overshadowed by noise. DS1 looks very poor in displaying lithologic contrast whereas DS2 is too bright to show the same. DS6 exhibits prevalent noise. The composite image DS5, DS4 and DS3 in R, G and B, respectively, gives the best composite for visual discrimination of the rock units in the area. On this image distinctions between basalt, metasediments and graphitic schists/gneisses, rhyolite, sandstone and dacite, and quartzo-feldspathic schists and ferruginous quartzite appear very explicit. Granites and basic plutons look rather indiscriminateable.

A similar computation of decorrelation stretching of standardized PCA obtained from MSS data yielded no special improvement. Individual images appear more noisy and exhibit poor spectral contrast. The composite DS4, DS2 and DS1 in R, G and B, respectively, gave a better result, though with no remarkable improvement over the same composite before decorrelation stretching. The method, thus, proved less useful for visual lithologic enhancement.

4.5 Band Ratios

Band ratio technique is a well established method of image enhancement in geologic remote sensing. In this approach the grey values in one (or more) band(s) are divided by the corresponding values in other band(s), thereby specifically enhancing objects having contrasting spectral responses in the numerator and denominator band(s). A major advantage of ratio images is that they convey the spectral or colour characteristics of image features, regardless of variations in illumination conditions. Subtle spectral differences that are masked by scene brightness variations are enhanced in ratio images due to the fact that such operations portray the variation in slopes of spectral reflectance curves between the bands involved, irrespective of the absolute values (Lillesand and Kiefer, 1994). One of the other characteristics of band ratioing is its data "compressive" nature, whereby more than two bands or band combinations may be used in the operation. Band ratio images are obviously less correlated than the original bands (eg. Gillespie *et al.,* 1987) and therefore chromatically enhanced, the fact that made the technique commonly applicable in many exploration studies.

4.5.1 Band selection

Statistical methods (Section 4.1.3) have been developed to assist band selection for ratioing (Sheffield, 1985; Crippen, 1989). A limitation to such procedure is that the best combination for conveying the overall information in a scene may

not be the best combination for conveying the specific information desired for that particular case (also Lillesand and Kieffer, 1994). In order to produce ratios in which the spectral features of various rock types are enhanced selection of particular bands is better based on the knowledge of spectral characteristics of minerals influencing reflectance of different rocks.

Considering the generally known spectral characteristics of minerals and rocks (Section 3.4), carbonates, hydroxylated silicates like clays, chlorites and serpentine are known to display strong absorption in TM band 7. Iron (ferrous) rich minerals are also known to have absorption band in TM band 1 and higher reflectance in TM band 3, whereas ferric-oxides (eg. hematite) and hydroxides display absorption in TM band 4 (Hunt *et al.,* 1971). TM band 5 generally records high reflectance for most objects. Based on the above considerations band ratios 7/5, 5/4 and 3/1 in R, G and B, respectively, were selected for this study. Band ratio 5/7 suggested by Crippen (1989) and also applied by Kaufmann (1988) were not selected in order to avoid the overall high reflectance in TM band 5 that could result in data over-flow in such an arid area at moderately high sun-elevation.

4.5.2 Adjusted and unadjusted band ratios

Band ratioing may be conducted on raw data where no correction for atmospheric path radiance is made, also called "unadjusted band ratio" (Crippen *et al.,* 1988). The resulting image would contain some topographic and albedo information but generally at the expense of spectral features (Gillespie *et al.,* 1987). In order to enhance the spectral information, atmospheric path radiance should be removed from the bands involved in the ratioing (also termed "adjusted ratio") by one of the known methods for haze correction (Section 4.1.2) (eg. Crane, 1971; Crippen, 1989) before band ratioing. One drawback, however, is that the resulting image would be devoid of topographic information that are often critically important for geologic interpretation.

The above selected band ratios were obtained for the area of interest using both unadjusted and adjusted data. Inspection of individual ratio images obtained from the former data type shows that band ratio 7/5 contains no topographic information because these bands are almost unaffected by path radiance or have low additive terms (Section 4.1.2) whereas ratio 3/1 appears to contain significant albedo and topographic data.

On this composite topographic expression is fairly preserved and units like basalt, metasediments, and gabbroic rocks are in similar magenta colour. The rhyolite, dacite, granite and gneisses are in greenish-yellow, and indiscriminateable. The sandstone displays a light yellow hue. This composite is generally poor in containing spectral information that may be used for lithologic discrimination; most units apparently exhibit close spectral ranges. This may as well be attributed to the fact that ratio images are "intensity blind", i.e. rocks having different absolute radiance but similar slopes of spectral reflectance curves appear identical on these images.

For the same input bands the ratio images obtained from adjusted data appear to be enhanced in terms of colour saturation but devoid of topographic and albedo information, making geological interpretation difficult. Proper location of geological features appears to some extent erroneous on these images. Furthermore, the image contains some noise introduced as scan-line striping, due to the enhancement of uncorrelated features in the component images during the ratioing (Lillesand and Kiefer, 1994).

An attempt has also been made to combine the spectrally enhance adjusted band-ratio images and the unadjusted band-ratio images rich in albedo and topographic information. In this approach the two images have been averaged and then linearly scaled. The obtained result appears to provide a spectrally and topographically enhanced image than the individual input ratio images. Other band-ratio composites like 5/7, 5/4 and 3/1 known as general "mineral composite", and the "hydrothermal composite" 5/7, 3/1 and 4/3 (ERDAS, 1982-1994) were also attempted for the Odi area. The results obtained are hardly different

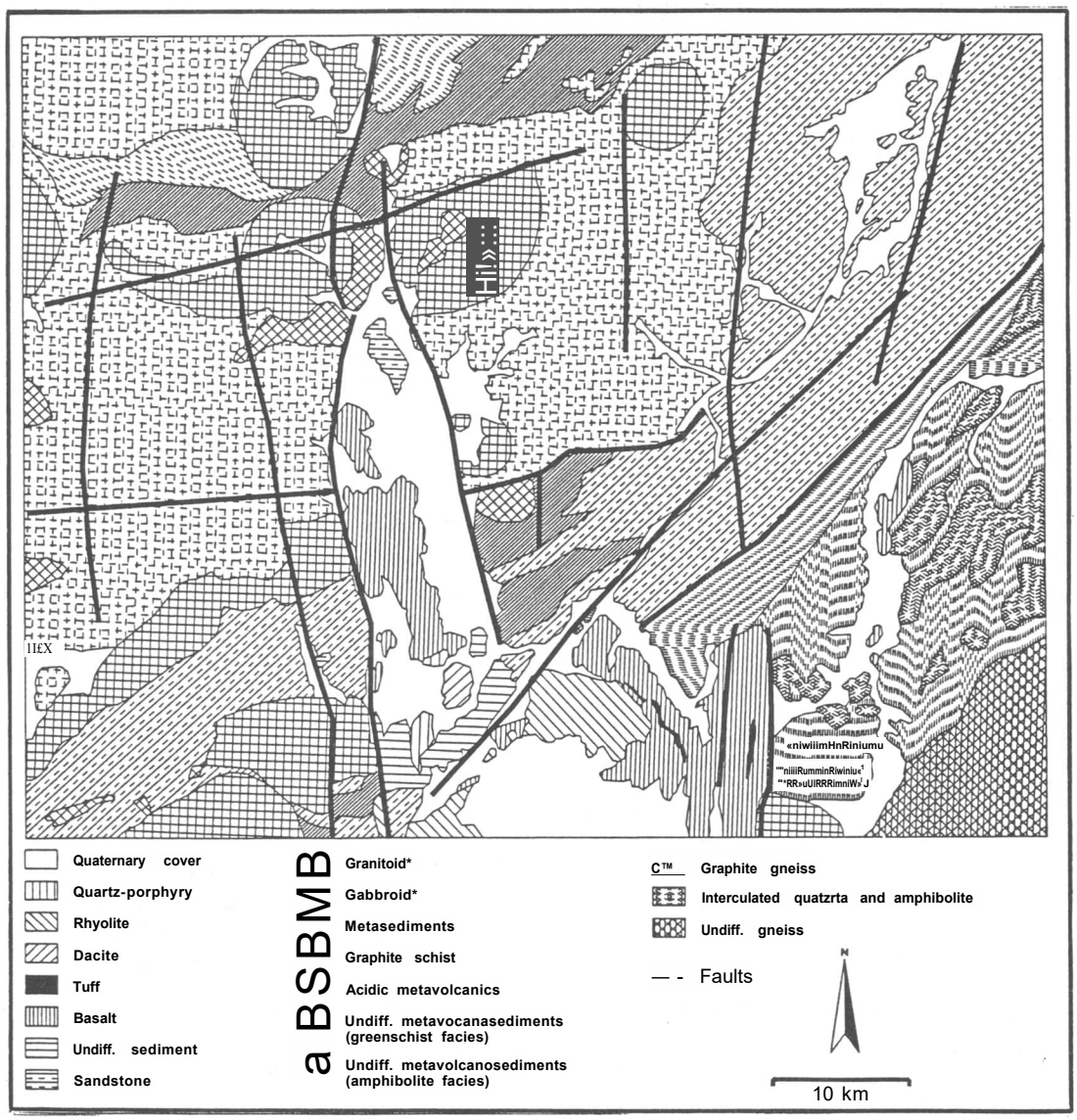

Figure 4.4. A geological interpretation map of the Odi subscene. Area corresponds to Figures 4.1a-e.

from that of the above described ratio in context of lithologic mapping.

4.5.3 Directed band ratios

As it has been demonstrated above, ratio images obtained from unadjusted data are generally poor in spectral contrast whereas those from adjusted data are devoid of topographic and albedo information that are often important for image interpretation since different geologic processes are expressed in various geomorphic forms. To exploit the advantages from both approaches Crippen *et al.* (1988) developed a valuable method known as "directed band ratio".

The method consists of initial haze correction, histogram inspection of ratio images followed by multiplication of the denominator bands by a constant, addition of a constant to all the bands in

the ratio, and finally band ratioing. The additive and multiplicative terms determine the extent to which topography is retained in the ratio images. More detailed explanations and the theoretical backgrounds are given in Crippen *et al.* (1988).

For the Odi subscene directed band ratioing was conducted using bands 3/1, 5/4 and 5/7 in R G and B, respectively. After several attempts an additive term of 55, and multiplicative constants of 0.9, 0.85 and 0.8 for TM bands 1, 4 and 7, respectively, were found to provide the best chromatically enhanced image for the area. The image is obviously well enhanced as compared to the other ratio methods in displaying both morphological features and colour saturations, but introduced no additional information to the geologic interpretation of the area. Figure 4.1e shows the obtained image.

On this image metasediments and graphitic schist are in greenish blue colour for high 5/7 ratio caused by carbonates and hydroxylated silicates. It is well distinct from the light-green coloured basalts that have significant absorption in TM-4 (NIR) by ferric iron which also partly off-sets the reflectance in TM-1 (Hunt *et al.,* 1971, 1974). The yellowish colour of sandstone is may be attributed to iron-oxides that have significant absorption bands in both TM-1 and TM-4. A similar reason explains the reddish yellow colour of the quartzite-amphibole bands. Rocks like quartzofeldspathic gneisses, dacite and most acidic metavolcano-sediments that are rich in tectosilicates (quartz and feldspar) appear in reddish hue for their overall high reflectance in SWIR despite the possible presence of water in low temperature minerals.

4.5.4 Chromaticity and band difference

Chromaticity transformation

The concept of chromaticity transformation has been illustrated by Gillespie *et al.* (1987). The method involves ratioing of the individual input bands by the intensity. It is computed as; r=R/(R+G+B), g= G/(R+G+B) and b=B/(R+G+B), where R, G and B are the original grey values of the input bands and r, g and b represent the chromaticity coordinates.

Following the above operations chromaticity images were determined for the Odi area using bands 1, 4 and 7 of the TM. The obtained images, however, appear to be of no significance for geological interpretation. Most lithologic units that are discriminateable on the composite of the input bands appear poorly enhanced. This is possibly ascribed to the least correlated nature of the input bands, as the method is helpful for highly correlated data (Gillespie *et al.,* 1987).

Band difference

Despite their decorrelated nature ratio images at times fail to display significant lithologic contrasts. This is partly because the contrast stretching which must be applied to the resulting output image is a linear operation unlike the ratioing itself which is non-linear (see also Crosta and McM. Moore, 1989). As a result of this inconsistency subtle spectral information in ratio images are often subdued. However, band differencing is a linear operation that, if followed by linear contrast stretching, may yield images with improved spectral contrasts. Furthermore, the existing topographic information are always retained in difference images unlike adjusted band ratios.

For the study area band difference images were produced using TM bands 5-7, 5-4 and 3-1 in R, G and B, respectively. In order to avoid the colour bias to be introduced from bands having larger variance and mean values a stretched data has been used (Section 4.2). The obtained image is chromatically enhanced as compared to both adjusted and unadjusted ratio images, but with no remarkable additional information.

Normalized band difference was also computed by dividing the band difference with the intensities of the respective bands (Gillespie *et al.,* 1987). This process is expected to reduce the effect of albedo, in the visible and near-infrared parts of the spectrum, and topography on the normalized image. The images were obtained for the area of interest using the bands (5-7)/(5+7), (5-4)/(5+4) and (3- 1)/(3+1) in R, G and B, respectively. In this composite image

topographic information are generally preserved, however rock discrimination appears difficult except for the sandstone, rhyolite, metasediments and basalts.

4.6 Spatial Enhancements

In contrast to spectral image enhancements discussed above, spatial filters emphasise or de-emphasise image data of various spatial frequencies that refer to the "roughness" of the tonal variation (Lillesand and Kiefer, 1994). Image areas of high spatial frequency are tonally "rough", emphasising local details in grey value variations, whereas those with low spatial frequency pronounce brightness changes in large areas and they are tonally "smooth". The process involves matrix operations where the spatial distribution of the pixel (neighbourhood influence) and the moving window size play an influential role. Filters that operate in the frequency domain are implemented through the Fourier transformation, whereas those which operate in the spatial domain of the image itself are known as Convolution filters (eg. List, 1993).

4.6.1 Convolution filtering

In order to facilitate visual interpretation of the Landsat data different convolution filters of variable window size were applied.

For the purpose of lithologic discrimination it has been found that mid-low filter of 3x3 window provides the best improvements. The values in the filter matrix are multiplied by the corresponding pixel grey value in the image, and the sum of these products is multiplied by the kernel's coefficient to give the new value to the central pixel in the image. This operation has been often useful following an image enhancement whose output has been scaled, and thereby yielded relatively brighter image due to saturation of the higher grey values. It has also proven helpful for alteration mapping using PC transformation by permitting the omission of undesired objects whose size is less than 100x100 m^2 (Section 4.7).

Mid-low filter

-1	-1	-1
-1	16	-1
-1	-1	-1

Northwest

1	1	1	1	1	1	1
1	1	1	1	1	1	-1
1	1	1	1	1	-1	-1
1	1	1	-2	-1	-1	-1
1	1	1	-1	-1	-1	-1
1	1	-1	-1	-1	-1	-1
1	-1	-1	-1	-1	-1	-1

Northeast

1	1	1	1	1	1	1
-1	1	1	1	1	1	1
-1	-1	1	1	1	1	1
-1	-1	-1	-2	1	1	1
-1	-1	-1	-1	1	1	1
-1	-1	-1	-1	-1	-1	1
-1	-1	-1	-1	-1	-1	-1

For the purpose of lineament analyses spatial enhancements were performed using non-directional and directional filters. It has been found out that directional filters provide better enhancement of linear features than the non-directional ones. In view of this, three directional filters were selected to also facilitate a colour composite. The chosen directions were W, NW and NE while the window size has been kept 7x7 for the whole map area, such that large lineaments are preferably enhanced.

West

1	1	1	1	-1	-1	-1
1	1	1	1	-1	-1	-1
1	1	1	1	-1	-1	-1
1	1	1	-2	-1	-1	-1
1	1	1	1	-1	-1	-1
1	1	1	1	-1	-1	-1
1	1	1	1	-1	-1	-1

On the resulting composite image displacements along major strike-slip faults are well depicted. In the areas covered by younger volcanic sequence the method has been effective in enhancing dikes which represent fractures that acted as feeders to the volcanic extrusions. On this image dikes as narrow as 3 m could be detected for their conspicuous positive topographic expression against the rather flat lying volcanic rocks, despite the 30 m resolution of the TM. They are generally shadow free, due to their limited hight of few metres, making them distinct from other non-dike linear topographic features that are often associated with shadows. The lineament data have been treated in Sections 2.2.4 and 6.5.

4.6.2 Variance filtering

Unlike spatial characteristics which describe the tonal variation of an object, texture contains information about the spatial distribution of this tonal variation. It is defined by the multidimensional variance observed in a moving window, and is one of the basic characteristics of an object's form useful for visual image interpretation. For this application variance has been chosen since it expresses the extent of tonal variation in an area, as a representation of texture (see also Drury, 1993) better appropriately than the mean or the median filters.

A texture analysis was conducted for the Odi subscene using a variance filter of 7x7 pixel window on the stretched version of the six reflective bands of Landsat-TM. The result shows that lithologic contrasts are better enhanced in bands 1, 5 and 7 whereas linear features are apparently more pronounced in band 4. However, the Odi rift-basin structure is very conspicuously depicted on all the obtained images by a dark zone with sharp boundaries, but more remarkable in TM-4. A band composite 7, 5 and 1 in R, G and B, respectively, provided the best spectral information. On this composite granites, the metasediments, metavolcano-sediments, and the Odi volcanics are well discriminated. A similar processing conducted for raw data gave inferior result. Figure 4.5 shows interpretation of variance-filtered band 7 image. On this image about five tonal variations which correspond to different groups of rocks have been identified. The very smooth areas (dark) represent unconsolidated Quaternary sediments. The smooth areas which represent basalt, gneisses and graphite schist are in dark grey. The metasedimentary rocks (greenschist facies) and the rhyolite are represented by medium variance of grey tone (mixed), whereas the light grey tones correspond to the relatively rough texture mainly displayed by granites. Metavolcano-sediments and amphibolite facies rocks along the ATTSZ exhibit the maximum variation in tone.

An attempt was also made to evaluate the capability of principal component images in giving better result for texture analyses, since especially the first component is known to map albedo and topographic information. In this exercise, among the first three components, variance-filtered PCI gave good lithologic information by also enhancing structural features, with improved results from those obtained from stretched data. PC2 discriminated the various rock units fairly good, whereas PC3 gave no valuable information. The produced colour composite has thus been less useful for further interpretation.

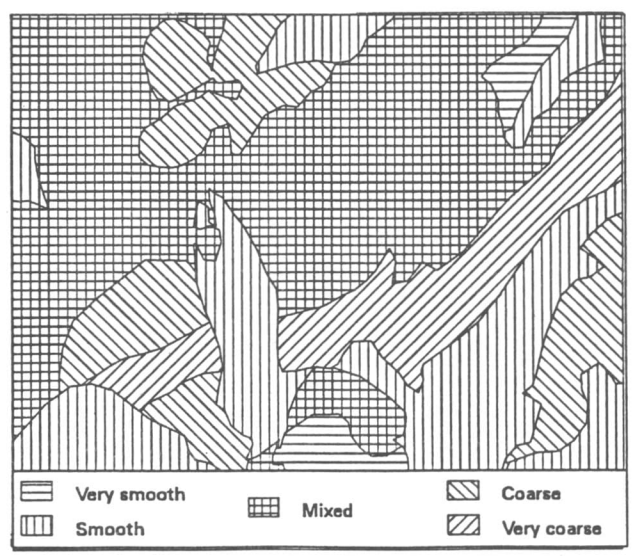

Figure 4.5. An interpretation of a variance-filtered image of TM band 7 produced by using a 7x7 window. Area is same as in Figure 4.2a-e. See text for explanation.

4.8 Alteration Mapping

4.8.1 Background

With an objective to evaluate some image processing techniques for applications to mineral exploration, the Ariab Mining District (AMD) of the central RSH have been selected as test-site. The area is known for gold exploration that is systematically active since 1990 (Wipfler, 1994), with the associated silica-barite lenses and disseminated sulphides. The sulphides are surfacially represented by 17 gossan [1] bodies, among which about 10 have a length ranging between 1-3 km and nearly all showing intense oxidation effects (Wipfler, 1994). Magnetite is the most abundant oxidation product observed in the massive sulphides consisting of principally pyrite, sphalerite and chalcopyrite. The metavolcanic country rocks show effects of chloritisation, sericitisation, carbonisation and silicification, whereas high fluorine content and the formation of hydroxylated minerals coupled with the occurrence of alunite in the silica-barite suggest involvement of hydrothermal solutions (Wipfler, 1994). Figure 4.6 shows the geological map and the gossan occurrences of the Ariab subscene.

It has been well established that ferric iron exhibits pronounced absorption features at around 0.87 gm and 0.35 /zm (with subordinate band around 0.5 /zm) whereas ferrous iron has major absorption at 1.0 /zm, 1.8-2.0 /zm and 0.55-0.57 */j.m* (eg. Gupta, 1991). Hydroxyl-bearing minerals like clays are known to have a major absorption band around 2.1-2.24 /zm, whereas carbonates show absorption features around 1.9 /zm, 2.35 */jm* and 2.5 /zm (eg. Gupta, 1991). Since most alterations involve some or all of these minerals their detection has been used for many exploration projects.

[1] According to Bates and Jackson (1987) gossan is an iron-bearing weathered product overlying a sulphide deposit. It is formed by oxidation of sulphides and the leaching-out of the sulfur and most metals, leaving hydrated iron oxides and rarely sulfates.

4.8.2 Ratio images

Ratio images are known for enhancement of spectral contrasts among the bands considered in the ratioing and it has successfully been used in mapping alteration zones (eg. Abrams *et al.,* 1983; Segal, 1983). Using the theoretical knowledge over the spectral property of most rocks and mineral (eg. Hunt and Salisbury, 1970, 1971; Hunt *et al.,* 1971, 1974) and the occurrence of gossans associated with gold mineralisation in the Ariab area, TM band ratios 3/1 and 5/7 were selected for iron-oxides and hydroxylated minerals, respectively. Ratio 5/4 has been computed to enhance possible ferrous oxides and suppress vegetation, as also used by others (eg. Rockwell, 1989).

Based on the above considerations a ratio composite image was produced for the Ariab area using bands 5/7, 5/4 and 3/1 in R, G and B, respectively. The obtained image has mapped the known gossan occurrences in reddish yellow colour that indicates the occurrence of significant hydroxylated minerals. Abundance of magnetite has possibly reduced the overall reflection and subdued the absorption caused by the iron-bearing minerals in TM band 1 because of its opaque nature (eg. Davis *et al.,* 1987). Interestingly, a "hydrothermal composite" of 5/7, 3/1 and 4/3 in R, G and B, respectively, gave an identical image supporting the same conclusion. Close observation of the image has revealed that Oderuk and Kamoeb occurrences have not been mapped, and the Hassai gossan is in cyan colour for significant ferric and ferrous iron. Furthermore, shadows are mapped in these composites with a similar hue, although their distinction is eased by the morphological differences.

A compound ratio of MSS bands (4/5)/(6/7) has been used by Segal (1983) for mapping limonitic rocks. A comparable double ratio of TM (3/4)/(4/5) was computed for the Ariab area since ferric iron are expected to be present in limonite formed from decomposition of sulphides and those from laterite (Gupta, 1991). A composite ratio image was then produce by using the bands 3/4, (3/4)/(4/5) and 4/5 in R, G and B, respectively. The image is generally inferior as compared to the above colour ratio composites but managed to show the alteration

zones enriched by ferric iron (in limonite) in yellowish hue due to their spectral absorption around 0.88 *pim* (TM-4) as expected. A little improvement has been achieved by substituting the ratio 5/7 for 4/5, whereby the altered zones showed a bright- to light-blue colour.

4.8.3 Feature Oriented PCA

In principal component transformation new statistically decorrelated axes are calculated from the input data where the successive components have smaller variance (see Section 4.4). The spectral character and abundance of the objects in the scene strongly influence the image statistics. Crosta and McM. Moore (1989) described a method called Feature Oriented Principal Component Selection (FPCS) whereby selected bands believed to contain spectral information over an intended target are used in PC transformation. In two of the four input bands the target object is expected to exhibit a contrasting response. In this approach the eigenvector loadings are examined to tell which component contains information related to the theoretically known spectral signatures of the target object in the original bands. Those PCs in which the desired target has been mapped are then selected, based on the significance of their contribution. Details of the procedure has been well elaborated by Loughlin (1991).

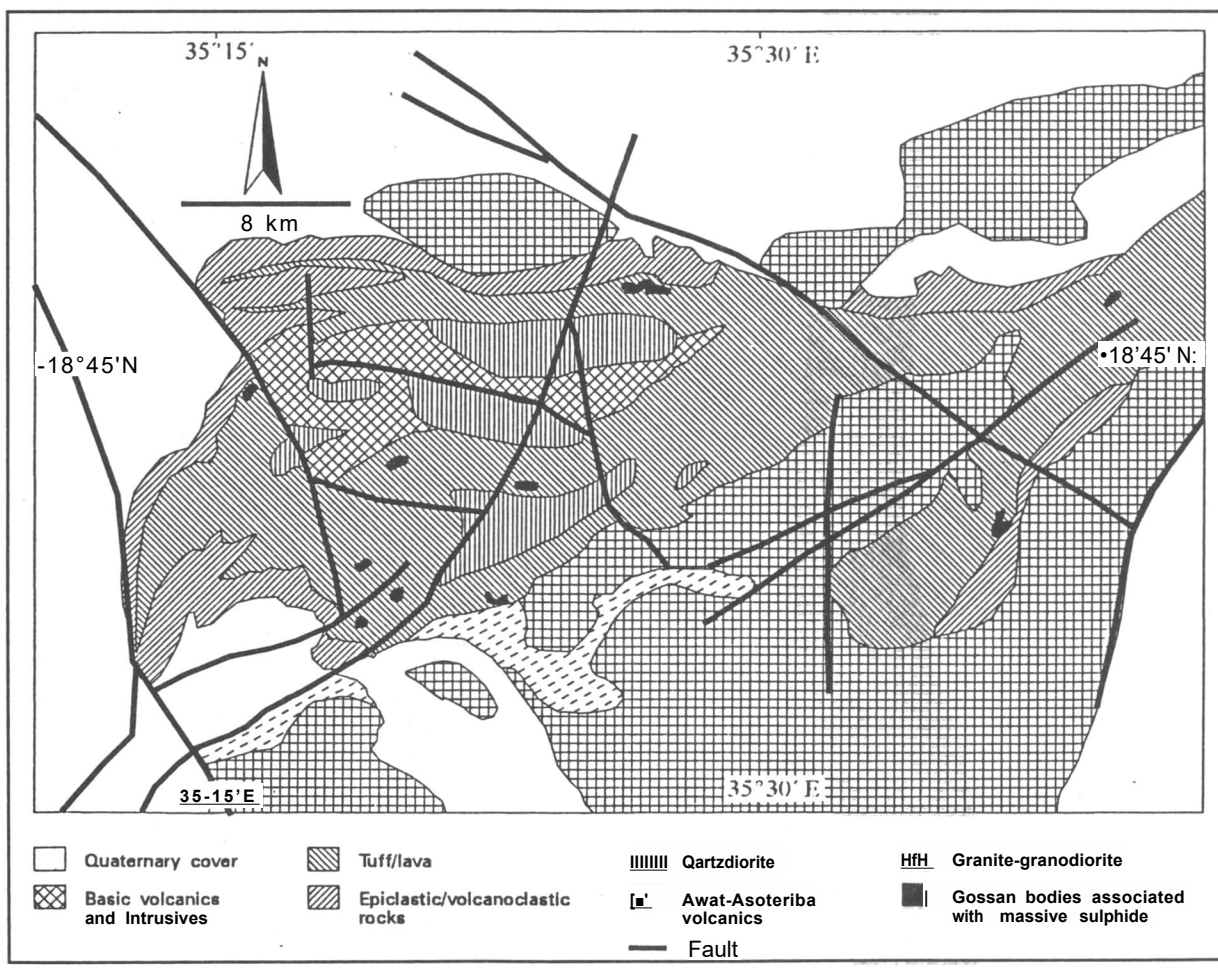

Figure 4.6. Geological map of the Ariab area with the major gossan occurrences. Ad:Adaiamet, Ak:Adassedakh, Ba:Baderuk, Ga:Ganaet, Ha:Hassaai, Hd:Hadal Auatib, Ka:Kamoeb, Od:Oderuk, Um:Umbarasin, Ta:Talaiderut. After Wipfler (1994).

For enhancements of both iron-oxides and hydroxyl-bearing zones, two sets of four TM bands were selected: bands 1, 3, 4 and 7, and bands 1, 4, 5 and 7, respectively. This selection is based on the fact that the former have contrasting signatures in TM bands 1 and 3, and the latter in TM bands 5 and 7, and an input of four bands is preferred for selective enhancement (Loughlin, 1991).

The above described two PC transformations were conducted for the Ariab area, and Table 4.7 gives the eigenvector loadings of both band sets in percentages, for better visualisation. It can be see that in both cases the first PCs effectively mapped albedo and topographic information that are responsible for strong correlation between multispectral image channels whereas the second PCs display the difference between VIS/NIR (bands 1 through 4) versus SWIR bands (TM-5 and -7) as dark and bright pixels, respectively.

As it can be seen on Table 4.7a, PC3 has no contrasting response from TM bands 3 and 1, and it thus less useful. However, PC4 has mapped iron-oxides as negative loadings (-45.78%) in contrast to PC3. For hydroxylated minerals (Table 4.4b) both PC3 and PC4 have contrasting signs from TM 5 and 7, but PC4 has relatively more loading (-29.41%) as compared to PC3 (-20.86%). In the latter case it is possible to compute a PC transformation of PC3 and PC4, and generally one of the resulting two components is supposed to exclusively map the hydroxyl minerals (Loughlin, 1991). For the present study the two PC4s were subsequently negated in order to have the corresponding minerals as bright pixels, and give the "iron-oxide" and "hydroxyl" images, respectively. Corollary to this operation is that the possible input of vegetation from TM-4 is mapped in dark pixels and thus excluded from being incorporated into the "alteration map". A "hydroxyl + iron-oxide" image was also obtained by a linear combination of these two images, followed by rescaling. A composite image was then produced by combining the "hydroxyl", "hydroxyl + iron-oxide" and "iron-oxide" images in R, G and B, respectively. The next important step was to run a low-pass spatial filtering in order to remove or subdue effects of the incorporated significant noise from the high-order PCs as it is often expected. For the Ariab area a 3x3 window yielded aesthetically the best result. The filtering process has also the effect of improving the hue by removing isolated pixels smaller than the applied window size. Figure 4.If shows the acquired image.

The obtained result has been compared with the known gossan bodies in the area (Figure 4.6) and apparently, except for the Baderuk and Kamoeb occurrences, all such alterations have been successfully mapped in distinct reddish yellow colour, in addition to showing other potential sites. Their colour supports the dominance of hydroxylated minerals in the altered rocks perhaps by the removal of iron-rich minerals through solutions, for reasons given above. Buckingham and Sommer (1983) also indicated the occurrence of such minerals in most gossans. Further comparison, with the result obtained by List *et al.* (1992) over

Table 4.7. Band statistics and eigenvector loadings (in %); (a) for "iron-oxide" mapping using TM bands 1, 3, 4 and 7, and (b) for "hydroxyl mapping using bands 1, 4, 5 and 7 for the Ariab area.

a)

	TM-1	TM-3	TM-4	TM-7
Mean	104.00	76.40	66.20	79.97
Stand.Dev.	12.90	19.70	17.87	16.50
PCI	22.62	36.15	26.63	28.93
PC2	-0.4.17	-14.46	-21.61	54.72
PC3	-50.00	-03.61	26.13	11.32
PC4	23.21	-45.78	25.63	05.03

b)

	TM-1	TM-4	TM-5	TM-7
Mean	104.00	66.20	121.47	79.97
Stand.Dev.	12.90	17.87	26.35	16.50
PCI	18.65	24.21	37.97	21.99
PC2	-16.95	-36.32	11.76	32.46
PC3	47.45	-13.16	-20.86	14.14
PC4	-16.95	26.31	-29.41	31.41

the same area using ratio technique, shows significant agreement. A case to be considered in this method is that since the high order PCs often contain noise the composite image may not be recommended for lithologic identification at large scales. Furthermore, the required relatively long processing steps, added to the lack of topographic features significant for image interpretation, make the method less useful for such applications.

4.8.4 GIS overlay technique

Close observation of the FPCA image revealed that there are unconsolidated Quaternary sediments mostly associated with drainage channels that also exhibit a signature similar to that of the alteration bodies (Figure 4.2f). Although morphological criterion provide sufficient clue to discriminate the two, a technique to reduce the subjectivity of the resulting image is often preferred. In view of this, a GIS matrix-overlay technique was employed. This involved a supervised classification of both the ratio composite and the FPCA images based on *a priori* knowledge obtained from the available map (Wipfler, 1994). The classification gave two GIS files with 8 classes, each referring to the rock types (Figure 4.6). The separability between the classes of altered rocks (gossans) and unconsolidated sediments is apparently good (Table 4.8), especially between the Quaternary sediments and the other rocks.

The classified images were then recoded with an off-set of 1, whereby the alteration classes were given a value of 1 and all the other classes obtained a value of zero to give two binary GIS files. This was followed by a matrix-overlay using an "intersection" function, in which case those classes having a value of 0 and 0, 0 and 1, and 1 and 0 in the GIS files obtained from the ratio composite and the FPCA images, respectively, were given a new value of zero. Only those pixels having a value of 1 in both of the binary GIS files obtained a new value of 1. In order to omit those pixels or group of pixels with less than 100x100 m^2 size a 3x3 low-pass filter was run. The latter operation further refined the binary image.

The resulting overlayed GIS file has been compared with the image obtained from FPCA (Figure 4.2f) and it appears that all the Quaternary sediments have been excluded from the "alteration map". As expected some of the gossan bodies have been omitted from the binary image since they are already missing in one or both GIS files obtained from band ratioing and FPCA operations (see above). Nonetheless, the other seven gossan occurrences have been exclusively detected, making the method extendable to other areas. It is worth mentioning that the ratio image has an advantage of

Table 4.8. Error matrices of the training classes used for classification of FPCA (a) and ratio image (b). Columns and rows represent classified and reference data, respectively. Numbers correspond to rock units as given in parenthesis in Figure 4.6. Values (in %) rounded to the nearest decimal.

a)

Cl.	1	2	3	4	5	6	7	8
1	17.6	8.6	4.1	13.1	0.4	0.9	1.0	0.1
2	44.0	66.3	4.0	33.6	0.0	9.0	10.0	0.0
3	8.2	1.2	60.9	6.1	3.5	4.7	17.2	0.0
4	8.2	6.2	4.4	16.0	1.1	3.6	4.9	0.4
5	1.0	0.0	4.1	1.5	90.2	0.5	2.4	0.2
6	10.4	9.4	14.7	15.8	2.4	71.2	34.1	0.0
7	10.6	8.4	7.8	13.9	2.4	10.2	30.3	0.0
8	0.0	0.0	0.0	0.0	0.0	0.0	0.0	99.5

b)

Cl.	1	2	3	4	5	6	7	8
1	18.3	9.2	6.4	13.0	1.2	1.1	0.85	0.1
2	39.7	67.0	5.7	35.4	0.2	9.4	0.9	0.0
3	8.6	1.4	59.3	5.5	3.7	4.3	16.2	0.0
4	9.6	5.6	6.6	16.9	1.0	3.9	17.2	0.6
5	1.3	0.1	4.4	2.5	87.9	0.7	2.5	0.1
6	10.7	8.0	9.4	11.8	2.9	70.6	32.2	0.0
7	11.8	8.7	8.2	14.9	2.9	10.0	30.2	0.2
8	0.0	0.0	0.0	0.0	0.0	0.0	0.5	99.0

not convolving undesired objects with the gossans, and yielded more realistic result as compared to the FPCA image, but possible potential sites are better depicted on the latter.

It is to be noted that more gossan bodies were mapped from the two processing methods using a 'union' function whereby all identified gossans are merged to a binary GIS file. In this procedure, therefore, the Baderuk and Oderuk (Figure 4.2f) gossans were also detected, in addition to the other seven bodies, whereas the Kamoeb gossan is the only occurrence to remain unmapped by both procedures. The result also incorporates the Quaternary covers along with the gossans and morphological features may be applied to exclude them from the alteration map.

4.8.5 IHS decorrelation stretching

As it has been described in section 4.3.1, IHS transformed image obtained from the composite 7, 4 and 1 in R, G and B, respectively, provided substantial enhancement and was thus used for lithologic mapping of the study area. During the course of interpretation of this image (particularly that obtained from stretched data) anomalous signatures were also noted and checked in the field. Among such features was a deep-red colour displayed by small ridges when seen on this image and thus suggesting higher reflectance in TM-7 (poor in hydroxylated /carbonate minerals) and major absorption in bands 1 and 4 (possibly enriched by ferric- and ferrous-oxides). Alternatively, the gossans also contain some hydroxylated minerals that have absorption bands in TM-7, as expected from alteration zones, but still bear higher reflectance as compared to VIS/NIR parts. The spectral behaviour of this body has been discussed in Section 5.

Field verification of one such supposedly iron-oxide enriched rock has proven to be a gossan body that shows fairly intense oxidation effects and dissolutions, its deeply weathered product giving reddish soil. The discovered gossan, called as "Jabal Malaket Gossan" after the ridge on which it is exposed, occurs about 20 km E of the Derudeb township close to Khor Derudeb (Figure 4.1). It occupies a rounded hill of about 0.1 km^2.

A number of other bodies with a similar signature have as well been checked in the field. Most of them were found to be ferruginous quartzite that contain fair amount of iron-oxides as shown by reddish colour on the outcrops. Quartzofeldspathic bands in the metavolcano-sedimentary sequence, and amphibolites also exhibit a comparably deep-red colour on the same composite, due to effects of desert varnish and iron-oxides (see Section 5.3). The latter could be distinguished on their persistent nature in the metamorphic sequence.

The known Abu Samar massive sulphide mineralisation in the NW (Enclosure) could not be detected on this image because of its small size and the exceptionally high reflectance (adjacency effect) from the surrounding Quaternary sediments and mainly sandy plains. Although the Ariab gossans have not been visited by this work their distinction is, on the other hand, apparent from the processed images. Nonetheless the spectral character of Ariab gossan, that also contains manganese concentration, has been helpful for characterising the gossan bodies in the area.

4.9 Digital Image Classification

4.9.1 Introduction

According to ERDAS (1982-1994) image classification is defined as the process of sorting pixels into a finite number of classes or categories of data. The categorisation is based on the data file values of individual pixel and it follows a set of criteria. Two major approaches are generally known: supervised and unsupervised classification. In the former case *a priori* knowledge of the study area and the different classes is needed to establish training areas that represent each category. The latter involves algorithms that examine unknown pixels in an image and aggregates them into a number of classes based on the natural groupings or clusters present in the image values (Lillesand and Kiefer, 1994). In unsupervised classification it is the analyst who tries to give meanings to the

different classes *(a posteriori* identification) in the resulting image.

4.9.2 Spectral classification

In this work an attempt was made to evaluate the significance of supervised classification for lithologic discrimination in the Odi area. To this end fourteen different classes were identified based on ground-truth data, to represent the major lithologic units in the area. Locations of the observations points were controlled by using a GPS. The training areas were then tested for their separability as given by the error matrix (Table 4.9). While Quaternary sediments appear to have a classified data of 92% and gabbro represents the least homogeneous unit with 54.5% misclassified pixels, other rock units fall between these two end members. Lithologic units such as undifferentiated gneiss and metavolcano-sediments also show a low percentage of correctly classified data due to their obvious inhomogeneous nature.

Table 4.9. Contingency matrix of the signatures corresponding to each rock class, classified data (columns) versus the reference data (rows) obtained for the Odi subscene. Numbers refer to rock types: l=basalt, 2=dacite, 3=ferruginous quartzite, 4=gabbro, 5=granite, 6=graphite gneiss, 7=graphite schist, 8=metasediments, 9=Quatemary cover, 1Orhyolite, 11=sandstone, 12=undiff. gneiss, 13=unidff. sedimentary rocks and 14=undiff. metavolcano-sediments. Bold diagonal No. refer to correctly classified data (in %) of each class.

%	1	2	3	4	5	6	7	8	9	10	11	12	13	14
1	**62.27**	-	0.68	23.21	0.83	5.08	1.04	4.62	0.14	0.77	3.24	0.25	3.71	0.60
2	-	**83.52**	0.35	0.01	5.18	0.02	-	-	0.16	5.23	-	11.02	0.13	6.25
3	0.49	0.45	**78.42**	3.43	0.17	3.64	0.07	0.10	0.03	0.47	0.83	9.93	1.69	6.60
4	14.30	0.03	1.21	**45.53**	2.22	0.03	0.13	5.67	-	1.37	3.45	0.39	5.49	1.57
5	0.75	2.68	-	2.59	**75.33**	4.70	-	0.33	2.70	4.64	1.84	0.73	0.13	2.98
6	5.20	-	5.47	7.33	0.01	**72.53**	8.16	3.09	0.69	2.16	-	2.09	13.36	0.64
7	1.75	-	0.30	0.41	-	4.70	**80.51**	12.07	0.10	0.01	-	0.01	2.41	0.01
8	4.60	-	0.03	4.76	0.94	1.50	9.44	**71.95**	0.09	0.07	-	0.01	0.69	0.46
9	0.10	1.62	0.06	0.14	0.96	0.89	0.10	0.63	**92.49**	0.29	0.08	1.65	3.83	0.17
10	0.59	3.72	0.50	1.54	4.30	1.94	0.18	0.10	0.01	**68.54**	0.05	7.22	0.70	13.49
11	8.51	0.10	1.48	4.10	3.86	0.05	-	-	-	0.29	**88.75**	0.48	1.00	1.72
12	0.03	5.98	5.53	0.47	0.23	2,13	0.04	0.04	0.73	7.20	0.03	**56.86**	2.12	12.18
13	0.95	0.10	0.53	4.68	0.26	2.05	0.24	0.66	2.86	0.07	0.67	0.39	64.72	0.26
14	0.46	**1.81**	5.44	1.81	5.74	0.70	0.10	0.74	-	8.88	1.06	8.97	0.02	**53.63**

Using the raw data in the six reflective bands of the Landsat TM the training areas were then tested for their separability on the possible three-band combinations. The signature separability, which is a statistical measure of distance between any two signatures, has been obtained using Euclidean,

Divergence, Transformed Divergence, and Jefffies-Matusita methods. The first method measures the spectral distance between the mean vectors of each pair of signatures, and it is the basis for the minimum distance classification (ERDAS, 1982 - 1994). The other three methods are related to the maximum likelihood classification rules and they all take into account the covariances of the signatures in the bands being compared in addition to the mean vectors of the signatures (ERDAS, 1982-1994). Table 4.10 gives the methods used and the band-triplet selected using the statistical data of the signatures.

Table 4.10. Separability of the training areas representing the various lithologic units, with scores of the corresponding band-triplets and classification methods.

Separability	Divergence	Euclidian Distance	Jefferie Matusita	Transformed Divergence
Best Minimum	1,4,5	1,4,5	1,3,5	1,4,5
Average	194	27	mi	1954
Minimum	6	2	518	1099
Best Average	1,3,7	3, 5, 7	1,4,7	2, 4, 7
Average	220	31	1179	1960
Minimum	3	1	406	662

For the best-minimum separability bands 1, 4 and 5 seem to provide the best results in three of the four applied methods. Using the best-average separability, however, bands 1, 4 and 7 appear to yield the maximum divergence of the signatures. The latter result is in good agreement with those obtained by best band composite selection using band correlation coefficients (Section 4.1.3).

Considering the methods of Jefrie Matusita and the Transformed Divergence least separability values were obtained between signature pairs of basalt/gabbro, rhyolite/undifferentiated gneiss and quartzite/ undifferentiated gneiss. These features

Table 4.11. Error matrix of the classified data (columns) versus the reference data (rows) obtained for the classified image. Numbers refer to rock types as given in Table 4.9. Bold diagonal numbers represent correctly classified percentages.

%	1	2	3	4	5	6	7	8	9	10	11	12	13	14
1	**47.42**	-	1.38	19.22	0.01	3.48	0.94	3.49	0.04	0.81	2.99	0.16	0.50	0.24
2	-	**82.25**	2.53	0.07	11.97	4.99	-	-	6.42	6.13	-	7.74	0.21	9.52
3	0.78	0.40	**35.72**	4.07	0.003	12.62	0.14	-	0.05	0.26	0.72	12.56	0.02	3.46
4	**16.74**	0.06	6.20	**41.80**	1.00	10.73	0.07	5.64	0.012	1.35	3.4	0.17	1.26	0.83
5	0.16	2.54	0.37	3.30	**46.61**	0.44	7.16	-	0.01	5.68	1.80	0.11	-	2.64
6	10.82	0.09	2.02	10.72	0.001	28.04	-	0.58	0.95	2.18	-	1.96	3.54	0.22
7	2.13	-	0.29	1.04	-	1.14	**82.94**	6.85	0.001	0.03	-	0.01	0.16	-
8	11.60	-	1.80	2.85	0.10	1.67	8.29	**82.57**	0.002	0.03	-	0.004	0.13	0.16
9	0.04	2.65	0.26	0.10	0.30	3.97	0.001	0.11	**87.15**	0.29	-	1.70	5.48	0.10
10	1.40	4.0	2.05	2.75	27.17	4.87	0.08	0.02	0.05	**69.53**	0.03	5.72	0.10	20.62
11	6.16	0.06	2.1	3.93	2.08	0.65	-	-	0.04	0.20	**89.53**	0.22	-	1.03
12	0.07	5.60	14.13	0.79	0.01	16.31	0.04	-	4.22	7.45	0.08	**58.48**	0.53	13.4
13	0.31	0.14	0.40	3.33	0.07	7.30	0.26	0.36	0.92	0.13	0.58	0.32	**88.04**	0.09
14	2.37	2.01	30.74	3.25	8.64	3.76	0.06	0.38	0.02	5.91	0.86	10.81	-	**47.64**

are attributed to the compositional similarities and geologic associations in these units. The obtained results for most of the other classes, however, appear to be satisfactory by these two methods. Using the selected bands 1, 4 and 7 of the TM a maximum-likelihood classification was run for the Odi area. This method considers the probability that a pixel belongs to a particular class, based on the assumptions that these probabilities are equal for all classes and the input bands have normal distribution (ERDAS, 1982-1994).

The classified image was also assessed for its accuracy. This was done by defining reference areas (polygons) for each class that are different from the training areas, as known from ground-truth data. These were then used as a "mask" against the input classified image. The accuracy was then estimated by dividing the number of correctly classified pixels by the sum of the pixels that were supposed to belong to that particular class, from within the reference polygons, in the classified (masked) data. Table 4.1 1 shows the obtained error matrix for the classified data.

Result of the accuracy assessment shows that the obtained image has managed to discriminate units such as metasediments, graphitic schists, Quaternary cover, sandstone, undifferentiated sedimentary rocks and dacite for all of which an accuracy of over 80% was obtained (Table 4.1 1). In case of the latter three, their limited exposure and proximity of the training and reference areas have possibly exaggerated the accuracy. Significant overlaps (-30%) occur between ferruginous quartzite (and amphibolite) and undifferentiated metavolcano-sediments, and between rhyolite and granite. About 20% of the reference pixels from gabbro and undifferentiated metavolcano-sediments were also misclassified as basalt and rhyolite, respectively. These are ascribed to the compositional similarities between the rock units, inhomogeneity of the reference areas themselves added to that of the lithologic units.

Visually the classified image appears to have discriminated only those units having higher accuracy percentages. However, most of the units appear less discriminateable, making the application of digital classification for lithologic discrimination of limited significance, at least in the test area.

4.9.3 Texture classification

In contrast to the above described classification methods that are based on the grey value vector of each pixel, texture classification permits the use of the influence from the neighbouring pixels for the clustering process (Haralick, 1978). The Evidence-based Interpretation of Satellite Images (EBIS) module allows the latter to be performed based on the local histogram within the desired window, or based on different co-occurrence matrices of variable orientations, or combinations of the above two (Lohmann, 1994). The local histogram option is feasible in cases where grey value differences between the various classes is good enough to help their distinction, as in spectral classification methods (see Section 4.9.2), in this case based on the neighbourhood pixels within the specified window. Classification based on local grey value operations is less successful in geological applications, as seen in the previous section, since the lithologies them selves are commonly inhomogeneous and the minerals that often influence spectral signatures are few. Furthermore, these minerals are less often restricted to only a particular rock type to denote a substantial distinction.

Co-occurrence matrices are special types of histogram representations that record the relative frequencies of spatial co-occurrences of grey values, rather than the relative frequencies of grey values (Haralick, 1978). That is, the frequency at which two grey values occur adjacent to each other along a specified direction and window size is recorded within the matrices' entry. As a result, directional grey value variations are better enhanced as variation in local texture.

The EBIS texture classification module has been applied to the Odi subscene using raw data of bands 1, 4 and 7 of the Landsat TM and the same training areas applied for spectral classification. For this computation a window of 15x15 have been used to enhance only variations of larger area, and a grey level of 14. After applying the 'local histogram' function to the three layers the resulting image shows inferior result than the input data. On this image only the metasediments are distinctly mapped

although similarity with basalt and basic intrusives is apparently unavoidable as in most of the image enhancement methods applied. Other rock units are much less distinct and poorly discriminateable.

A similar attempt made using TM band 1 yielded slight improvements in discriminating graphite schist from basalt. On this image undifferentiated metavolcano-sediments are fairly distinct but similar to granite and other acidic rocks. The other rock units are hardly differentiable. Using left-diagonal, vertical and right-diagonal co-occurrence matrices with TM bands 1, 4 and 7 provided no considerable improvements in lithologic discrimination. The metasediments, basalts and graphite schist are fairly discriminateable, whereas the other units are poorly differentiated. One feature observed on this image is that shadows are mapped as unclassified pixels as an effect of directional frequency of grey value variation related to the co-occurrence matrices. The method seems less useful for lithologic discrimination in the present context.

5 Spectral Analysis

5.1 Introduction

Spectral measurements of minerals and rocks in the laboratory have been conducted since the early 1970's (eg. Hunt and Salisbury, 1970, 1971). The results of such studies have provided essential information in designing successive sensor systems thereby promoting remote sensing applications in mineral exploration, despite the obvious difference between laboratory and remote sensing conditions. The idea herein is that although interference of the atmosphere in different parts of the spectrum is variable (Section 3.2), the effects are believed to be comparable for different rock types, making it a common parameter. Laboratory measurements, therefore, remain important and a basis even for specific applications of spaceborne data.

Reflectance measurements of selected rock and gossan samples from the Derudeb area have been carried out under laboratory conditions. The main objective was to study their spectral characteristics and thereby evaluate the comparability of the results with Landsat TM data in discriminating the gossan bodies, as alteration markers in gold and sulphide mineralisation, from the other rock types. Furthermore, the effect of desert varnish on the reflectance spectra of different rock types in the context of the spectral ranges covered by the Landsat TM, has also been assessed for this particular area.

The spectral laboratory measurements were made a on Lambda 19 UV/VIS/NIR spectrometer at the Geo-Forschungs-Zentrum (GFZ) in Potsdam (Germany). Initially, reflectance from a reference plate of barium sulphate ($BaSO_4$) was calibrated at 652 nm using radiation from a halogen lamp. Samples with preferably even surfaces (often cut) were set on a 2x1 cm^2 window and their reflectance was measured against the standard plate. The resulting reflectance curves were processed using the "Geospectre" software at the same institution.

For the purpose of this analysis the reflectance measurements were conducted in the range between 0.4 and 2.5 gm so that all the TM reflectance bands are covered. A resolution and a NIR-sensitivity of 3 nm and 5 nm, respectively, have been considered sufficient in order to keep the signal-to-noise ratio optimum. The measurements were conducted at an interval of 1 nm with a speed of 480 nm/min. One sample has been considered representative for each rock type, and an average of three measurements over a moving window was used for this analysis in order to minimize uneven readings. In order to establish the effect of desert varnish on the reflectance of the different rocks within the TM band ranges, surfaces with and without desert varnish were measured for each rock. Statistical analysis was conducted using the SPSS software at the Institute of Geology, Geophysics and Geoinformatics, Free University of Berlin.

Statistical Analysis

The objectives of this analysis were to evaluate the potential of TM data to separate altered and unaltered rocks and to analyse the correlation between the bands that best discriminate rocks in both TM and laboratory data. The statistical analysis were divided into two parts: reducing the number of variables to those having higher discrimination power, and evaluating the separability of gossans from the other rock types.

In order to reduce the dimensionality of the data, two methods were used: Principal Component Analysis (PCA) and Stepwise Discriminant Analysis (SDA). PCA transforms the variables to a new set that describe the variability with fewer variables (see also Section 4.4). The result is that the data set is transformed from a number of correlated spectral bands to a lesser number of uncorrelated variables by linear combination of the original variables (Davis, 1986). SDA reduces the number of variables to those important in discrimination between altered and unaltered rocks, assuming that the data within individual bands have

normal distribution. This method selects variables by minimizing the within-class variance and maximizing the between-class variance and identifies specific bands that are the best class-predictors by stepwise selection (Davis, 1986). For the latter operation, at each step the variable that contributes least to the discriminatory power of the model as measured by Wilk's Lambda test is removed, whereas inclusion is based on the F-statistics derived from a sequential analysis of covariance (Davis, 1986).

Cluster analysis permits the grouping of objects under investigation into clusters based on specific variables with no *a priori* knowledge as to neither the number of groups nor to which group a sample belongs (Davis, 1986). Hierarchial clustering connects the most similar observations, then successively connects the next most similar observations to these. In this study cluster analysis has been used to evaluate the difference in center of clusters between altered and unaltered rocks based on spectral data.

5.2 Altered vs. Unaltered Rocks

Cut surfaces

As stated above one of the main objective of the spectral analyses was to evaluate the differentiability of altered rocks (mainly gossans) potentially related to gold-sulphide mineralisations, from unaltered barren rocks. To this end the spectral characteristics of 15 samples (numbers 1-15 on Appendix-2) were statistically treated. Using reflectance measurements obtained from cut surfaces two factors were extracted by principal component analysis: the first component is highly dominated by positive loadings from bands 1, 2, 3 and 4 of the TM (low negative correlation with factor-2) whereas the second component is positively loaded only by TM bands 5 and 7 (Table 5.1). Interestingly, this observation is similar to the pattern observed in PC2 of the Landsat data (Section 4.4). Scatter plots of the measured data show that the gossans have higher positive loadings

Table 5.1. Factor scores obtained for cut samples using PC analysis.

Band	factor- 1	factor-2
1	0.919	-0.389
2	0.941	-0.335
3	0.978	-0.204
4	0.989	-0.087
5	0.810	0.574
7	0.743	0.663

in factor 2,whereas the non-gossan samples show low scores in factor 2 and wide ranges of values in factor 1 (Figure 5.1). Cross plots of the reflectance data from cut samples in TM band 1 vs band 5 (selected on the basis of linear discriminant function described below) show the differentiability of the Derudeb gossans from the non-gossan rocks (Figure 5.2).

Similarly, Q-mode factor analysis also revealed that gossans are the only samples showing a negative correlation with factor 1 and at the same

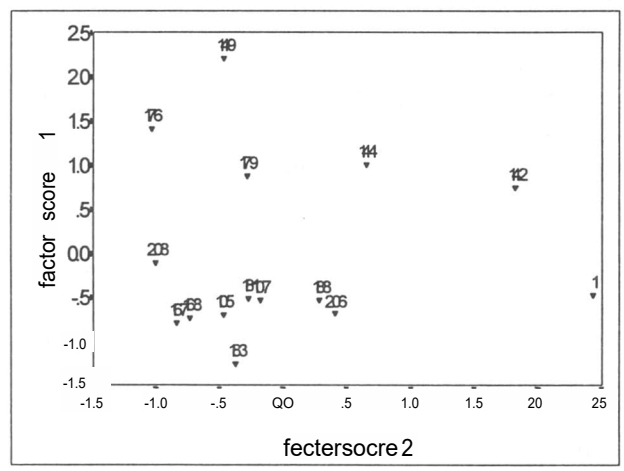

Figure 5.1. A scatter plot for reflectance values from cut surfaces of different rocks using factors determined by PCA. Numbers 1, 142 & 144 are gossans. For others see Table 5.4.

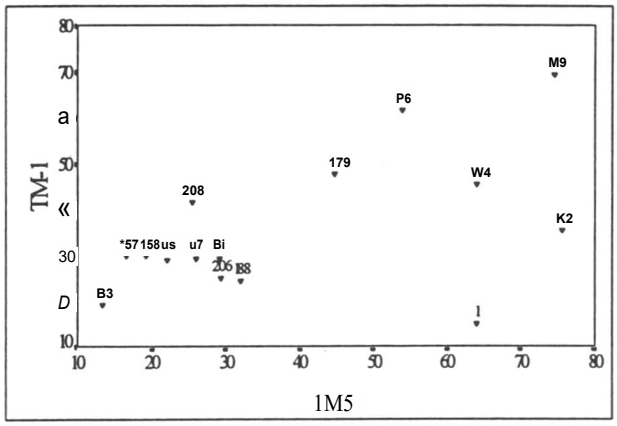

Figure 5.2. A scatter plot of TM bands 1 & 5 using reflectance values obtained from cut surfaces of different rocks. Sample numbers 1, 142 and 144 are gossans. For others see Table 5.4.

time a positive correlation with factor 2, while other rocks show various combinations of relations. A W-rich granite shows relatively high positive correlations in both factors and appears less resolved. In order to further substantiate the broad classification of the rocks R-mode cluster analysis was conducted using the Centroid Method. Interpretation of the resulting dendrogram (Figure 5.3) shows that the gossans can be fairly easily discriminateable from the unaltered rocks by forming a separate cluster.

In order to further verify the separability of these groups of rocks a two-group linear discriminant function was computed. Using a step-wise variable selection with Wilk's Lambda method a 100% classification between the gossans and the non-gossan rocks was obtained by employing bands 1, 2 and 5. Table 5.3 gives the eigenvalue and the variance of the canonical discriminant function.

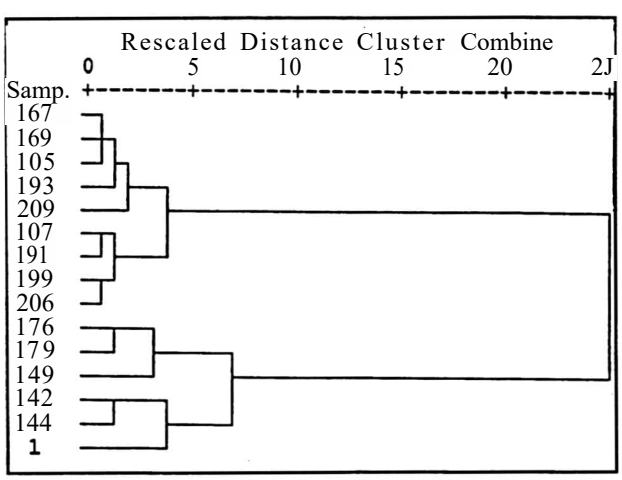

Figure 5.3. A dendrogram obtained for cut samples. Sample numbers 1, 142 and 144 are gossans. For others see Table 5.4.

Exposed surfaces

Using reflectance values obtained from the exposed surfaces of the same samples used in the previous section the differentiability of altered vs unaltered rocks was also statistically evaluated and compared with the results obtained from cut surfaces. R-mode factor analysis of exposed surfaces reveals a positive high loadings of TM bands 1, 2, 3 and 4 in principal component-1 (and a negative correlation with factor-2), while bands 5 and 7 are positively loaded in both components (high in factor-2), similar to the result obtained for cut surfaces (Table 5.2). This similarity in correlation shows the comparability of the two data sets despite the difference in the reflectance values. Appendix-3 shows the reflectance values measured over exposed surfaces of the samples studied.

Table 5.2. Factor scores obtained for exposed surface using PCA.

Band	factor-1	factor-2
1	0.92	-0.39
2	0.94	-0.33
3	0.97	-0.20
4	0.99	-0.08
5	0.81	0.57
7	0.74	0.66

A scatter-plot of the samples further reveals a strong correlation between the gossan samples and their high positive load in factor-2, whereas all the

other rocks show lower values in factor-2 and wide ranges of values in factor-1. Scatter plots of the factors depict the fairly good discrimination between these groups of rocks similar to the results obtained from cut surfaces (Figure 5.4).

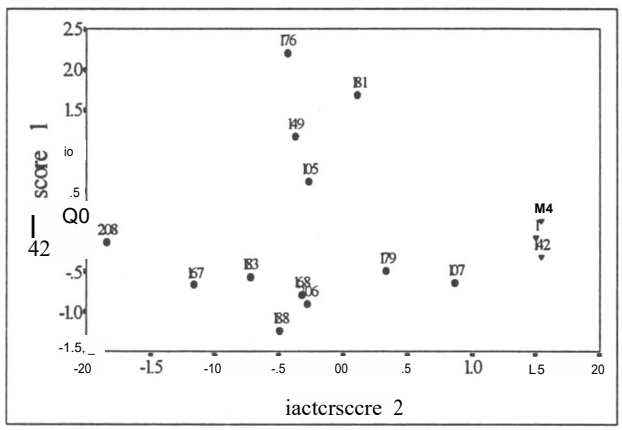

Figure 5.4. A scatter plot for reflectance values from exposed surfaces of different rocks using factors determined by PCA. Sample numbers 1, 142 & 144 correspond to gossans. For others see Table 5.4.

A result from R-mode cluster analysis using the Centroid method corroborates the above results in which the gossans show a well differentiated cluster from the unaltered rocks slightly better than in the case of cut surfaces (compare Figure 5.3 and 5.6). Using the method of Wilk's Lambda, with the same

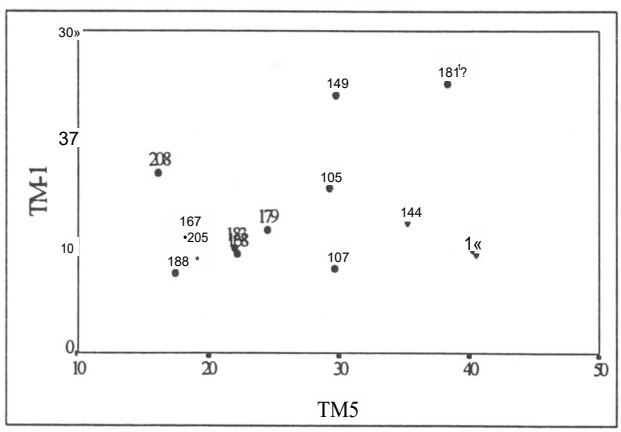

Figure 5.5. A scatter plot of TM bands 1 & 5 using reflectance values obtained from exposed surfaces of different rocks. Sample numbers 1, 142 & 144 represent gossans. For others see Table 5.4.

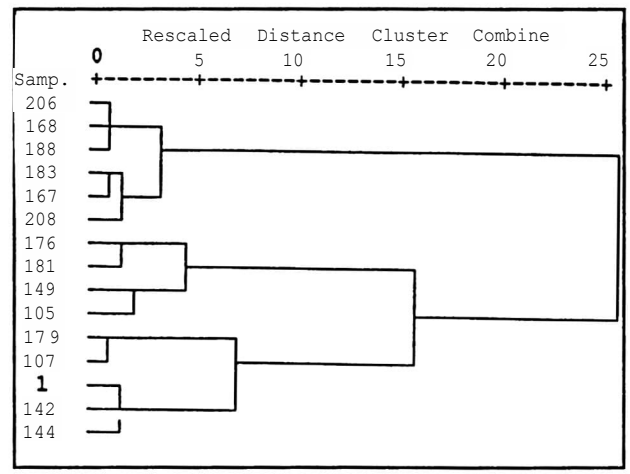

Figure 5.6. A dendrogram obtained for exposed surfaces. Sample numbers 1, 142 and 144 are gossans. For others see Table 5.4.

specifications as for the cut samples, a step-wise linear discriminant analysis yielded a classification accuracy of 93.33% using TM bands 1& 5. In this case only one granite sample rich in tungsten was misclassified. The obtained result depicts that gossans are discriminated from non-gossans also with their exposed surfaces, and the mineralised granite rich in tungsten is spectrally close to the gossans than to non-gossan rocks. Figure 5.5 shows the scatter plots of the data from exposed samples using TM bands 1 and 5.

Landsat TM - data

The above procedure was also applied to Landsat TM data in order to evaluate the extent of comparability between these data sets, although several factors such as data scaling, the various radiometric corrections, sensor parameters, etc. are known to contribute to their discrepancy. Such inferences have as well been previously used successfully (eg. Kruse, 1996; Palacios-Orueta and Ustin, 1996). To this end, grey values of pixels corresponding to sampling locations of those rocks used for laboratory measurement were obtained, with the help of a GPS, from Landsat TM data that has been corrected for haze effects. Appendix-4 gives the grey values used for the analysis.

A result from R-mode factor analysis shows that the first factor is loaded by high positive values from all the TM bands as expected, whereas factor 2 has a negative correlation with bands 1, 2 and 3 but positively loaded by bands 4, 5 and 7. A scatter plot of the TM data using these factors indicates that the gossans are not separable from the unaltered rocks. Using TM bands 1 and 5 that have been used for classification of the exposed data, a discriminant analysis conducted on TM data yielded a classification accuracy of only 53.33%. In this analysis two of the three gossan samples and five of the twelve non-gossan rocks have been misgrouped. The low eigenvalue of the canonical discriminant function (Table 5.3), as compared to that from exposed surface, further suggests that the two data sets are less complimentary to each other.

Table 5.3. Eigenvalues of the canonical discriminant functions used for reflectance from cut, exposed and TM data.

Data	Eigenvalue	Canonical correlation
Cut surface (lab)	6.795	0.934
Exposed surface (lab)	2.009	0.817
TM data	0.033	0.179

5.3 Effects of Desert Varnish

Exposed surfaces of rocks in desert regions often contain desert vanish which, according to Bates and Jackson (1987), is defined as a thin dark shiny film coating, composed of iron oxides accompanied by traces of manganese oxide and silica, formed on the surface of rock fragments after long exposure. It is caused by mineral exudation of mineralised solutions from within and deposition by evaporation on the surface.

Analysis of the desert varnish by a scanning electron microscopy (Streoscan 360) shows that it is a thin, amorphous and translucent film that resembles a stain on rock surface. Spatz *et al.* (1987) described Fe, Mn, Si, and Al rich compounds to intergranularly penetrate the surface. It may consist of two or more layer-like features whose aggregate thickness may reach up to 25 μm. Each layer may be as thin as 1 /zm. The development of desert varnish is generally dependent on the mineralogy and texture of the bed rock, in addition to the environmental factors. The composition of the desert varnish varies with depth of the coating towards the bed rock, with Mn often concentrated on the outer surface and Fe being consistent throughout such coatings (Spatz *et al.,* 1987). These minerals are thought to generally account for 50-60% of the desert varnish.

The effect of desert varnish on Landsat TM data applications has been evaluated, in addition to reflectance measurements from exposed rock surfaces in the laboratory, by also conducting limited chemical analysis of the oxidized surfaces/desert varnish which involved the determination of Mn/Fe concentration. The chemical analysis was conducted by Dr. G. Matheis (Technical University of Berlin). This has been done by dissolving and filtering the desert varnish in a 50 ml nitric acid solution. Concentrations of iron and manganese were finally obtained by using the Atomic Absorption Spectrometry. The obtained results were treated in two approaches: statistical evaluations and interpretations of reflectance plots. Table 5.4 shows the obtained chemical results and some characteristics of the samples studied.

Statistical evaluation

In order to evaluate the effect of desert varnish in discriminating gossans and non-gossan rocks a four-group discriminant analysis has been carried out on reflectance laboratory data with step wise discriminant analysis using Wilk's Lambda. The groups consisted of samples from cut-gossans, cut-unaltered rocks, exposed-gossans and exposed-unaltered rocks.

The result shows that bands 4, 5 and 7 best discriminate the rock groups with an accuracy of 75%. In this analysis all the cut-gossans have been

Table 5.4. Manganese and iron concentrations of desert vamish/exposed surfaces, and some characteristics of the samples used for spectral analysis.

Sample #	Mn	Fe	Mn+Fe	Mn/Fe	Rock	Remarks
1	10.40	5.90	16.30	1.76	Gossan	Mn-rich
142	3.40	2.30	5.70	1.48	Gossan	brownish
144	10.60	7.20	17.80	1.47	Gossan	brownish
149	1.56	0.52	2.08	3.00	Granite	W-rich (dendritic)
188	4.64	4.39	9.03	1.06	Quartzite	ferruginous
183	2.88	22.60	25.48	0.13	Basalt	very minor alteration
167	6.13	10.80	16.93	0.57	Harzburgite	serpentinized, 6% Fe-oxide
176	3.53	31.00	34.53	0.11	Marble	white, sugary
208	17.30	142.00	159.30	0.12	Marble	grey, banded
206	1.60	1.60	3.20	1.00	Chlorite-epidote schist	minor alteration, 2% Fe-oxide
168	6.50	6.40	12.90	1.02	Olivine gabbro	serpentinized, 3% Fe-oxide
179	3.70	2.70	6.40	1.37	Tuff	light, fine grained, fresh
107	3.47	2.33	5.80	1.49	Graphitic schist	migmatitic, fresh
105	3.32	6.98	10.30	0.48	Amphibolite	slightly altered
181	3.84	7.38	11.22	0.52	Mica-quartz schist	chloritized, epidotized, mylonitized

correctly classified. Two cut-unaltered samples (harzburgite and white marble) have been misclassified as exposed unaltered rocks, and one exposed-gossan and one exposed-unaltered samples were misgrouped as exposed-unaltered and cut-unaltered, respectively. The result implies that the effect of desert varnish is variable for gossans and non-gossans, and it is significant for gossans permitting no spectral mixing between the exposed and cut varieties. The gossans are better discriminated from non-gossans in their fresh form, for obvious reasons, and may exhibit signatures similar to other rock types because of the oxidisation effects seemingly common to all.

Another attempt made to constrain the effect of desert varnish on the reflectance behaviours of rocks involved examination of the role of Mn/Fe ratio. Spatz *et al.* (1987) indicated that combined Fe and Mn and Fe/Mn ratios are genetically related to the underlying host rock. To this end a three-group step wise discriminant analysis was conducted for reflectance data from exposed surface; for gossans with a ratio greater

Table 5.5. Eigenvalues and variances of the two canonical discriminant functions used for groups based on Mn/Fe value.

Data	Eigenvalue	Canonical correlation
Exposed surface, F1	2.433	0.842
F2	0.044	0.206
TM, F1	0.749	0.654
F2	0.210	0.416

than 1, non-gossans with Mn/Fe greater than one, and those non-gossan rocks with a ratio less or equal to one.

On the obtained result a classification accuracy of 80% was achieved using TM bands 2 and 7. A W-rich granite and chlorite-epidote schist samples were grouped as non-gossans with Mn/Fe lower than 1 and higher than 1, respectively (Table 5.4). A graphite schist sample was misgrouped as gossan with Mn/Fe above 1. The result implies that although Mn/Fe ratio >1 does not necessarily correspond to gossan bodies, discrimination of such rocks from non-gossan rocks based on this ratio appears fairly possible. To this end a threshold value of -1.4 (see Table 5.4) would improve the classification result, with the possible exception of the above samples. For this purpose it seems that bands from both the VIS and NIR are best suited. The two canonical discriminant functions needed for this grouping are given in Table 5.5.

This procedure was also applied to Landsat TM data, based on the laboratory Mn/Fe values corresponding to each sample, to examine its comparability with the above results. Using bands 2 and 7 of the TM a classification accuracy of only 33.33% was obtained. The result further indicates the low degree of comparability of the two data sets, whereby less variation in laboratory data is explained by the TM data, as also shown by the large difference in their eigenvalues (Table 5.5).

Visual interpretation

The method of visual analysis, for investigating the effects of desert varnish on TM data, is based on interpretation of spectral plots of reflectance data from both cut and exposed surfaces of different rocks. Figures 5.7 & 5.8 show some of the spectral curves used for interpretation. For each rock sample the characteristics of the spectra from cut and exposed surfaces were examined and the following general inferences have been made.

Spectra obtained from both surface types mostly display a similar pattern. Spectra from exposed surfaces coated by desert varnish show reduction in reflectance, that increases from about 20% in the SWIR up to about 60% in the VIS range, as compared to those from cut surfaces. For light coloured rocks the overall difference between these two curves is often high, while the reduction in reflectance is relatively low for dark coloured rocks. Good examples are the reflectance curves from tuff (Figure 5.7a) or granite (Figure 5.7b) which display reflectance reduction of -30-75%, and basalt (Figure 5.8a) that exhibits a reflectance difference less than -20%, with decreasing wavelength. Mica-quartz schist exceptionally shows a reflectance difference less than 10% due to desert varnish in the VIS part (Figure 5.8f).

This feature is thought to be related to the overall maximum reflectance which is low for dark coloured rocks and higher for light coloured rocks, permitting lower and higher reflectance differences between those from cut surfaces and those with desert varnish, respectively. The strong reduction in overall reflectance in the VIS part is principally ascribed to the opacity of Mn-oxide that exhibits strong absorption in this part of the spectrum (Hunt *et al.,* 1971), in addition to the dark colour of the desert varnish that permits more absorption.

Due to the significant reduction in reflectance towards the VIS part of the spectrum, known absorption bands by iron-oxides in the range 0.4 - 1.0 gm by and large turn to featureless spectra, and are hardly retained on spectra of exposed surfaces. The steep fall-off the blue, characteristics of ferrous iron, is often removed. The intensity of this feature seems to be mainly governed by the rock type, mafic (dark) or acidic (light coloured). This is well illustrated by tuff (Figure 5.7a), granite (Figure 5.7b), and chlorite-epidote schist (Figure 5.8g) whose absorption bands in the visible region are turned featureless in case of surfaces with desert varnish. Mafic rocks generally show less reduction in reflectance in this part of the spectrum.

On the other hand, these absorption bands appear to be severely affected by the intensity of desert varnish development, which in turn is related to the Mn/Fe ratio (Table 5.4) that is of course governed by the composition of the underlying rock (eg. Spatz *et al.,* 1987). Spectral

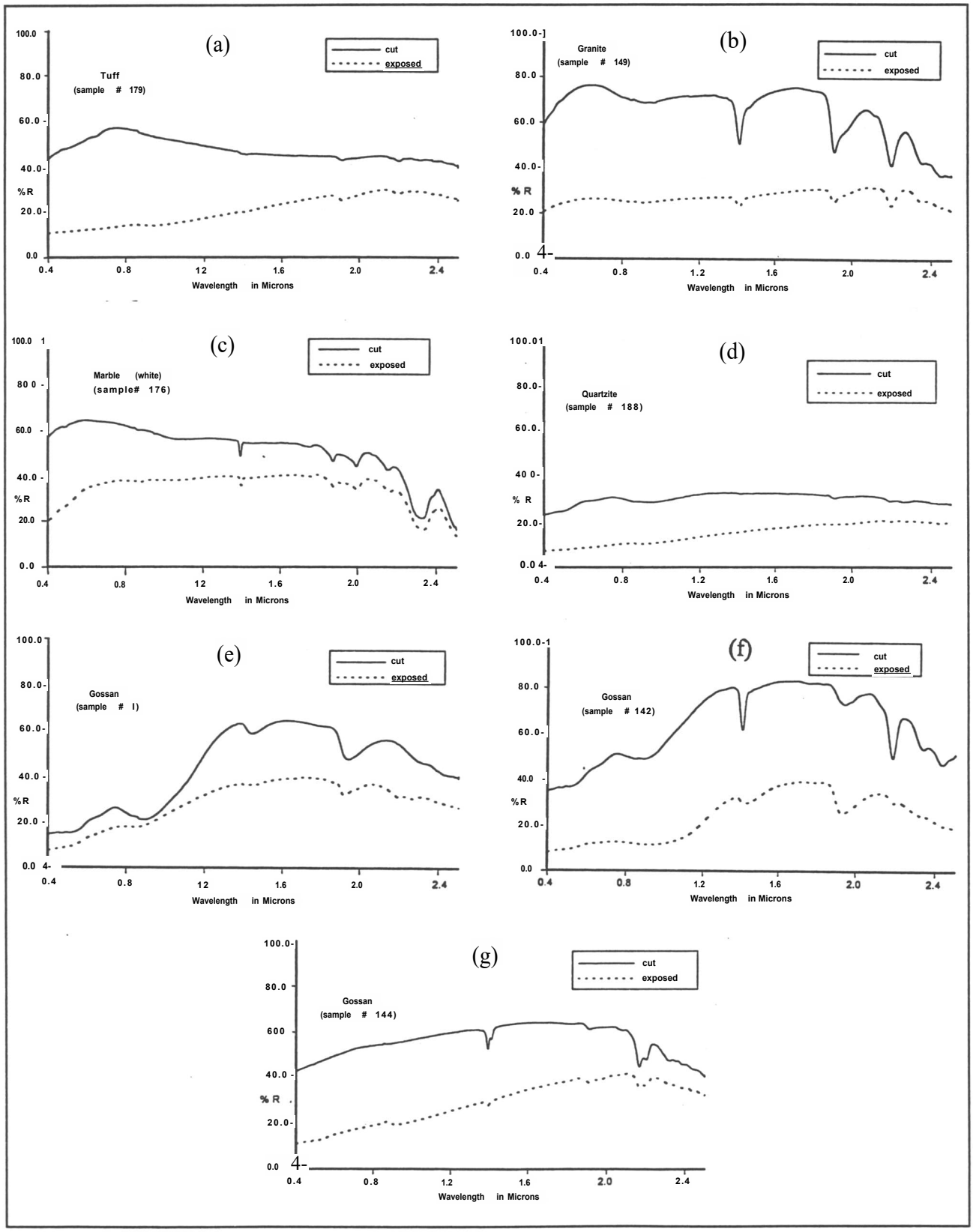

Figure 5.7. Reflectance curves of selected rock samples measured (in %) relative to halon, within the spectral ranges of the Landsat TM reflective bands. See text for explanations.

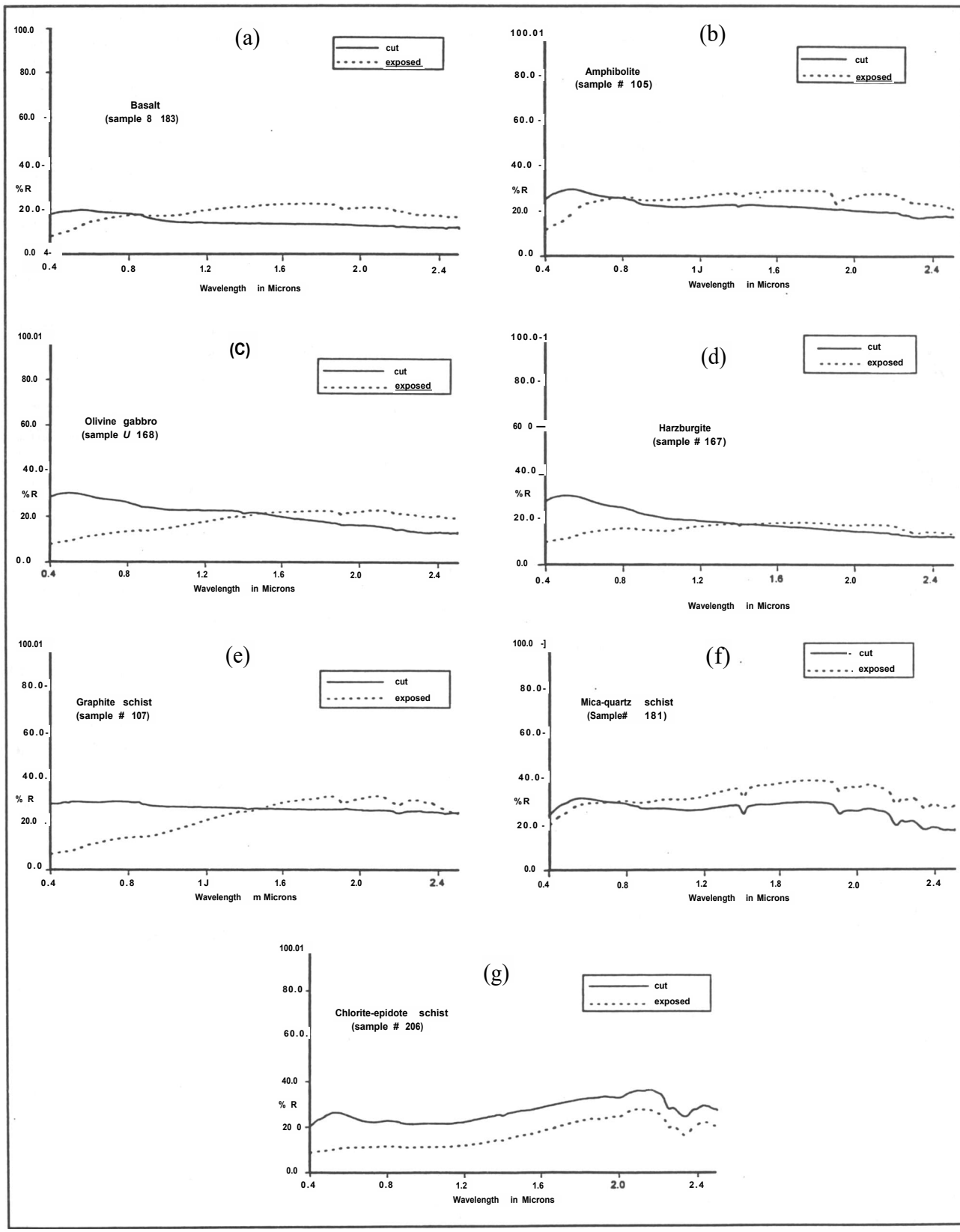

Figure 5.8. Reflectance curves of selected rock samples measured (in %) relative to halon, within the spectral ranges of the Landsat TM reflective bands. See text for explanations.

curves of some samples with high Mn/Fe ratio show remarkable flattening and broadening of absorption bands in the visible range (Figures 5.7 and 5.8). Gossan samples (Figure 5.7e and f), and granite (Figure 5.7b) very well display this effect. The practical consequence would be a significant colour bias in band or band-ratio composites involving those bands in the visible ranges along with "false" signatures which exaggerate absorption by "ferrous iron" concentration.

Spectral plots of exposed and cut surfaces of some samples appear to cross each other, i.e. reflectance from cut surface is higher in the visible range and that of exposed surface is higher in the SWIR ranges (Figures 5.8a-f). The spectral crossings occur, in the studied cases, between 0.7 *pm* (for mica-quartz schist, Figure 5.8f) and around 1.5 *pm* (for harzburgite, Figure 5.8d). Such spectral inversion has been related to contamination effects from grinding steel for particles of different size in the works of Hunt *et al.* (1971). For the present study this feature is ascribed to the mixed effect of composition, as it is displayed only by the mafic rocks (harzburgite, gabbro, basalt and graphite schist), and the overall opacity of manganese-oxide (Hunt *et al.,* 1971), which managed to significantly reduce the reflectance only in the VIS part.

According to Spatz *et al.* (1987) the higher reflectance of coated surfaces in the SWIR are related to the translucent compounds high in Si and Al in the desert varnish compared to the relatively higher absorption and low albedo of dark rocks. This relationship is consistent with the increased contribution of underlying host rock to the spectra of longer wavelength bands which penetrate to greater depth. Magnetite is also known to occur in many mafic rocks, and it is characterised by reducing absorption bands which results in spectral crossover in the VIS (Hunt *et al.,* 1971). Neither the individual concentration of Mn and Fe, nor their ratio, appears to explain this feature. However, these values are higher for mafic rocks indicating a conformable relationship with the formation of desert varnish (eg. Spatz *et al.,* 1987). The latter implies that high Fe/Mn ratio are associated with mafic rocks, and thus more development of desert varnish.

This phenomenon is well exemplified on the IHS image (Figure 4.1). On this image reddish colour that corresponds to gossans is displayed by other light coloured rocks like quartzofeldspathic schist because of the significant absorption in TM-1 due to the well developed desert varnish. Lyon (1990) also indicated comparable effect of desert varnish in acidic rocks, whereby absorption bands due to limonite near 0.9 *pm* and 2.2 *pm* occur. Similar effect of higher reflectance in TM bands 4 and 7 resulted in a yellowish colour for quartz gravels on the same image (SW).

In the NIR region the intensity of reflectance from exposed surfaces is less severely reduced, as compared to that of cut surfaces in VIS part, and absorption bands are often broadened, and partly removed. Towards the SWIR, however, the effect of desert varnish on reducing the overall reflectance of all the rocks is not only low, but the intensity of absorption bands characteristics of water, OH-bearing minerals, and carbonate radicals are certainly less sharp but hardly removed. Lyon (1990) indicated that reflectance from parent minerals penetrates through desert varnish in SWIR part only for those constituents having strong spectra (such as mafic rocks). Good examples are exhibited by gossans (Figures 5.7e-g), W-rich granite (Figure 5.7b), marble (Figure 5.7c), chlorite-epidote schist (Figure 5.8g) and graphite schist (Figure 5.8e). This conforms very well with the transparent nature of both manganese and iron oxides in these spectral ranges.

Spectra of the Derudeb gossans

Spectra of the Abu Samar and Malaket gossans of the Derudeb area have been considered here to describe their features since gossans are often good markers for sulphide and gold mineralisations. Figures 5.7e-g show the reflectance plot of gossan samples from the Derudeb area.

The reflectance curves obtained from the cut surfaces of these gossans are characterised by a common and fairly broad absorption bands around 0.55 *pm* that is ascribed to ferrous iron. Another

major absorption band is centred around 0.9 /zm caused by ferric iron, with a moderately steep rise in slope towards higher wavelength. These features, therefore, display very well the iron enrichment of the gossan as it commonly occurs through oxidation of sulphides and the leaching-out of sulphur and other metals. Buckingham and Sommer (1983) also reported the same absorption bands in ferric iron-bearing gossans. As discussed above, these absorption bands are almost missing (Figures 5.7c and g) or much broadened (Figure 5.7f), and the slopes are apparently gentle, for reflectance curves from gossan samples with exposed surface.

Prominent absorption bands near 1.4, 1.9 and 2.2 /zm are very well related to water and hydroxyl-bearing group of minerals. These bands characterise the hydrated iron-oxides and sulphates that have possibly been left-behind after the leaching-out of sulphur. Limonite is one such hydrated iron-oxide that most likely occurs in such rocks (and Lyon (1990) also ascribed absorption bands around 2.2 /zm in desert varnish to limonite). It is also known that OH' vibrational overtone and Al-OH bending mode are responsible for these absorption bands in gossans (eg. Buckingham and Sommer, 1983). On the reflectance plots from exposed surfaces these absorption bands are less sharp and less intense, but still well prevalent.

Penetration of electromagnetic energy within the TM spectral range was studied by Buckingham and Sommer (1983), who concluded a maximum penetration of 50 /zm for pulverised samples. If this value is also considered for the samples studied, it is apparent that parts of the reflectance represent the mineralogy of the rock surfaces. It is this part of the reflectance, which generally increases with increasing wavelength, and that helps in giving the gossans a seemingly different and characteristic signatures.

On the IHS-transformed image obtained from bands 7, 4 and 1 in R, G and B, respectively, it has been mentioned that the gossans are in intense reddish colour (Section 4.8.5). The spectral plots (Figure 5.7e-g) show that the characteristic absorption bands in SWIR range are still retained, and in exposed gossans the reflectance in this band range is higher than those from VIS and NIR bands for the same rocks. In effect TM band 7 remains to be the dominant reflector-band, and thus the reddish hue in this composite.

6 Application of a Geo-Information System (GIS)

6.1 Introduction

Geo-Information System (GIS), also known as "geomatics" (eg. Laurini and Thompson, 1994) is a rapidly advancing computer-based technology where information is organised, analysed, and presented with reference to space. It is distinguished from other information storage and retrieval systems by its use of locations of features in a two-dimensional co-ordinate space as the fundamental referencing principle and as the important variables in quantitative analysis. GIS is a means to an end, and its value lies in how it helps one think differently about the way spatial information is organised or logically linked, combined, understood and used for inferring meanings. In addition to spatial considerations GIS structure also involves integration of thematic dimension such as the different characters or properties of each entity or location and its relationship with others, that are used for assessing data patterns and interactive query.

A GIS structure commonly consists of five major sections: data input, management, processing, analysis and modelling, and data output (Laurini and Thompson, 1994). Since data used in GIS are often from different source, and thus different qualities, a GIS should provide the tools and method for the integration of these data into a format which allows the data to be compared and interrelated. After data are collected the GIS must provide facilities which can integrate, contain and maintain the data along with proper access. Data processing involves operations performed on the data to produce information, whereas data analysis deals with the quantitative and qualitative interpretation of the data. The data can then be modelled using known relationships, and the outcome of a set of conditions, and finally presented in different output formats.

Where data are observations made from monitoring the real world, and are related to the elements and physical processes that operate in it, their representations define models. Geographic models generally address three dimensions of data realisations: the spatial, thematic and temporal dimensions. The first one refers to the location of an object, the second deals with the character of either the location or the object, and the third dimension points to the comparison of data over time. While points, lines, areas, surfaces and networks are different entities, their locations represent a spatial dimension in the real world. Attributes are characteristics of an entity or its location, and are composed of the unique identifiers and the geometry of spatial entities, the spatial relationships between entities and their other properties. Based on the scale and type of measurement or observations made, attributes may be in ordinal, interval, ratio or nominal form (Laurini and Thompson, 1994).

In spatial data representations and analyses there are two major models: the vector model and raster or grid model. As the most common method of spatial data representation the vector model describes location as x, y co-ordinate pairs that are fundamental building blocks from which spatial entities such as points, lines, and areas are composed. In such data structures 2-D space is assumed to be continuous and it allows very precise representation of locations, distances and areas. Furthermore, attribute values for point, line, and polygon entities are typically stored independent of the entity's spatial representation.

According to the grid model the real world is represented by a mosaic of two-dimensional array of cells or matrix with definite shape, and arranged in a grid of rows and columns. Each grid cell represents a square or rectangular portion of the earth and it is assumed to have one value for any given attribute. The resolution of raster data is represented by the size of cell on the ground. Thus, such data represents a discrete space where the location precision is dependent upon the size of the grid cell. For smaller grid size (higher spatial

resolution) greater data volume is required to store the representation of an area. The advantages of grid structure includes the ability to represent continuous surfaces, and the ability to store points, lines, polygons and surfaces equally. The hierarchial Quadtree and Octree models are well known in grid based data structures. The choice of a particular type of data representation should consider the involved data volume, topology and spatial query, extent of data generality, analytical capability, and the required accuracy and precision. Almost all available GIS softwares permit conversion between these data types.

Most GIS applications involve discrete features that are described by the attributes related to a thematic data, in addition to their representation in 2-dimensions. Continuous features, that are not spatially discrete and transition between values is not abrupt, on the other hand, can also be represented as surfaces. The Triangulated Irregular Network (TIN) is a functional surface representation of data that consists of adjacent, non-overlapping triangles computed from irregularly spaced points with x, y co-ordinate and a z-value. Lattice, as another model of surface representation, consists of an array of equally-spaced mesh points in x-y direction that are referred to a common origin.

The ability to integrate, manipulate and process data from different sources in order to provide information and facilitate understanding through visualisation and generalisation, among others, make GIS a very powerful tool. Digital images, as one of the commonly used raster data, can be well integrated into GIS database. Analogue data can be automated and also integrated with several other data on a common coordinate (often plane rectangular) system. The different data types may then be related as required, visualised, analysed and generalised for physical representation of the real world.

For the present work various data types, from different sources, that individually constitute part of the spatial information system pertaining to the Derudeb area have been used. In the next sections the basic data characteristics, followed by database management, processing, analysis and interpretation will be considered. Geophysical data available to this work were obtained in a form of Bouguer, residual and aeromagnetic data grids. No information was supplied concerning the regional field removed to produce the residual anomalies.

6.2 Data Characteristics

Gravity data

Regional gravity survey over the Red Sea area was conducted by the Technoexport (between 1971 and 1974) project. According to this work base gravity stations were established using a central system by means of repeated measurements of differences relative to the main station. The base net has been referred to the level of International Gravity Network Station in Khartoum. The error in determination of co-ordinates of the gravity station was ±1.5 km, and 1.5 m for heights, by using air photo (1 : 40 000) mosaics. Accuracy of gravity value on main base station ranges between ±0.14 and ±0.06 mgal for OVM pendulum and GMT gravimeter, respectively.

According to Technoexport (1974) field gravity data were measured with a mean square error of ±0.25 mgal, whereas for the Bouguer anomaly the value was at ±0.65 mgal. Normal field was computed using the International Formula of 1930 assuming an average rock density of 2.67 g/cm^3. The observed gravity values were then subjected to Free-air and Bouguer correction, whereby a predetermined value of ±0.5 mgal were used for latitude correction. No terrain correction was employed for lack of topographic maps of reliable quality. Gravity values on topographic maps with plotted gravity stations were compiled at a scale of 1 : 250 000. Final Bouguer gravity contour maps then were produced with an interval of 2.5 mgal at the scale of 1 : 500 000.

Aeromagnetic data

An aeromagnetic survey of the Red Sea area was also carried out by the Technoexport (1974) project with heights streamlining the relief, and along sub-meridional profiles spaced at an interval of 1940

±120 m. Magnetic field intensity was continuously recorded by AMM-13 magnetometer mounted on IL-14 aircraft. Absolute intensity values were discretely recorded by an aircraft proton magnetometer Jap-I, and an SMB-2 instrument recorded the magnetic variations. For adjustment of measurements obtained during the survey a base-control-net was established. Accuracy of the survey, as checked by a system of control profiles flown over the calm field, was ±12 gamma. No information is available over diurnal correction. The magnetic isolines, representing the total field, have been initially compiled at the scale of 1 : 250 000, and finally at 1 : 200 000 scale using a contour interval of 50 gamma. The latter has been used by this work. All cartographic works pertaining to the geophysical data were done in UTM co-ordinates using Clarke-1880 projection.

Topographic data

Six topographic maps, each at 1 : 100 000 scale, covering the Derudeb map-sheet (NE 37-1) produced in 1982, were obtained from the Sudan Survey Department. The topo maps are known by the names Mahattat Derudeb, Dilay, Dibal Tuluqweb, Khor Lanqeb, Jibal Adar Ribad, and Jibal Teluk. The contour interval is generally 40 m, with an interval of 20 m over flat areas. The maps also contain Universe Transverse Mercator (UTM) grid co-ordinates produced by projection using the spheroid of Clarke 1880. The topographic maps have also been used for geometric rectification of the Landsat data (Section 4.1.1).

6.3 Database Organisation

The database has been organised such that each data type represents a thematic layer related to a particular information type. This helped distinction of themes having the same feature types, and also permits combination of different features (eg. points and lines) corresponding to a particular theme. In this regard the following 7-themes have been identified: Bouguer gravity, aeromagnetic, residual gravity, topographic, lineament, geologic, and observation points. The first five data types contain line features, whereas the last two are composed of polygon and point features, respectively. All the coverages have been made equally accessible and the UTM co-ordinate, with the spheroid of Clarke-1880, has been selected for registration of all data.

Additional descriptive data or attributes such as rock names corresponding to GPS-reading locations were then appended to the respective coverages (eg. lithology, based on thin-section studies) through look-up tables related by a common item. The same item has been appended to the geologic data. This type of relational data representation has been preferred over others because of its simplicity for data organisation, flexibility to join tables as required, and non-procedural style for accessing data. These conditions also permit expression of queries in terms of what is needed rather than how to get the data to answer the question posed (Laurini and Thompson, 1994). The processing, visualisation and interpretation of the different data has been initially made separately for the different data types, and then for merged data sets as needed.

6.4 Data Processing

For the purpose of data integration and visualisation, geophysical, topographic, and geological data pertaining to the Derudeb area have been processed using ARC/INFO (7.02) software installed on SUN SPARCSTATIONS. Bouguer gravity (1 : 500 000), residual gravity (1:1 000 000) and aeromagnetic (1 : 200 000) contour maps produced by the Soviet based Technoexport (1974) were provided by the Geological Research Authority of Sudan (GRAS). Furthermore, topographic maps at the scale of 1 : 100 000 were also obtained from the Sudan Survey Department, and a geological interpretation map and a lineament map, both at 1 : 170 000 scale, produced by this work have been made available. All the above mentioned data were encoded using a DIGIPAD/ GTCO 16-4800 digitizer.

In order not to further reduce the already low precision, and also save memory space, the spatial data have been principally represented and processed in a vector format. The general

processing steps adopted for the above vector data are analogous, and generalised in Figure 1.2. All coverages were automated and edited for possible errors. Since the data are of varying scale, and thus varying accuracy, different tolerance levels of the Root Mean Square (RMS) error has been adopted. Accordingly RMS error of 200 m, 100 m, and 400 m for Bouguer gravity (1 : 500 000), aeromagnetic (1 : 200 000) and residual gravity (1 : 1000 000) anomaly data, respectively, have been used. For topographic data (1 : 100 000) the RMS error was kept at 20 m, whereas for geologic and lineament data (1 : 170 000) the values have been limited to 30 m preventing the total error (with *ca.* 60 m from the Landsat data) to exceed ~100 m. While in all cases the available isolines have been digitized, the topographic data have been generally encoded at an interval of 40 m, except along steep slopes where 80 m interval has been considered.

Except for the geologic and lineament data which are polygon and line coverages with discrete data, respectively, the other line coverages representing continuous data were further processed for better visualisation. Initially, points with interpolated values were manually inserted into closed-high or closed-low isolines in order to avoid flat-tops and flat-lows, respectively, and approximate natural conditions. Additional item was appended to the databank under which the corresponding Bouguer gravity, aeromagnetic, residual gravity and elevation data of each isoline have been stored.

Following the building of topology for the different features contained in a coverage, whereby the new geometric, relational and other information are reconstructed, all the data have been transformed to a common UTM co-ordinate system using the spheroid of Clarke 1880, in conformity also with the Landsat data (Section 4.1). For the topographic data the six separate sheets were to be joined, and then checked for continuity of isolines along boundaries, to produce a single composite map.

Triangulated Irregular Network (TIN) was then generated for each coverage using the item containing the data values corresponding to both line and point features. In all cases the Z-factor has been kept to be one, avoiding unnecessary exaggeration of the data values at this stage. For Bouguer gravity and aeromagnetic data the proximal-tolerance (distance determining the points and nodes to be ignored in weeded vertices) and weed-tolerance (which governs the maximum distance between vertices for smoothing/ generalisation of arcs) have been kept at 10 m and 20 m, respectively. This is expected to permit the retention of high density of vertices. In the case of residual gravity anomaly these values were increased to 50 m and 100 m, whereas for topographic data they have been kept at 5 m and 10 m, respectively.

The TIN to Lattice conversion was then conducted for the different coverages using a distance of 30 m between mesh points, although larger distances yielded no inferior results, in conformity with the resolution of Landsat TM. In order to achieve a visually optimal contrast exaggeration of the z-values has been found necessary at this stage. In this regard a z-factor of 100 has been used for both Bouguer and residual gravity data, and a z-factor of 10 was found to be optimal for both topographic and aeromagnetic anomaly data. It is worth mentioning that during the Lattice generation a "quintic" interpolation of the z-values has been preferred to the "linear" one, in order to closely approximate the real-surface through smoothing, because of the already sparse nodes at these scales.

By applying user-defined ranges to the regularly distributed lattices of Bouguer gravity, residual gravity, aeromagnetic anomaly and topographic data, the corresponding polygon coverages were generated through look-up tables. These coverages were then checked for anomalous isolines often with peaks, which result from interpolations during TIN generation, and were accordingly edited. Shaded-relief coverages of the Bouguer gravity and topographic data have been produced from the lattice coverages using the actual data, by avoiding the possible effects from the "shadow" induced by the azimuth and altitude values. In this exercise the azimuth and altitude values should be optimised, since higher altitude result in over-exposure and vice versa, and azimuth values between 270° - 0° and between 0°- 90° yield inversed relief of the geo-data. An azimuth of 40° has proven optimal for all

the surface generation. Finally the polygons were transformed to a grid format for further processing and data presentation.

In addition to the above procedures of data conversion and presentation the aeromagnetic and gravity data were also subjected to some processing steps commonly performed on image data. These type of processing are expected to enhance features not explicitly observable on the conventional contour maps that often smooths the data and may result in loss of structural details. This approach generally involved extended gray value ranges (up to 256), local contrast stretching, directional filtering and PCA following steps described in Section 4. Similar processing methods have already been used for geological application by some workers (eg. Kowalik and Glenn, 1987; Drury, 1993).

For the geologic and lineament maps produce by this work, the encoded data were transformed to the UTM co-ordinate using the spheroid of Clarke-1880. The transformation was done by adopting the same ground-control-points employed for the rectification of Landsat data (Section 4.1) and also obtained by GPS readings. This was followed by further checking of the conformity of geological boundaries and lineaments with the Landsat image, whereby a number of ground control points were used to readjust the former against the latter through "rubber-sheeting", thereby reducing the possible error introduced during processing. The more number of ground control points used, the better the result would generally be. Since the final mapping was supposed to be produced at a scale of 1 : 250 000 all geological units (polygons) less than 1 km^2 were then omitted from the original map. Similar processing steps have been adopted for the lineament map of the Derudeb area.

Location of observation points obtained from GPS measurements in the field were prepared in ASCII format and added to the database. These were further related to the lithology occurring at that particular location as obtained from thin-section study.

6.5 Data Analysis and Interpretation

For geological study of the Derudeb area using the different data types in GIS a map overlay modelling has been adopted, for it simplifies association of different themes for visualisation. Considering the relationships between the available data types the following pairs of combinations have been produced for analysis: Bouguer gravity anomaly and geology, Bouguer gravity anomaly and lineament, aeromagnetic anomaly and geology, aeromagnetic anomaly and lineament, residual gravity anomaly and geology, and topographic data. Furthermore, the Landsat TM image (composite 7 4 1 in R G B) was draped over the aeromagnetic and gravity data not only to see the possible relationships between these data types in geologic context, but also to improve the geologic interpretation of the existing data through better visualisation. The latter is also expected to provide more information as compared to the separate individual data (eg. Kowalik and Glenn, 1987). Locality names used in the following sections are shown on Figures 6.1 and 6.2, and explanations to the geological symbols[1] used are given below. A more regional integration of the geophysical, topographic and Landsat data for the most part of the Red Sea Hills is given in Ott (1997).

6.5.1 Aeromagnetic data

Magnetic susceptibility is the fundamental parameter that is measured in magnetic prospecting. It generally represents a response from the near-surface crust of the Earth and depends on the local amount of magnetic minerals contained in the rocks. That means, rocks enriched by magnetic minerals generally give higher magnetic response than those

[x]Key to geologic symbols used in Figures 6.1 and 6.2. Qt = Quaternary sediments, Av = acidic volcanics, Bv = basic volcanics, Sd = sedimentary rocks, Ap = acidic plutons, Bp = basic pluton, Vs = metavolcano-sediments, Gn = gneiss.

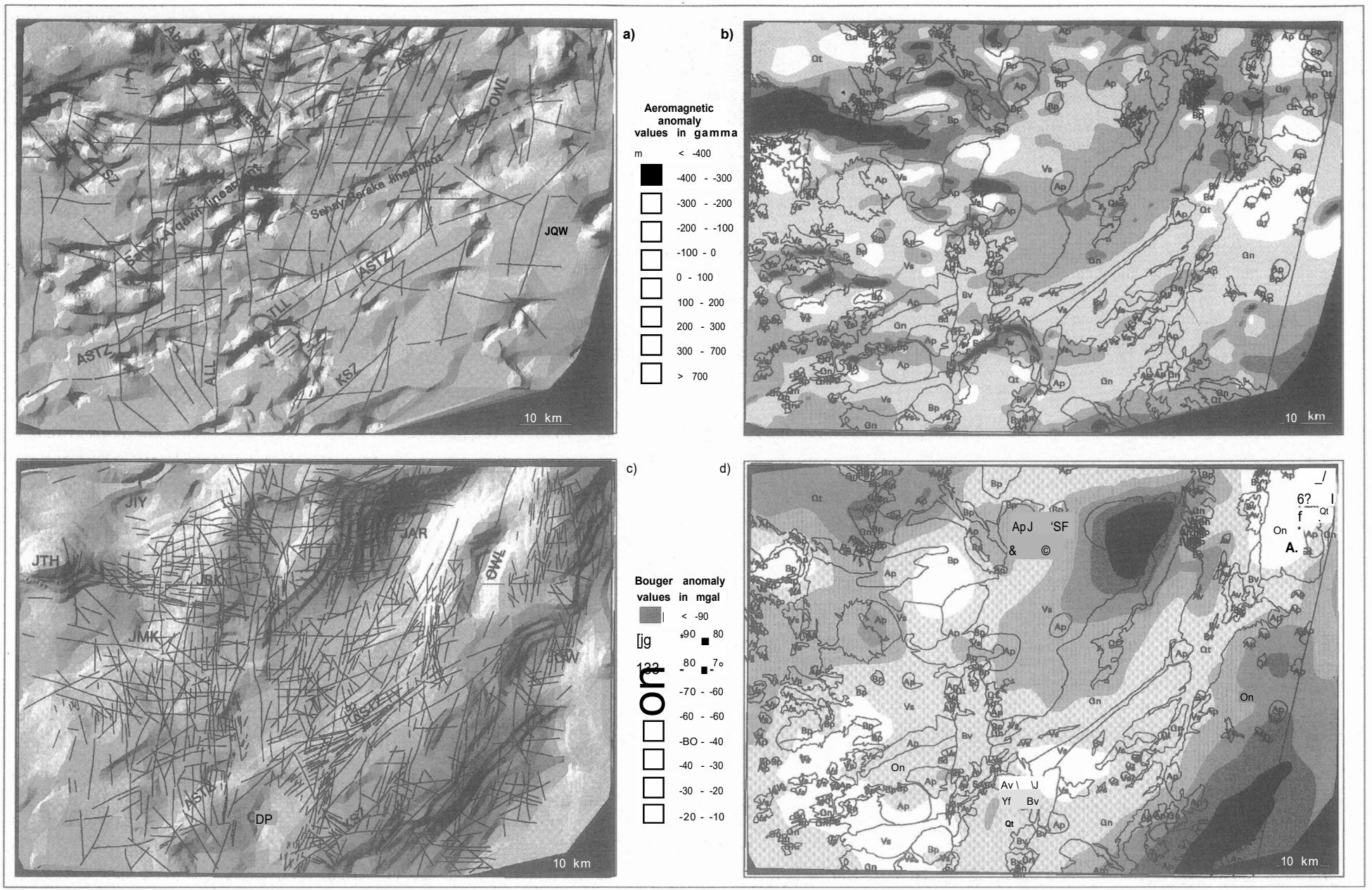

Figure 6.1 GIS modelling of aeromagnetic and bouger gravity data: (a) and (c) show a pseudo-relief representation of aeromagnetic and bouger gravity anomaly overlain by lineament map, respectively (azimuth - 300°, altitude = 40 ^{s} and z-factor = 10 for (a) & 100 for (b>. The same are respectively shown in (b> & (d)«using user-defined ranges and overlain by simplified geological map. JTH=J. Tihilla, JIY=J. Iyub, JMK=J. Malakat, JAR=J. Arqawi, JBK=J. Bakabne, JQW=J. Qawayateb, OWL=Osir Walab Lineament, KSZ= Kibirit Shear Zone, TSZ=Tihilla Shear Zone, ASTZ=Adadi Shear & Thrust Zone, ODP=Odi depression. Brocken lines show inferred possible lineaments. Area is same as in Figure 6.2.

containing few or no such minerals. Telford *et al.* (1976) gives sufficient details on the magnetic method.

The aeromagnetic anomaly map of the Derudeb map sheet falls within the Southern Province of a three-fold classification adopted for the RSH by Technoexport (1974), with intensities ranging between 1000 and 700 gamma. It is characterised, as a whole, by two distinct magnetic fields: a mosaic of strongly differentiated field complicated by numerous local anomalies, and a quite field predominated by large anomalies. The former are often distinguished by their low intensity (<50 gamma) and small size (3-5 km) whereas the latter are characterised by amplitudes of up to ±100 gamma and large size (15-20 km). In addition, there are areas in which linear anomalies predominate, and parts by and large remarked by dipole anomalies. Figures 6.1a and b show a pseudo-topographic and polygon representations of the aeromagnetic anomaly data overlain by major lineaments and generalised geological map of the area, respectively.

J. Tihilla in the NW displays a conspicuous magnetic anomaly with remarkably steep gradient that extends for over 50 km in the WNW-ESE direction (Figures 6.1a and b). This feature is interpreted to be related to the relatively dense sublatitudinal fracture and dike systems thought to have controlled the emplacement of the ring complex (Section 2.2.2). Their deep-seated nature is evidenced by this vividly seen pattern on northern and southern sides of the granite, since the form of magnetic contours is often determined to a large extent by the structural trends in the basement rocks, reflecting buried structures not related to the surface geology (Griffiths and King, 1981).

A similar E-W trending negative magnetic anomaly of about 20 km long is to be seen in the SW close to J. Sanay (compare Figures 4.1 and 6.1a). Here the high-positive anomaly is apparently underlain by gabbroids, but the structure is rather interpreted to be associated with deep-seated fault along which the pluton was emplaced, as also seen from its elongated shape. A comparably intense anomaly with steep gradient occurring just to the N is thought to be related to similar structure. In the area NW of J. Arqawi a well resolved negative anomaly as long as 10 km is easily seen from the map (Figures 6.1a and b). This feature is ascribed to be the ductile Arqawi Shear Zone (Section 2.2.4). A similar pattern of magnetic field is displayed along Tashalal-Langeb Lineament (central S). On the other hand major faults related to the Cenozoic rifting and volcanism appear to have been hardly resolved by the magnetic fields, including other Pan-African faults that run nearly submeridional. This is may be ascribed to the resemblance in magnetic susceptibility of the rocks on either sides.

Major aeromagnetic anomaly patterns of several kilometres long have been interpreted in the Derudeb area (discontinuous lines on Figure 6.1a). Two such structures trend NE-SW and have been identified as Sanay-Arqawi and Sanay-Baraka lineaments. These lineaments are not seen on the Landsat images and they most probably correspond to deep-seated structures that were developed with the Pan-African accretion tectonics that prevailed in the area, since they also trend nearly parallel to the ATTSZ. The Abu Samar Lineament strikes NW-SE and appears to join a fault in its southeastern extension. This feature may also be ascribed to mafic rocks at depth, in view of the significant density variation against the surrounding upper crustal rocks.

In the southeastern part of the map-sheet broad (over 15 km) positive aeromagnetic anomalies with low amplitude (up to 100 gamma) and predominantly gentle gradients are prevalent. An interesting feature in this area is a linear like pattern that can be traced continually from SW to NE. The structure apparently fits very well with the location and trend of the Adadi Thrust and Transpressional Shear Zone (Figure 6.1a) whose northern part is demarcated by the late D_3 thrust fault (Section 2.2.4). The ATTSZ is seemingly well resolved by a northward decreasing susceptibility. Furthermore, this structure explicitly marks the boundary between the highly differentiated anomaly pattern in the north from the quite and large field in the south (see above).

This observation, therefore, reinforces the geological interpretation, and corroborates the suggestion that the possibly older gneissic rocks (to the S) and the Pan-African sequence (to the N) are demarcated by this shear zone. Lineament patterns

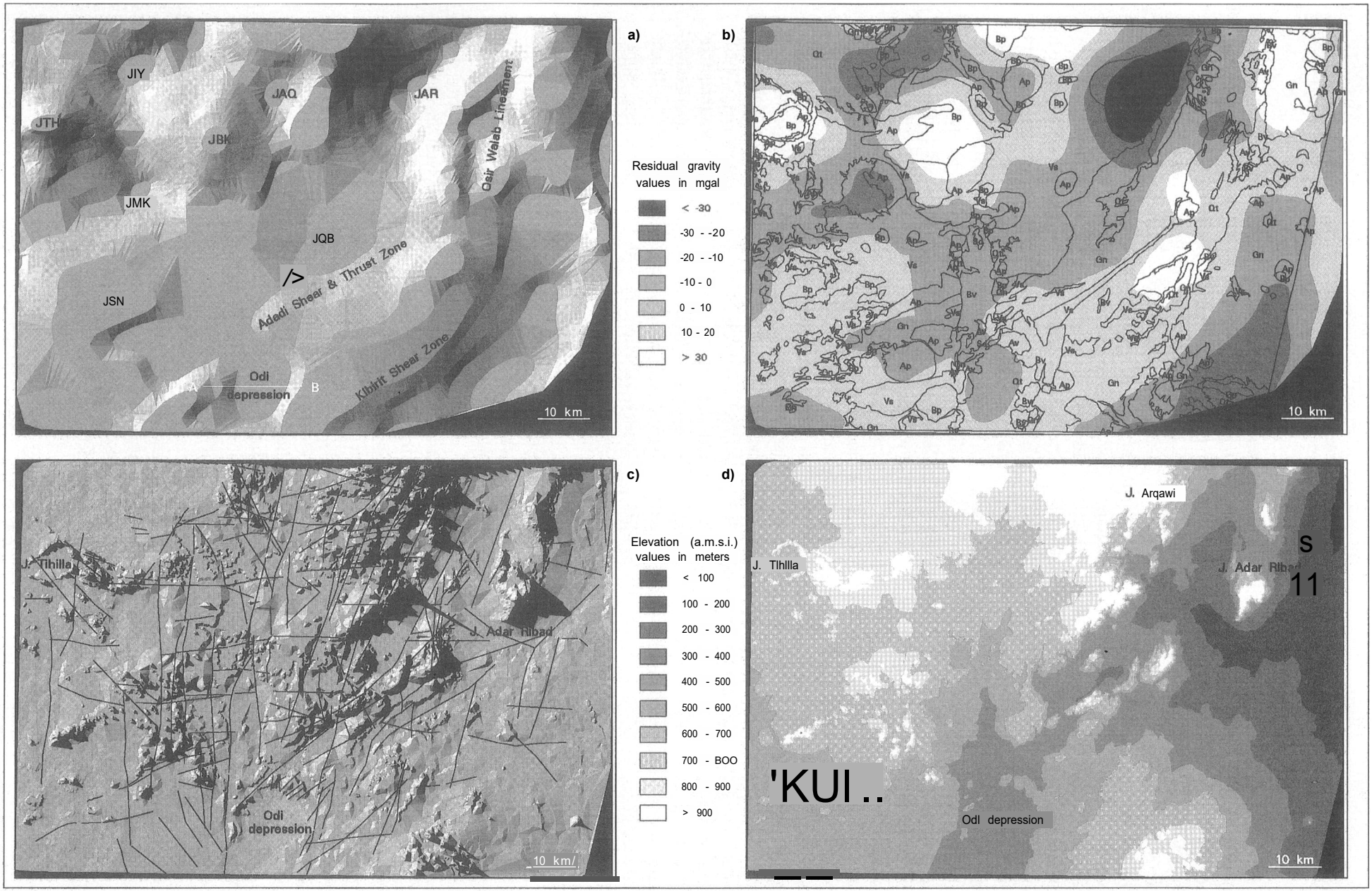

Figure 6.2 GIS modelling of residual gravity and topographic data, (a) shows a 3-dimensional representation of residual gravity anomaly, and <c) is a perspective view of the Derudeb area, (bi & (d) are representations of (a) & (c) in value ranges, respectively, (b) & (c) are overlain by simplified geological and lineament maps, respectively. Azimuth = 300°, altitude = 40°, z-factor = 100 for (a) and 10 for (c). JTH=J. Tihilla, JIY=J. Iyub, JAQ=J. Arqawi, JBK=J. Bakabneb, JMK=J. Malakat, JAQ=J. Aqarta, JSN=J. Sanay & JQB=J. Qubuliteb. A & B join the line of cross-section shown on Figure 6.3. Figures correspond to Derudeb area (36°00'E 17°00'N - 37°30'E 18°00'N). See text for explanations.

discernible in these two sectors fail to reveal such a relationship, for they were primarily products of D2/D3events (syn-to post-collisional) that have been witnessed in the whole region.

Dipole anomalies in the area are apparently widespread, and invariably display their maxima S of their conjugate minima. This may be ascribed to induced magnetization along a direction close to the present day inclination, which possibly resulted in the absence of longitudinal anomalies. Since many such features are related to single magnetic bodies that are below the line of inflection (Telford *et al.,* 1976) similar interpretation may be valid, with care, for the Derudeb area.

It is worth mentioning that the aeromagnetic data that was processed by image enhancement techniques yielded substantial improvements in recognising major structural features that are less obvious on the contour maps. Spatial filtering of the data apparently gave better result in visually detecting the structural features, although gray value stretching also produced a good representation of the dipole anomalies. This is valid for most of the major shear zones and faults in the area. The advantage with this way of data representation, as compared to the surface modelling (Figure 6.1), is that major structural features are sharply represented, making delineation of tectonic boundaries easier.

6.5.2 Gravity data

Measurement of the gravitational field of the Earth are generally influenced by several factors and should be corrected for variations in latitude, elevation, topography, earth tide and effect of isostasy in order to reduce the values onto some datum equipotential surface such as the geoid (Telford *et al.,* 1976). The gravity data for which these corrections have been made represents the Bouguer anomaly. This anomaly represents the lateral and vertical density variations in the Earth's crust, which intum are related to the underlying rock types and the constituent minerals. Generally, dense/compact rocks exhibit higher Bouguer anomaly than less dense rocks. The removal of 'regional' anomalies caused by deep-seated structures yields a 'residual' gravity which often symbolises the local anomaly. Details over the characteristics and processing of gravity anomaly data are given in standard geophysics books (eg. Telford *et al.,* 1976; Griffiths and King, 1981).

The Derudeb area is generally characterised by exclusively negative Bouguer anomaly values ranging from -90 mgal around J. Arqawi in the NE to -10 mgal around the NE corner of the map-sheet (Figure 6. Id). Generally, two types of local gravity fields have been identified in the area: the roughly rounded and isometric anomaly, and the linearly elongated anomalies. The former are displayed often by very low gravity anomalies that correspond very well to acidic igneous intrusions, because of their obviously low density. Good examples in the area include the granitic bodies E of J. Malaket (central W) and around J. Aqarta (central N). Similar features are exhibited by J. lyub (far NW) and J. Lanqeb (central), but at a lower intensity.

In the W, the post-orogenic Tihilla ring complex is characterised by relatively higher (-25 mgal) gravity values in its central part corresponding to the gabbroic body, and Bouguer gravity minimum (up to -50 mgal) that is related to the rimming granite. Furthermore, a gabbroic body rimmed by a granite occurring E of J. Qawayateb, as interpreted from Landsat images, is well displayed on this anomaly map (Figure 6.1c) in a similar fashion.

The most conspicuous feature, however, is displayed by J. Arqawi (N) with Bouguer anomaly values ranging from -90 mgal in the centre to about -55 mgal at the periphery of a syn-orogenic granite. Basic plutons around J. Sanay (SW) and J. Bakabneb (central W) show relatively higher gravity values than their surroundings but appear to be generally less resolved unlike the one N of J. Adarit (NE). Figures 6.1c and d show a 3-dimensional model and a polygon representations of the of Bouguer gravity anomaly overlain by lineaments and simplified geological maps, respectively.

Narrow and elongated Bouguer gravity anomalies are often related to steep contacts between rocks of different density, possibly due to fault systems (eg. Griffiths and King, 1981). A very low (up to -65 mgal) gravity anomaly with high gradient in the NE is accordingly ascribed to the

NE-SW running Osir Walab Fault, that bounds the nearby rhyolite to the E and predominantly basement rocks to the W, and being obscured under unconsolidated Quaternary sediments. Further to the E (along J. Adar Ribad) the basalt mantle over the basement rocks appears to be characterised by a relatively higher gravity field. Towards the Baraka Suture the gravity anomaly decreases with moderate gradient, possibly depicting its reactivation as normal fault with down-throw side to the E (see Figure 2.6).

Another interesting regional feature to be seen from the Bouguer gravity data is the NE trending pattern of broad and elongated gravity anomalies with moderate gradient. One such low anomaly exists around Kibirit Shear Zone (Figure 6.1a), in the area dominated by gneissic rocks, extending all the way to the northeastern comer of the map area. To the N a horst-like pattern is exhibited by the higher gravity values close to the Adadi Thrust and Transpressional Shear Zone (Figure 6.1c), the latter being correlative to the "zone of increased horizontal gradient" thought to separate very large anomalies from regional ones (Technoexport, 1974). The steep gravity gradient in this area may be ascribed to deep-seated structures that mark the old continental margin sediments (graphite schists, marble, quartzite et.) from the dominantly quartzofeldspathic gneisses of possibly continental character (Section 2.1.1).

In the central part of the map area (around J. Qubuliteb - J. Arqawi) the NE trending pattem exists but with low amplitude. Further N and NW, however, this regional feature is absent and rather locally differentiated gravity highs and lows prevail. It is thought that this pattern of gravity anomaly is a manifestation of the possibly different crustal blocks of the southern high-grade gneissic rocks and the northern relatively juvenile volcano-sedimentary sequence. This interpretation corroborates the geological and aeromagnetic interpretation (Section 2.2.5, 6.5.1), as trends of gravity and magnetic anomaly are helpful in discriminating distinct crustal blocks (Wellman, 1985).

In the central-southern part of the Derudeb area, the Odi depression is represented by a gravity low of -50 mgal against a relatively high of -36 mgal along its margins. The low gravity gradient may seem to have not resolved the underlying rift structure, however, using 3-dimensional modelling the rift basin can be better visualised (Figure 6.1c), as also evidenced from Landsat data (Section 4.6.2). Figure 6.3 shows a cross-section along the Odi depression using Bouguer and residual gravity data.

An attempt made by merging the lineament map and the gravity data shows that the northeasterly trending lineaments in the gneissic area (domains IV and V in Figure 2.7) are in fair agreement with the gravity anomaly pattern in the same sector. In the western part of the map-sheet the fairly equally prominent N-S and E-W trending lineaments hardly fit with the gravity anomaly data.

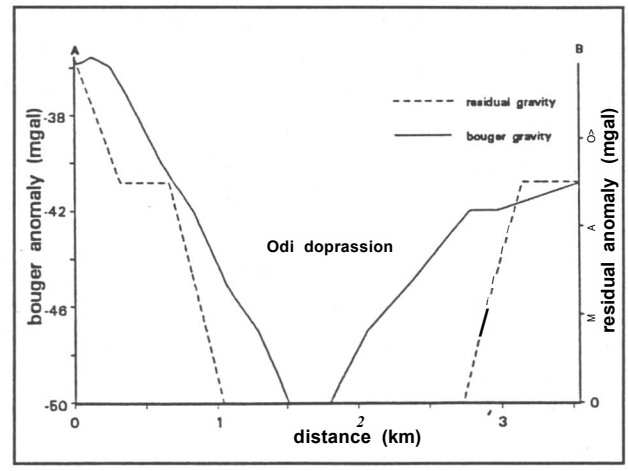

Figure 6.3. A cross section along the Odi depression using Bouguer and residual gravity data.

In general, the poor resolution of the obtained gravity data has limited further applications for structural studies, however, steep gravity gradients appear to correspond to major faults in the area. Although lineament patterns are known to reveal the difference between different blocks (Wellman, 1985), in the Derudeb area this seems to be poorly displayed because the lineaments were predominantly developed after the main regional deformation events that postdate accretion tectonics (Section 2.2.4).

Residual anomaly of the area appears to be comparably informative like the Bouguer gravity data. Local anomalies related to the geology are fairly enhanced by this data as expected, especially

in the 3-dimensional representation (Figure 6.2a). Good examples are the high anomalies around J. Tihilla and J. Bakabneb, and low gravity anomalies close to J. Arqawi and J. Malakat. Anomalies related to the Osir Walab Fault and the Kibirit Shear Zone, including the Odi depression, are also well depicted, though the poor resolution (1 : 1000 000) is thought to have still prevented the detection of more detailed local anomaly patterns expected to be revealed by this data. The interpretations made for the Bouguer gravity data are generally valid for the residual gravity anomaly. Interpretations of free air anomaly data for the RSH are given in Ott (1997).

An attempt has also been made to combine areas of high aeromagnetic and high gravity anomaly. Although most basic rocks are of high density and relatively rich in magnetite and other magnetically susceptible minerals, combination of these data yielded no systematic correlation with the surface geology. Similar result has been obtained for low magnetic and low gravity data, making this combination of little input to the geological knowledge of the area. This has been ascribed to the fact that both data types represent information obtained from different depths in the Earth's crust.

In most of the attempts made to combine gravity anomaly data with Landsat imagery, the conformity between the two data sets is seemingly good. Most intrusives that are both spectrally and morphologically distinct on the Landsat images are apparently revealed also on the gravity data. Linearly stretched gravity data also depicted the same result in showing few of the major lineaments. A good example where the gravity data strongly helped, and where Landsat imagery failed to give any strong hint as to the rock type, occurs around J. Bakabneb (Figure 6.1c and 6.2c). Here, it has also been difficult to undoubtedly mark the geologic boundary of this body only on bases of the imagery.

As it has been described in section 6.2 the Bouguer gravity data has not been topographically corrected. Preliminary observation revealed that some degree of topographic information is contained in gravity data. This initiated the idea of evaluating the possibility of removing the latter from the former using image processing methods. This was done by conversion of these data into raster formats and rescaling to an 8-bit range, followed by computation of PCA and ratio images. The PCA image yielded similar images as the inputs, showing the strong decorrelation between the data sets. The ratio image also provided no valuable information, making the method least useful.

Topographic data (Figure 6.2c) well express some geological features that help image interpretation. Most syn-orogenic plutons occupy a subdued topography unlike their post-orogenic equivalents which generally form prominent ridges in the area. Linear features such as the Adit-Langeb Lineament, Tashalal-Langeb Lineament, Adadi Thrust and Transpressional Shear Zone and NNE-SSW trending faults are well displayed. The uplifted Adar Ribad block is also explicit, likewise the Odi depression.

7 Summary and Conclusions

The geology of the Derudeb area has been studied primarily based on remote sensing techniques and GIS data analysis, aided by limited field data, with the production of a geological map at the scale of 1 : 250 000. The basement rocks of the Derudeb map sheet comprise part of the Nubian sector of the ANS that is generally of Neoproterozoic age. High grade gneisses (amphibolites, quartzofeldspathic gneiss, marble, and migmatite metamorphosed at mid-amphibolite facies), greenschist facies sequence of metasediments (graphite schist, marble, metasiltstone etc.) and metavolcanics of predominantly acidic composition, all intruded by mafic to acidic syn- and post-orogenic plutons constitute the basement lithology in the area. Sedimentary rocks of presumably Mesozoic age, basic to acidic Cenozoic volcanics and dikes comprise the Phanerozoic sequence.

At least three ductile deformation events (D_2-D_4), along with the accompanied magmatic events have been identified in the study area, the earliest D| phase being less explicit and by and large restricted to the gneissic rocks in the SE. The D_2/D_3 events were generated by NW-SE oriented principal compression that also produced the most penetrative structural features in the area, and accompanied by greenschist facies metamorphism and syn-orogenic magmatism. Major ductile transpressional shearing event (D_4) was post-dated by post-orogenic plutons and the associated contact metamorphism (M_4) at places. The brittle (D,) deformation is marked by prominent submeridional and NE-SW sets of brittle faults and lineaments.

Association of graphite gneiss, marble, intercalated quartzite and quartzofeldspathic gneiss in the high grade rocks in the SE, that range from deep-sea to shelf sediments, are thought to represent a passive continental margin, with the amphibolites symbolising intracontinental volcanism. The NE-SW trending ATTSZ, that demarcates the northern boundary of these rocks, exhibits a prominent sinistral displacement that was preceded by thrust tectonics similar to known sutures in the region (Stem *et al.,* 1990). Highly dismembered meta-ultramafics (pyroxenite, talc schist and minor serpentinite), marble and gabbroic rocks interpreted to show layered structure occur along this zone. Observation of Bouguer gravity and aeromagnetic data shows that the gneissic rocks are characterised by broad and monotonous anomaly pattern that trends parallel to this shear zone, unlike the highly resolved and differentiated pattern for the area to the N, also in good agreement with distribution of intrusive rocks. Based on these observations and regional considerations (eg. Drury and Berhe, 1993; Kroner *et al.,* 1991) it is suggested that the Adadi Thrust and Transpressional Shear Zone demarcates a possible crustal boundary to be considered in the accretion models for the RSH, Sudan. The redefined "Baraka Terrane" is bounded to the E-SE by the Baraka Suture, and is presumably older than the adjoining relatively juvenile terranes of Tokar (to the E) and Haya (to the N). It is, therefore, implied that the contact between the high grade gneisses and the greenschist facies rocks is tectonic, at least in the study area. The predominantly upper crustal rocks in the area may suggest moderate orogenic uplift and denudation, following the collision episode.

Sedimentary rocks of dominantly sandstone, mudstone, conglomerate and limestone make the oldest post-Pan-African stratigraphy in the Odi area. In the absence of substantial age evidence, it is suggested that these rocks were deposited in a N-S trending local rift basin of pre-Oligocene time, that possibly marked one of the earliest extension tectonics related to the Red Sea opening. The fact that this basin is bounded by deep-seated Pan-African faults (mainly the Adit-Langeb Lineament) of regional extent implies later reactivations of older structures. It is unclear if the sedimentation process was undisturbed until the Cenozoic.

These Pan-African faults were reactivated in the Late Oligocene *(ca.* 31 Ma ago), permitting the extrusion of basaltic flows through fissures in the Odi rift basin, and initiation of less extensive rift basin in the Adar Ribad area, as depicted by the submeridional abundant dikes. This event marked the second extensional event and is to be related to early rifting in the southern Red Sea suggested by Voggenreiter *et al.* (1988). Intraformational sedimentary layers that occur in the volcanic stratigraphy, added to some amygdaloidal basalts, suggest subaqueous volcanism. These observations imply that the earliest magmatic activity of *ca.* 31 ago was preceded by rather predominantly extensional structures and hardly any uplifting.

Extrusion of acidic flows in the central zone of Odi rift basin, close to the Tashalal-Langeb transform fault, and in the Adar Ribad area denote the latest extension tectonics of early Miocene *(ca. 22* Ma ago) in the Derudeb region that is apparently concomitant with the onset of major opening along the central Red Sea (Voggenreiter *et al.* (1988). Rough extension estimate less than 2 km anywhere in the basin is suggested. For the Adar Ribad area, however, the extension was certainly larger (with stratal dips of about 45°). These observations indicate that extension increases towards the margins of the Red Sea likewise the flank uplift. The volcanic activities in the Odi and Adar Ribad areas are not only coeval and related to similar magmatic rift settings, but make part of a large province that was represented by doming covering Ethiopia, Yemen, and Egypt (Menzies *et al.,* 1992; Almond, 1986). The Odi rift basin, therefore, represents an aborted rift that was active long before the Red Sea opening until early Miocene, since when the Red Sea possibly operates as the chief zone of extension. It denotes a long period of hiatus with no deposition at least since the Oligocene. Most of the younger submeridionally trending lineaments and draniage patterns in the area, however, are ascribed to the Neotectonic activity associated with the Red Sea opening.

The Odi subscene was used as a test site for digital image processing of Landsat TM and MSS data aimed at enhancing lithologic discrimination and structural features in the Derudeb area. PCA transformation, IHS-decorrelation stretching, band rationing, spatial filtering and image classification were conducted for this area. Remarkable lithologic enhancements by way of substantial spectral contrasts and morphologic features have been obtained through standardized PCA transformation, PC decorrelation stretching, directed band ratioing and IHS decorrelation stretching.

IHS decorrelation stretching of three least correlated bands (7, 4 and 1 in R, G and B, respectively) yielded the best image with overall good lithologic and structural information. Stretched input data generally gave further enhancement in the spectral contrast. PC transformations provided improved result with higher signal-to-noise ratio when standardized coefficients are used, instead of covariance matrix. Four bands, instead of six, proved sufficient in most cases to produce substantial spectral contrast, and modifications by convolving the first component with the other components yielded enhanced images. Decorrelation stretching is also a valuable tool in spectral enhancements by permitting more numbers of band triplets. Omission of PCs with much noise, or setting their coefficients to zero before retransformation, significantly improved the results. Band ratioing yielded geologically interpretable image by adopting the "directed band ratio" technique, that considers both spectral and morphologic information. It is to be emphasised, however, that combination of information obtained from different processing methods provided the best comprehensive result suitable for visual geologic image interpretation, and most enhancement techniques yield improved images when linearly stretched data are processed.

Supervised image classification of TM data yielded an inferior result for the area of interest, making digital image classification for lithologic discrimination less useful. While 3x3 mid-low filters have been found to provide improvements for some processed images, spatial enhancement through directional filters in NW, W and NE directions have been effective in mapping the lineaments in the area.

Gossan bodies associated with sulphide and gold mineralisations in the Ariab area have been successfully mapped using Feature Oriented PCA in which selected TM bands 1, 3, 4 and 7, and 1, 4, 5 and 7 were processed to enhance iron and hydroxyl rich minerals, respectively. Ratio image composite of 3/1, 5/4 and 5/7 in R, G and B, respectively, also yielded good result in enhancing the gossans. The use of a GIS overlay technique, based on image classification and data recoding followed by low pass filtering, has substantially improved the overall outcome by removing undesired objects. IHS-decorrelation stretching of bands 1, 4 and 7 in R, G and B, respectively, has led to the discovery of the Malakat gossan body of the Derudeb area, where band ratios failed to be effective.

Laboratory spectra have been helpful in studying the characteristics of desert varnish in the context of Landsat-TM data, and also compare to what extent the two data sets are comparable. Based on visual inspection of the reflectance curves obtained for different samples, limited chemical analyses and statistical methods it has been established that, in general, the extent of development of desert varnish, the lightness or darkness of the rock (which is in turn related to the mineral composition), including the Mn/Fe proportion of the exposed surface, and the wavelength under consideration control the effect of desert varnish on Landsat TM data.

Reflectance of rocks is remarkably reduced in the VIS part of the spectrum (up to 70%) due to desert varnish, consequently modifying absorption bands caused by iron-oxide to featureless spectra. Towards the longer wavelengths the reduction in intensity of reflectance is generally minimal (below 20%) and absorption features are well resolved but with reduced contrast. This effect is severe for light coloured (generally acidic) rocks than for dark coloured (commonly basic) rocks. The manganese-oxide coating the surface is responsible for these effects, and the desert varnish appears to have less influence in discriminating the gossan bodies, as alteration markers, from the non-gossan rocks. The latter has been ascribed to the occurrence of significant hydroxylated minerals in the gossans, which have strong signatures in the SWIR bands and that are less influenced by the desert varnish. The study also reveals that only part of the laboratory spectral variance is explained by Landsat TM data.

Aeromagnetic, topographic, Bouguer gravity and residual gravity anomaly data pertaining to the Derudeb area have been processed, merged, analysed and interpreted using a GIS technique in the context of geological study. In most cases a surface-representation has provided a visually more interpretable model. Bouguer and residual gravity data show substantial conformity with syn- and post-orogenic plutons in the area, with large-negative values corresponding to granitic intrusives and low-negative anomaly for gabbroids. Aeromagnetic data of the area is apparently less informative of the surface lithology.

The Odi depression is well shown on both Bouguer and residual gravity data supporting its rift structures, but linear features appear generally less resolved with exception to the Osir Walab Fault in the NE. More information on linear features are apparently revealed by aeromagnetic data, resolving most shear zones and major faults in the area, in addition to depicting possible extensive lineaments of regional dimensions not seen on the Landsat images. The study shows that increased magnetic gradients are closely related to deep-seated fault and fracture systems whose azimuth is often NE, with less vivid anomalies in the NW-SE direction.

Generally, the aeromagnetic anomaly distribution is fairly conformable with the gravity data. To the N and NW local and highly differentiated anomaly predominate, whereas in the S and SE broad anomalies with low amplitude prevail. These features are thought to be related to the broad geologic distribution whereby the former types of anomalies correspond to the juvenile Pan-African sequence of rocks and the latter are ascribed to the relatively older gneissic rocks of the Baraka Terrane. The aeromagnetic data, and to a lesser extent also the gravity anomaly, managed to depict the bounding Adadi Thrust and Transpressional Shear Zone between these crustal segments, corroborating the geologic data. More detailed studies are obviously required

to further substantiate this interpretation, and aeromagnetic and gravity data with much better resolution are expected to yield improved results by also increasing the extent to which the different data sets coroborate eachother.

8 References

ABDEL RAHMAN, E. M. (1993): Geochemical and geotectonic controls of the metallogenic evolution of selected ophiolite complexes from the Sudan. -*Berliner Geowiss. Abh.* (A), **145,** -175 pp., Berlin (FU-Berlin).

ABDELSALAMM-G. (1993): Structural evolution of the Oko shear zone, Sudan. *In* U. Thorweihe and H. Schandelmeier (eds.), -*Geoscientific Research in Northeast Africa,* 121-125, Rotterdam (Balkema).

ABDELSALAM, M. G. AND STERN, R. J. (1993): Tectonic evolution of the Nakasib suture, Red Sea Hills, Sudan: evidence for a late Precambrian Wilson cycle. -*J. Geol. Soc., London,* **150,** 393-404, London.

ABRAMS, **M. J.,** BROWN, **D.,** LEPLEY, **L.** AND SADWSKI, R. (1983): Remote sensing for porphyry copper deposits in Southern Arizona. -*Econ. Geol.,* **78,** 591-604, El Paso, Texas.

AHMED, F. (1977): Petrology and evolution of Tehilla igneous complex, Sudan. -*J. Geol.,* **85,** 331-343, Chicago.

ALMOND, D. C. (1986): Geological evolution of the Afro-Arabian dome. -*Tectonophysics,* **131,** 301-332, Amsterdam (Elsevier).

ALMOND, D. C., DARBYSHIRE, D. P. F. AND AHMED, F. (1989): Age limits for major shearing episodes in the Nubian Shield of NE Sudan. -*J. of African Earth Sei.,* **9,** (3/4), 489-496, UK (Pergamon).

BACKINGHAM, W. F. AND SOMMER, S. E. (1983): Mineralogical characterization of rock surfaces formed by hadrothermal alteration and weathering - application to remote sensing. -*Econ. Geol.,* **78,** 664-674, Littleton, CO.

BATES, R. L. AND JACKSON, J. A. (Eds.)(1987): *Glossary of Geology.* 3rd ed., -788 pp., Alexandria, Virginia (Am. Geol. Inst.).

BERHE, S. M. (1990): Ophiolites in northeast and east Africa: implications for Proterozoic crustal growth. -*J. Geol. Soc. London,* **147,** 41-57, London.

CAMP, V. E. (1984): Island arcs and their role in the evolution of the western Arabian Shield. -*Geol. Soc. Am. Bull.,* **95,** 913-921, Boulder.

CHAVEZ, P. S., BERLIN, G. L., AND SOWERS, L. B. (1982): Statistical method for selecting Landsat MSS ratios. -*J. Applied Photograph. Eng.,* **8,** 23-30, Washington, DC.

CRANE, R. B. (1971): Processing techniques to reduce atmospheric and sensor variability in multispectral scanner data. -*Proceed. 7th Int. Symp. Remote Sens. Environ.,* **2,** 1345-1355, Ann Arbor, MI.

CRIPPEN, E. (1989): Selection of Landsat TM band and band-ratio combinations to maximize lithologic information in colour composite displays. -*Proceed. 7th Them. Conf. Remote Sens. Expl. Geol.,* Calgary, Alberta, 2, 917-921, Ann Arbor, ML

CRIPPEN, E., BLOM, R. G., AND HEYADA, J. R. (1988): Directed band ratio ing for the retention of perceptually-independent topographic expression in chromatically-enhanced imagery. -*Int. J. Remote Sens.,* **9** (4), 749-765, London (Taylor and Francis).

CROSTA, A. P. AND McM. MOORE, J. (1989): Enhancement of Landsat Thematic Mapper imagery for residual soil mapping in SW Minas Gerais State, Brazil: A prospecting case history in Greenstone belt terrane. -*Proceed. 7th Thematic Conf. Remote Sens. Expl. Geol.,* Calgary, Alberta, 2, 1173-1187, Ann Arbor, ML

DAVIS, J. C. (1986): *Statistics and data analysis in geology.* 2nd ed., -620 pp., New York, NY (Wiley).

DAVIS, P. A., BERLIN, G. L. AND CHAVEZ, P. S. (1987): Discrimination of altered basaltic rocks in the southwestern United States by analysis of Landsat Thematic Mapper data. -*Photogramm. Eng. Remote Sens.,* **53** (1), 45-55, Bathesda, Maryland.

DELANY, F. M. (1956): *Geological map ofDerudeb, sheet 46-1, scale 1 : 250 000.* -Geological Survey, Sudan, Khartoum.

Drury, S. A. (1993): *Image interpretation in geology.* -2nd ed., -283 pp., London (Chapman and Hall).

DRURY, S. A. AND BERHE, S. M. (1993): Accretion tectonics in northern Eritrea revealed by remotely sensed imagery. -*Geol. Mag.,* **130** (2), 177-190, Cambridge.

EL LABIB, A. A. M. (1991): *Structure and petrology of the basement and post-orogenic ring complexes, Derudeb area, NE Sudan.* -185 pp., unpubl. MPhil. thesis, Portsmouth polytechnic, UK.

EMBLETON, J. C. B., HUGHES, D. J., KLEMENIC, P. M., POOLE, S. AND VAIL, J. R. (1983): A new approach to the stratigraphy and tectonic evolution of the Red Sea Hills, Sudan. -*Bull. Fac. Earth Sei., King Abdulaziz Univ. Jeddah, 6,* 101-112, Oxford.

ERDAS (ed.) (1982-1994): *Erdas Field Guide.* - Atlanta (ERDAS, Inc.).

GASS, I. G. (1981): Pan- African (Upper Proterozoic) plate tectonics of the Arabian-Nubian Shield. *In* A. Kroner (ed.), -*Precambrian Plate Tectonics,* 387-405, Amsterdam (Elsevier).

GABERT, G., RUXTON, B. P., AND VENZLAFF, H. (I960): Uber Untersuchungen im Kristallin der nördlichen Red Sea Hills im Sudan. -*Geol. Jb.,* **77,** 241-270, Hannover.

GILLESPIE, A. R., KAHLE, A. B. AND WALKER, R. E. (1986): Colour enhancement of highly correlated images, I. decorrelation and HSI contrast stretches. -*Remote Sens. Env.,* **20,** 209-235, New York, NY (Elsevier).

GILLESPIE, A. R., KAHLE, A. B. AND WALKER, R. E. (1987): Colour enhancement of highly correlated images. II. Channel ratio and "chromaticity" transformation techniques. -*Remote Sens. Env.,* **22,** 343-365, New York, NY (Elsevier).

GRAS (1988): *Geological map of the Sudan,* Sheet 6 - Port Sudan, 1 : 1 000 000.

GRIFFITHS, D. H. AND KING, R. F. (1981): *Applied geophysics for geologists and engineers; the elements of geophysical prospecting.* -230 pp., England (Pergamon).

GUPTA, R. P. (1991): *Remote sensing geology.* -356 pp., Berlin-Heidelberg (Springer).

HAENISCH, H. (1997): Radiometrische Korrectur von Landsat-TM-Daten unter Einbeziehung eines digitalen Geländemodells; am Beispiel der Geologischen Karte Blatt Sinkat 1:250 000, NE Sudan. - PhD thesis, FB Geowissenschaften, Freie Universität Berlin (in prep.).

HAENISCH, H., KENEA, N. H., AND OTT, N. (1996): Tectonic development of the southern Red Sea Hills of Sudan-evidence from Landsat TM-mosaic interpretation. -*Int. Arch. Photogramm. Remote Sens.,* **31** (B7), 262-267, Vienna.

HARALICK, R. M. (1978): Statistical and structural approach to texture. -*Proc. Int. Symp. Remote Sensing for Observation and Inventory of Earth Resources and the Endangered Environment,* 379-431.

HASSAN, A. S. (1991): *Cainozoic volcanic rocks and intraformational sediments from the Red Sea Hills, Sudan.* -209 pp., unpubl. Mphil. thesis, Portsmouth Polytechnic, UK.

HUNT, G. R. AND SALISBURY, J. W. (1970): Visible and near- infrared spectra of minerals and rocks: I. Silicate minerals. - *Modern Geol.,* **1,** 283-300, New York, NY.

HUNT, G. R. AND SALISBURY, J. W. (1971): Visible and near-infrared spectra of minerals and rocks: II. Carbonates. -*Modern Geol.,* **2,** 23-30, New York, NY.

HUNT, G. R., SALISBURY, J. W. AND LENHOFF, C. J. (1971): Visible and near-infrared spectra of minerals and rocks: III. Oxides and hydroxides. -*Modern Geol.,* **2,** 195-205, New York, NY.

HUNT, G. R., SALISBURY, J. W. AND LENHOFF, C. J. (1974): Visible and near-infrared spectra of minerals and rocks: IX. Basic and ultrabasic igneous rocks. -*Modern Geol.,* **5,** 15-22, New York, NY.

KAUFMANN, H. (1988): Mineral exploration along the Aqaba-Levant structure by use of TM-data: Concepts, processing and results. -*Int. J. Remote Sens.,* **9** (10 and 11), 1639-1658, London (Taylor and Francis).

KENEA, N. H. (1997): Improved geologic mapping using Landsat TM data, Southern Red Sea Hills, Sudan: PC and IHS decorrelation stretching. -*Int. J. Remote Sens.,* **18,** 1233-1244, London (Taylor and Francis).

KENEA, N. H. AND HAENISCH, H. (1996): Principal component analyses for lithologic and alteration mappings: examples from the Red Sea Hills, Sudan. -*Int. Arch. Photogramm. Remote Sens.,* **31** (B7), 271-275, Vienna.

KLEMENIC, P. M. AND POOLE, S. (1988): The geology and geochemistry of Upper Proterozoic granitoids from the Red Sea Hills, Sudan. -*J. Geol. Soc., London,* **145,** 635-643, London.

KOWALIK, W. S. AND GLENN, W. E. (1987): Image processing of aeromagnetic data and integration with Landsat images for improved structural interpretation. -*Geophysics,* **52** (7), 875-884, Tulsa, OK.

KRONER, A., GREILING, R., REISCHMANN, T., HUSSEIN, I. M., STERN, R. J., DÜRR, S., KRÜGER, J., AND ZIMMER, M. (1987): Pan- African crustal evolution in the Nubian segment of Northeast Africa. *In* A. Kroner (ed.): Proterozoic lithospheric evolution. -*Am. Geophys. Union,* Geodyn. Ser., **17,** 235-257, Washington, DC.

KRONER, A., LINNEBACHER, P., STERN, R. J., REISCHMANN. T., WANTON, W., AND HUSSEIN, I. M. (1991): Evolution of Pan- African island arc assemblages in the southern Red Sea Hills, Sudan, and in southwestern Arabia as exemplified by geochemistry and geochronology. *In* R. J. Stem and W. R. Schmus (eds.), Proterozoic Crustal Evolution in the Late Proterozoic. -*Precambrian Research,* 53, 99-118, Amsterdam.

KRUSE, F. A. (1996): Identification and mapping of minerals in drill core using hyperspectral image analysis of infrared reflectance spectra. -*Int. J. Remote Sens.,* **17** (9), 1623-1632, London (Taylor and Francis).

KÜSTER, D. (1993): Geochemistry and petrogenesis of Permo-Jurassic oversaturated alkaline complexes of northern Kordofan, central Sudan. *In* U. Thorweihe and H. Schandelmeier (eds.), -*Geoscientific Research in Northeast Africa,* 197-201, Rotterdam (Balkema).

LILLESAND, T. M. AND KIEFER, R. W. (1994): *Remote sensing and image interpretation.* 3rd ed., -750 pp,, New York, NY (Wiley).

LAURINI, R. AND THOMPSON, D. (1992): *Fundamentals of spatial information systems.* -680 pp, London (Academic Press).

LIST, F. K. (1992): Basic physics of remote sensing. *In* P. Bankwitz and F. K. List (eds.), - Proceed, of the 3rd United Nations Int. Training Course on Remote Sens. Appl. to Geol. Sei., Potsdam and Berlin. -*Berliner Geowiss. Abh.,* D, 5, 27-35, Berlin.

LIST, F. K. (1993): Fundamentals of digital image processing for geologic applications. *In* F. K. List and P. Bankwitz (eds.), - Proceed, of the 4th United Nations Int. Training Course on Remote Sens. Appl. to Geol. Sei., Potsdam and Berlin. -*Berliner Geowiss. Abh.,* D, 5, 7-29, Berlin.

LIST, F. K., KOCH, W., AND SALAHCHOURIAN, M. H. (1992): Geological mapping in arid regions of Africa using satellite data -integration of visual and digital techniques. -*Int. Arch. Photogramm. Remote Sens.,* **29** (B4), 325-332, Washington, DC.

Liu JIANGuo AND McM. MOORE, J. (1989): Colour enhancement and shadow suppression techniques for TM images. -*Proceed. 7th Them. Conf. Remote Sens. Expl. Geol.,* Calgary, Alberta, 2, 901-915, Ann Arbor, ML

LIU JIAN Guo AND McM. MOORE, J. (1990): Hue image RGB colour composition. A simple technique to suppress shadow and enhance spectral signature. -*Int. J. Remote Sens.,* **11** (8), 1521-1530, London (Taylor and Francis).

Liu JIANGuo AND McM. MOORE, J. (1993): Cloud-shadow suppression technique for enhancement of Air Borne Thematic Mapper imagery. -*Photogramm. Eng. Remote Sens.,* 59 (8), 1287-1291, Bathesda, Maryland.

LOHMANN, G. (1994): *EBIS-Evidenz-basierte Interpretation von Satellitendate.* -Geosystems User Group Meeting, 20-21 June, Feldafing, 6-10.

LOUGHLIN, W. P. (1989): Principal component analysis for alteration mapping. -*Photogramm. Eng. Remote Sens.,* 57 (9), 1163-1169, Bathesda, Maryland.

LYON, R. J. P. (1990): Effects of weathering, desert-varnish, etc. on spectral signatures of mafic, ultramafic and felsic rocks, Leonora, West Australia. -*IEE Geoscience and Remote Sensing,* **10,** 1719-1722, New York, NY.

MAKRIS, J. AND RiHM, R. (1991): Shear-controlled evolution of the Red Sea: pull apart model. -*Tectonophysics,* **198,** 441-166, Amsterdam.

MENZIES, M. A., BAKER, J., BOSENCE, D., DART, C., DAVIDSON, I., HURFORD, A., AL'KADASI, M., MCCLAY, K., NICHOLS, G., AL'SUBBARY, A. AND YELLAND, A. (1992): The timing of magmatism, uplift and crustal extension: preliminary observation from Yemen. *In* B. C. Story, T. Alabaster and R. J. Panchurst (eds.), -*Geological Soc. Spec. Publ.,* 68, 293-304, Broughton Gillford, Melksham (Cromwell).

OTT, N. (1997): GIS-Modellierung und Klassifizierung von geophysikalischen, geologischen und Fernerkundungs-Daten aus den südlichen Red Sea Hills (Sudan). -PhD thesis, FB Geowissenschaften, Freie Universität Berlin (in prep.).

PALACIOS-ORUETA, A. AND USTIN, S. L. (1996): Multispectral statistical classification of soil spectra. -*Remote Sens. Env.,* **57,** 108-118, New York , NY (Elsevier).

RAMSAY, J. G. (1967): *Folding and fracturing of rocks.* -568 pp., New York (McGraw-Hill).

READY, P. J. AND WlNTZ, P. A. (1973): Information extraction, SNR improvement, and data compression in multispectral imagery. -*IEEE Trans. Communic.,* **21** (10), 1123-1130, New York, NY.

REX, D. C. (1994): K-Ar age determinations of samples from LEG 134. *In* Green, H. G., Collot, J. -Y., Stokking, L. B., *et al.,* -*Proceed, of the ODP, Sei. Results,* **134,** 413-414, College Station, TX (Ocean Drilling Program).

ROCKWELL, B. W. (1989): Hydrothermal alteration mapping in spectral ratio feature space using TM reflectance data: Aurora Mining District, Mineral County, Nevada. -*Proceed. 7th Them. Conf. Remote Sens. Expl. Geol.,* Calgary, Alberta, 2, 1189-1203, Ann Arbor, MI.

ROTHERY, D. A. AND HUNT, G. A. (1990): A simple way to perform decorrelation stretching and related techniques on menu-driven image processing systems. -*Int. J. Remote Sens.,* **11** (1), 133-137, London (Taylor and Francis).

SABINS, F. F. Jr. (1987): *Remote Sensing Principles and Interpretation.* 2nd ed., -449 pp., Sanfrancisco (Freeman).

SCHANDELMEIER, H., KÜSTER, D., WlPFLER, E., ABDEL RAHMAN, E. M., STERN, R. J., ABDELSALAM, M. G. AND SULTAN, M. (1993): Evidence for a new Late Proterozoic suture in Northern Sudan. *In* U. Thorweihe and H. Schandelmeier (eds.), -*Geoscientific Research in Northeast Africa,* 83-85, Rotterdam (Balkema).

SCHANDELMEIER, H. AND PUDLO, D. (1990): The central African fault zone (CAFZ) in Sudan-A possible continental transform fault. -*Berl. Geowiss. Abh.,* A, **120.1,** 31-44, Berlin (FU-Berlin).

SEGAL, D. B. (1983): Use of Landsat Multispectral Scanner data for definition of limonitic exposures in heavily vegetated areas. -*Econ. Geol.,* **78,** 711-722, El Paso, Texas.

SEMTNER, A. K. (1993): Uplift kinematics of Jebel Dirurba sedimentary complex, Red Sea Hills, Sudan. *In* U. Thorweihe and H. Schandelmeier (eds.), -*Geoscientific Research in Northeast Africa,* 197-201, Rotterdam (Balkema).

SHACKLETON, R. M. (1994): Review of Late Proterozoic sutures, ophiolitic melanges and tectonics of eastern Egypt and north-east Sudan. -*Geol. Rdsch.,* **83,** 537-546, Stuttgart.

SHEFFIELD, C. (1985): Selecting band combinations from multispectral data. -*Photogramm. Eng. Remote Sens.,* **51** (6), 681-687, Bathesda, Maryland.

SINGH, A. AND HARRISON, A. (1985): Standardized principal components. -*Int. J. Remote Sens.,* **6** (6), 883-896, London (Taylor and Francis).

SPATZ, D. M., TARANIK, J. V. and Hsu, L. C. (1987): Desert varnish on volcanic rocks of the Basin and Range Province - composition, morphology, distribution, origin and influence on Landsat imagery. -*Proceed. 21st Int. Symp. Remote Sens. Env.,* **2,** 843-852, Ann Arbor, ML

STERN, R. J., NIELSEN, K. C., BEST, E., SULTAN, M., ÄRVIDSON, R. E. AND KRONER, A. (1990): Orientation of late Precambrian sutures in the Arabian-Nubian shield. -*Geology,* **18,** 1103-1106, Boulder.

STERN, R. J., KRONER, A. AND RASHWAN, A. A. (1991): A late Precambrian (-710 Ma) high volcanicity rift in the southern Eastern Desert of Egypt. -*Geol. Rdsch.,* **80** (1), 155-170, Stuttgart.

SULTAN, M., CHAMBERLAIN, K. R., BOWRING, S. A., ARVIDSON, R. E., ABUZIED, H., AND EL KALIOUBY, B. (1990): Geochronologie and isotopic evidence for involvement of pre-Pan-African crust in the Nubian Shield, Egypt. - *Geology,* **18,** 761-764, Boulder.

TECHNOEXPORT (1974): Final report, -unpubl. report, Geological Research Authority of Sudan, v. **8.**

TELFORD, W. M., GELDART, L. P., SHERIFF, R. E. AND KEYS, D. A. (1976): Applied geophysics. - 860 pp., Cambridge (Cambridge University).

VAIL, J. R. (1976): Location and geochronology of igneous ring-complexes and related rocks in north-east Africa. -*Geol. Jb.,* **B 20** (7), 97-1 14, Hannover.

VAIL, J. R. (1985): Pan-African (late Precambrian) tectonic terrains and the reconstruction of the Arabian-Nubian Shield. -*Geology,* **13,** 839-842, Boulder.

VAIL, J. R. (1988): *Lexicon of geological terms for the Sudan.* -199 pp., Rotterdam (Balkema).

VAIL, J. R. (1993): The dike swarms of north-eastern Sudan. *In* U. Thorweihe and H. Schandelmeier (eds.), -*Geoscientific Research in Northeast Africa,* 127-131, Rotterdam (Balkema).

VOGGENREITER, W., HÖTZL, H. AND JADO, A. R. (1988): Red Sea related history of extension and magmatism in the Jizan area (Southwest Saudi Arabia): indication for simple-shear during early Red Sea rifting. -*Geol. Rdsch,* **77** (1), 257-274, Stuttgart.

WELLMAN, P. (1985): Block structure of continental crust derived from gravity and magnetic maps, with Australian examples. *In* W. J. Hinze (ed.), -*The utility of Regional Gravity and Magnetic Anomaly Maps,* 102-108, Tulsa, Oklahoma (Soc. Expl. Geophy.).

WILLIAMS, R. S. Jr. (1983): Geological applications. In: *Manual of Remote Sensing,* 2nd ed., 2, 1667-1951, R. N. Colwell (ed.), Am. Soc. of Photogramm., Falls Church, VA.

WlPFLER, E. L. (1994): Geochemische, strukturelle und erzmikroskopische Untersuchungen zur Lagerstättenentwicklung des westlichen Ariab Nakasib Belt, Red Sea Provinz, NE-Sudan. - *Berliner Geowiss. Abh.,* A, 166, -206 pp., Berlin (FU-Berlin).

9 Appendices

Appendix - 1

Some characteristics of Landsat-5 data used for image processing.

Data characteristics	TM-data	MSS-data
Scene ID	5058 4 07 253	50584 07253 1
Path	171	171
Row	48	48
Date of acquisition	06.10.1985	06.10.1985
Local time	7:25:30	7:25:30
Sun elevation	53°	53°
Sun azimuth	125°	125°
Coordinates of nadir point	17:35 N, 36:50 E	17:21 N, 36:30 E

Appendix - 2

Laboratory reflectance values within the TM spectral ranges obtained for samples with cut surfaces.

SAMPLE #	TM-1	TM-2	TM-3	TM-4	TM-5	TM-7
1	15.30	16.89	21.92	23	63.93	51.81
142	35.43	37.56	42.98	47.18	75.75	60.86
144	45.42	48	50.75	54.26	64.08	52.21
149	69.38	74.5	76.18	70.46	74.62	53.87
188	24.31	26.97	29.04	29.21	32.03	29.5
183	19.12	19.54	18.86	17.55	13.45	12.27
167	30.03	29.51	27.32	23.83	16.57	13.25
176	61.60	63.8	63.89	61.1	53.96	36.75
208	41.67	40.34	38.71	35.46	25.44	20.91
206	25.01	25.94	23.46	22.23	29.41	31.75
168	29.92	29.35	27.84	25.18	19.35	14.41
179	47.72	50.32	53.67	55.82	44.76	43.47
107	29.15	29.3	29.16	28.94	26.01	25.09
105	28.88	29.36	27.5	24.92	22.16	18.81
181	29.34	31.22	30.48	28.1	29.16	22.02

Appendix - 3

Laboratory reflectance values within the TM spectral ranges obtained for samples with exposed surfaces.

SAMPLE #	TM-1	TM-2	TM-3	TM-4	TM-5	TM-7
1	9.30	11.41	15.02	18.33	40.58	32.63
142	9.59	11.10	12.80	12.93	40.30	32.09
144	12.13	13.72	15.92	19.13	35.33	38.37
149	24.09	25.76	26.44	25.30	29.74	29.41
188	7.63	8.18	8.80	10.27	17.43	20.18
183	9.99	12.73	15.00	17.07	22.02	18.66
167	11.25	12.86	14.51	15.74	18.34	16.07
176	26.18	31.66	35.47	37.29	39.66	28.04
208	16.83	18.33	19.09	18.85	16.14	14.14
206	9.75	10.71	11.12	11.42	19.27	23.51
168	9.36	10.75	12.02	13.76	22.13	21.54
179	11.58	12.10	12.75	14.41	24.48	29.17
107	8.01	9.67	11.68	13.91	29.67	30.00
105	15.43	20.48	24.02	25.86	29.20	26.34
181	25.17	28.48	29.32	29.74	38.32	31.93

Appendix -4

Grey values obtained from TM data for sample points corresponding to those in appendices 2 and 3.

SAMPLE #	TM-1	TM-2	TM-3	TM-4	TM-5	TM-7
1	73	55	97	90	167	114
142	43	30	51	48	121	79
144	53	37	61	53	115	75
149	45	31	53	63	153	101
188	62	46	79	67	132	80
183	44	32	53	84	153	94
167	37	26	42	39	85	54
176	53	39	68	59	129	81
208	68	49	86	77	156	105
206	67	51	87	76	143	95
168	42	28	46	44	100	59
179	63	44	74	64	104	62
107	53	37	62	55	111	70
105	64	44	75	64	118	75
181	44	35	56	50	103	68

GEOLOGICAL MAP

Enclosure

Sheet Derudeb (NE 37 - 1)

GEOLOGIC UNITS

QUATERNARY
- Wd — Wadi deposits
- Qu/w — Undiff. Quaternary deposits/ partly consolidated
- Qg — Old gravel (affected by desert varnish)
- Qgv — Quartz gravel (affected by desert varnish)

MESOZOIC(?) CENOZOIC

Younger Cover Rocks
- Cqp — Quartz-porphyry
- Cdc — Dacite
- Crh — Rhyolite
- Cbsw — Basalt/strongly weathered
- Msd — Undiff. sedimentary rocks
- Mss — Sandstone

Post-Orogenic Granitoids
- Pgsg — Granite
- Pgbw — Gabbroid/strongly weathered

Syn- to Late-Orogenic Granitoids
- Pgsg/w — Metagranite/ strongly weathered
- Pgbw — Metagabbro/partly weathered
- Pdg/w — Metadiorite-granodiorite/ strongly weathered
- Pum — Meta-ultramafics
- Pdg — Syn-orogenic granite

LATE PROTEROZOIC (PAN-AFRI A^2

Metavolcano-sedimenatary Rocks (Nafrideib Series/Greenschist Ass.)
- Pmsd — Metasedimentary rocks
- Pmc — Marble
- Pamv — Acidic metavolcanics
- Pvsg — Undiff. metavolcano-sediments (greenschist f.)/weathered
- Pvsa — Undiff. metavolcano-sediments (amphibolite f.)
- Pgsc — Graphite schist

PRE(?)-PAN-AFRICAN

High-grade Rocks/Kashabib Series
- Pgsm — Graphite gneiss (migmatitic)
- Paq — Intercalated quartzite and amphibolite
- Pugn — Undiff. gneisses

GEOLOGIC SYMBOLS

- Geologic boundary
- Major fault, inferred
- Minor fault, inferred
- Normal fault
- Lateral fault
- Thrust fault
- Axial trace of synform
- Axial trace of antiform
- Dike (Cenozoic)
- Dike (Pan-African)
- 70 — Strike & dip of foliation
- 55 — Strike & dip of strata
- 45 — Plunge of lineation
- Gossan/sulphide occurrence
- Manganese occurrence
- 26 Ma — K-Ar whole rock age

OTHER SYMBOLS

- Main road
- Railway
- Township/settlement
- International boundary

INDEX (TM-171/48)

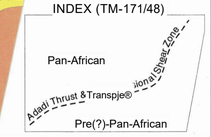

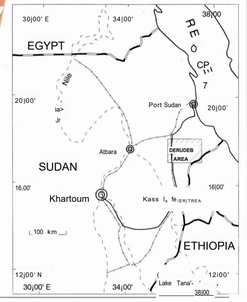

Free University of Berlin,
Institute of Geology, Geophysics and Geoinformatics,
Remote Sensing Working group; Prof. Dr. F. K. List
Maltaserstrasse 74 - 100, D-12249 Berlin, Germany

Printed by TFH Berlin, 1997

Digital image processing, geological interpretation and field work, GIS data processing and integration, geochronological data, and cartographic concept:
NASIR HASEN KENEA, 1997

Scale 1 : 250 000

10 0 10 km

D-LandsatTM & MSS; 171-48, 06.10.1985
-Aerial photographs; GRAS, 1 : 40 000
-Large Format Camera; frame 1321, 1 : 75 000
-Topographic maps; Sudan Survey Department, 1 : 100 00
-Aeromagnetic/gravity data; GRAS, 1 : 200 000/500 000

Grid: U.T.M zone 37
Projection: Transverse Marcator
Spheroid: Clarke 1880
Units: Meter
Meridian of origin: 39j E
Datum: Adindan

BERLINER GEOWISSENSCHAFTLICHE ABHANDLUNGEN
Freie Universität Berlin • Technische Universität Berlin • Technische Fachhochschule Berlin

Noch erhältlich sind:

Reihe D: Geoinformatik

Band 1 / **Peter Bankwitz & Franz K. List (Hrsg.):** Proceedings of the Third United Nations International Training Course on Remote Sensing Applications to Geological Sciences, held at Potsdam and Berlin. October 7 to 25, 1991. 160 S., 101 Abb., 3 Tab., 1992. DM 30,-.

Band 2 /Michael Fietz: Art- und schadensbedingtes Abbildungsverhalten von Berliner Straßenbäumen auf Colorinfrarot-Luftbildern. 215 S., 67 Abb., 21 Tab., lOTaf., 1992. DM 49,-.

Band 3 /Christiane C. Schmullius: Radarfernerkundung landwirtschaftlicher Flächen mit einem flugzeuggetragenen L-, C- und X-Band Scatterometer. 111 S., 77 Abb., 7 Tab., 1992. DM 42,-.

Band 4/Junfeng Luo: Konditionale Markovsimulation 2-dimensionaler geologischer Probleme. 103 S., 55 Abb., 38 Tab., 1993. DM 48,-.

Band 5 /Franz K. List & Peter Bankwitz (Hrsg.): Proceedings of the Fourth United Nations/CDG International Training Course on Remote Sensing Applications to Geological Sciences, held at Potsdam and Berlin, September 28 to October 16, 1992. 120 S,, 88 Abb., 4 Tab., 1993. DM 38,-.

Band 6 /Christian Bauer: Digitale Bildverarbeitung von großräumigen Satellitenbild-Verbänden: Mosaikbildung, multitemporale Analyse und Klassifizierung. 97 S., 35 Tab., 58 Abb., 1994. DM 48,-.

Band 7 /Gerold Reusing: Contribution to the Risk Analysis of Hydrologic Droughts Based on Hydrologic Time Series of the River Nile. 125 S., 74 Abb., 24 Tab/, 1994. DM 54,-.

Band 8 /Sabine Balmer-Heynisch: Erfahrungen bei der Erstellung von rechnergestützten Bewertungssystemen für die Ermittlung des Grundwassergefährdungspotentials kontaminierter Altstandorte im Hinblick auf Sanierungsmaßnahmen. 208 S., 1995. DM 74,-.

Band 9 /Jörg Tietze: Geostatistisches Verfahren zur optimalen Erkundung und modellhaften Beschreibung des Untergrundes von Deponien. 96 S., 1995. DM 51,-.

Band 10 /Andreas Neutze: Ein Beitrag zur geostatistischen Raum-Zeit-Prognose. Anwendungsbeispiel bodennahes Ozon. 119 S., 1995. DM 59,-.

Band 11 / Claudia Werner: Digitale Klassifizierung und GIS-Analyse von MOMS-02/D2-Bilddaten eines tropischen Regenwaldgebiets in Mindanao (Philippinen). 115 S., 1996. DM 57,-.

Band 12 / Wolfgang Koch: Analyse und Visualisierung geowissenschaftlicher Daten mit Hilfe digitaler Bildverarbeitung und eines Geo-Informationssystems. Beitrag zur regionalen Geologie der Red Sea Hills, Sudan. 103 S., 44 Abb., 14 Tab., 2 Karten. 1996. DM 68,-.

Band 13 /Michael Wolfgang Köhnke: Beitrag zur Dürrerisiko-Abschätzung in der Nördlichen Gezira-Ebene (Sudan). 99 S. 1997. DM 51,-.

Band 14 **/Nasir Hasen Kenea:** Digital Enhancement of Landsat Data, Spectral Analysis and GIS Data Integration for Geological Studies of the Derudeb Area, Southern Red Sea Hills, NE Sudan, 116 S., 1997. DM 79,-.

Das vollständige Verzeichnis der lieferbaren Titel der Reihen A, B, C, D und E ist erhältlich bei:

Selbstverlag Fachbereich Geowissenschaften, FU Berlin
Fax: (0)30 -776 20 34
Tel.: (0) 30-7762360
Malteserstraße 74-100
Bibliothek, Haus C
D-12249 Berlin